

LUNAR SURFACE PROCESSES

Friedrich Hörz, Richard Grieve, Grant Heiken, Paul Spudis, and Alan Binder

The Moon's surface is not affected by atmosphere, water, or life, the three major agents for altering terrestrial surfaces. In addition, the lunar surface has not been shaped by recent geological activity, because the lunar crust and mantle have been relatively cold and rigid throughout most of geological time. Convective internal mass transport, which dominates the dynamic Earth, is therefore largely absent on the Moon, and so are the geological effects of such internal motions—volcanism, uplift, faulting, and subduction—that both create and destroy surfaces on Earth. The great contrast between the ancient, stable Moon and the active, dynamic Earth is most clearly shown by the ages of their surfaces. Nearly 80% of the entire solid surface of Earth is <200 m.y. old. In contrast, >99% of the lunar surface formed more than 3 b.y. ago and >70% of the lunar surface is more than ~4 b.y. old.

Despite the fact that lunar surface processes are less varied and dynamic than those of the Earth, complex alterations of the lunar surface do occur; the most important source of such alterations, at least during the last 3 b.y., is external to the Moon. The Moon's stable but heavily cratered surface provides evidence that planets are continuously bombarded by external objects ranging from small dust specks to giant bodies tens of kilometers in diameter.

The Moon and all other planets are not isolated, closed systems. They are an integral part of a dynamic solar system that continues to evolve under largely gravitational forces. Orbits of predominantly small bodies are continually rearranged by close

encounters with each other and with larger planets throughout the lifetime of the solar system. These orbital alterations are generally minor, but they ensure that, over geological periods, collisions with other bodies will occur.

When such a collision happens, two outcomes are possible. If "target" and "projectile" are of comparable size, collisional fragmentation and annihilation occurs, producing a large number of much smaller fragments. If the target object is very large compared to the projectile, it behaves as an "infinite halfspace," and the result is an impact crater in the target body. For collisions in the asteroid belt, many of the resulting collisional fragments or crater ejecta escape the gravitational field of the impacted object; many of these fragments are then further perturbed into Earth-crossing orbits to form the majority of the projectiles that impact the Earth and Moon.

The Moon's population of impact craters represents a faithful record of these collisional processes over most of the lifetime of the solar system. By comparison, only the barest outlines of the cratering history of Earth can be reconstructed, even for just the last 200 m.y., and only a few structures older than 500 m.y. have been identified.

Typical impact velocities of asteroidal objects on the Moon at present are between 15 and 25 km/sec; they were apparently somewhat lower prior to 4 b.y. ago. Such high velocities, combined with a high frequency of impact events (especially before 3.8 b.y. ago), have expended a cumulative kinetic energy on the lunar surface that exceeds the lunar internal energy released by volcanism and seismicity. As a

result, meteorite impact has been, and continues to be, the dominant lunar surface process, although volcanic and tectonic processes were also important in the Moon's distant past.

In this chapter, lunar surface processes are grouped by decreasing importance into impact-related phenomena (section 4.1), volcanic processes (section 4.2), and tectonic activity (section 4.3). A summary of lunar geologic history and associated stratigraphy is presented in section 4.4.

4.1. IMPACT PROCESSES

The projectiles that now enter the Earth/Moon system are derived from the asteroid belt and from comets. The most massive objects are entire asteroids or comets, which are generally a few kilometers in diameter, but rarely a few tens of kilometers across. Most projectiles, however, are smaller fragments from asteroidal collisions that vary widely in size; small specimens reach the Earth's surface as meteorites a few grams to a few metric tons in weight. The exceedingly fine-grained "micrometeoroids" (fragments <1 mm in diameter, with masses $\lesssim 10^{-2}$ g; see section 3.10) may be either the most fine-grained collisional debris from asteroids or small particles released from comets (e.g., Gehrels, 1979; Shoemaker, 1983).

Projectile masses impacting the lunar surface have ranged over 35 orders of magnitude, from microscopic dust particles weighing 10^{-15} g to huge asteroids of 10^{20} g; associated kinetic energies vary from a small fraction of an erg to $\sim 10^{32}$ ergs per individual impact. By comparison, the total internal energy released by the Earth, which drives such visible processes as volcanism and tectonism, is estimated at 10^{26} to 10^{27} ergs per year (Lammlein *et al.*, 1974). The "geologic" manifestations of impacts on the Moon range from microscopic craters <0.1 μm in diameter on tiny grains of lunar soil to impact basins hundreds of kilometers across on the lunar surface. Lunar global surface evolution has thus been dominated by a small number of discrete but rare, large-body, basin-forming impacts as well as by the more continuous pounding from numerous smaller and less energetic projectiles. The latter group produces smaller craters, together with some unique cumulative surface effects.

Characterization of many lunar surface processes therefore requires an understanding of the consequences of single hypervelocity (>3 km/sec) impacts of vastly different scales. Section 4.1.1 provides a phenomenologic and geometric description of fresh impact craters. This is followed by a summary of our current understanding of impact physics and its major geologic consequences (section 4.1.2). When combined with isotopically-determined ages of

returned lunar samples, the statistical number of lunar craters per unit area provides important constraints on both the relative and absolute ages of various surface units and on the nature of the projectile flux through geologic time (section 4.1.3). Such calculations permit an assessment of cumulative cratering effects by modeling the stochastic nature of repetitive impacts (section 4.1.4).

The importance of impacts on the Moon extends far beyond the simple formation of crater-shaped landforms. The largest impact structures, which are the multiring basins that constitute major topographic and structural features of the Moon, have also served as sites for later volcanic and tectonic activity. Furthermore, the lunar surface materials and deeper crustal rocks that are excavated from impact craters are also processed by impacts in ways that greatly affect their petrographic appearance (Chapter 6), surface debris (Chapter 7), chemical composition (Chapter 8), and physical properties (Chapter 9).

4.1.1. The Morphology of Impact Structures

Terminology. The fundamental shape of an impact feature is that of a bowl-shaped depression (a crater) surrounded by a raised rim. Impact crater shapes vary with crater diameter (measured from rim to rim). With increasing diameter, they become proportionately shallower and develop more complex rims and floors, including the appearance of central peaks and rings. Such morphologic changes are found in craters on all the terrestrial planets and moons (Pike, 1980). Some basic terms for the range of features associated with fresh, uneroded impact craters are illustrated by the examples in Fig. 4.1, and schematic views of various crater features are shown in Fig. 4.2.

The basic morphologic subdivisions of impact structures are (1) *simple craters*, (2) *complex craters*, and (3) *basins*. *Simple craters* are generally bowl-shaped with rounded or, in some cases, small, flat floors (Smith and Sanchez, 1973). They have smooth rims that lack terraces. With increasing diameter, simple craters develop scalloped walls as large masses of rock and regolith are slumped onto a generally hummocky crater floor (Figs. 4.1 c,d).

With larger diameters, simple craters evolve into *complex craters*, which are characterized by terraced and crenulated rims, or by zones of broad-scale (inward) slumping, and by an uplifted central peak or peaks protruding from a relatively broad, flat floor.

On the Moon, the transition from simple to complex craters takes place in the 15–20 km diameter range (Pike, 1977). *Central peaks* are rarely observed in craters <10 km, but most fresh craters >35 km and <100 km have central peaks (Wood and

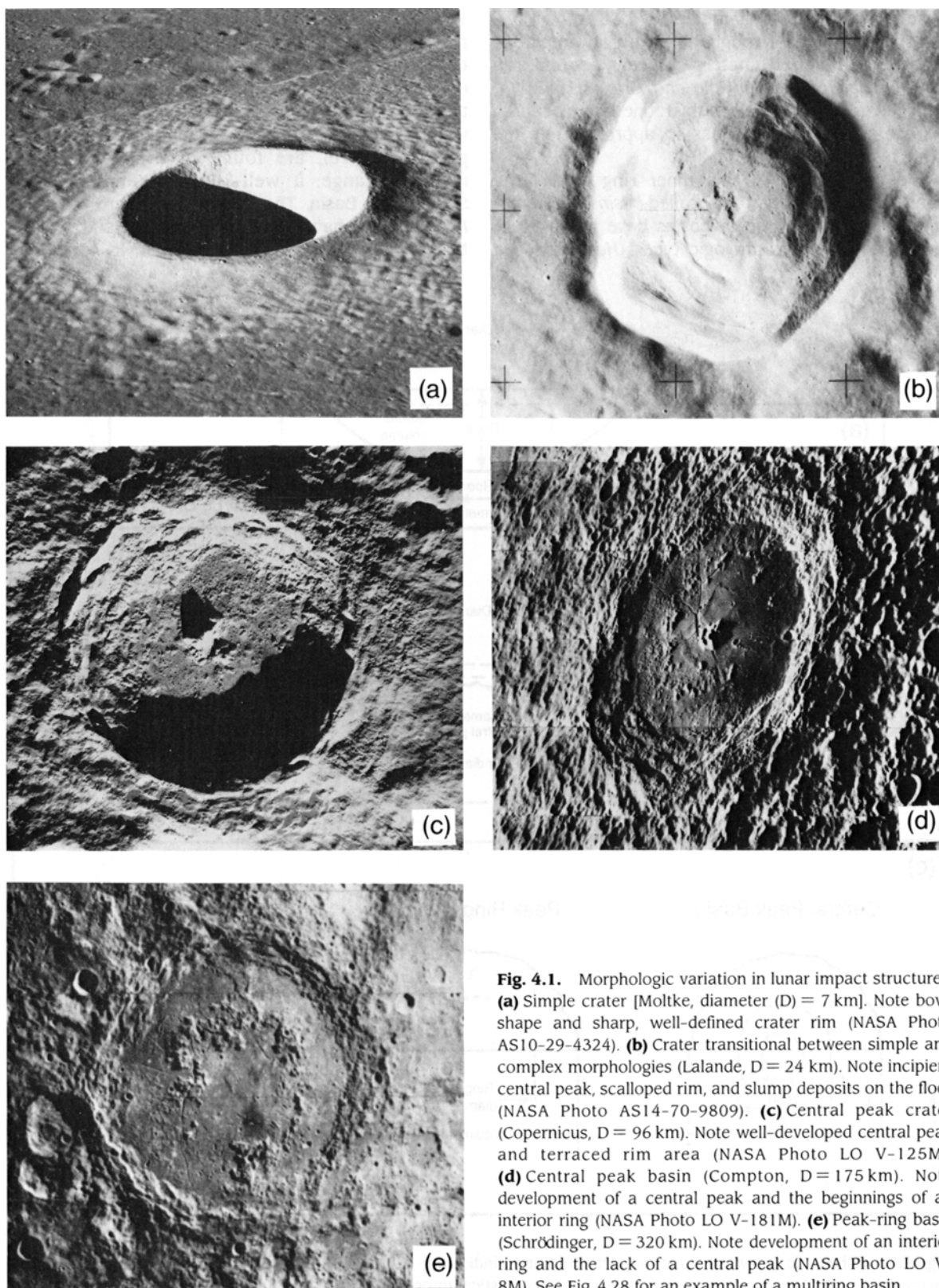


Fig. 4.1. Morphologic variation in lunar impact structures. **(a)** Simple crater [Moltke, diameter (D) = 7 km]. Note bowl shape and sharp, well-defined crater rim (NASA Photo AS10-29-4324). **(b)** Crater transitional between simple and complex morphologies (Lalande, D = 24 km). Note incipient central peak, scalloped rim, and slump deposits on the floor (NASA Photo AS14-70-9809). **(c)** Central peak crater (Copernicus, D = 96 km). Note well-developed central peak and terraced rim area (NASA Photo LO V-125M). **(d)** Central peak basin (Compton, D = 175 km). Note development of a central peak and the beginnings of an interior ring (NASA Photo LO V-181M). **(e)** Peak-ring basin (Schrödinger, D = 320 km). Note development of an interior ring and the lack of a central peak (NASA Photo LO V-8M). See Fig. 4.28 for an example of a multiring basin.

Andersson, 1978). At diameters of >80 km, a concentric zone of floor roughening with an amplitude of several hundred meters appears around the central peak or peaks (Hale and Grieve, 1982). At larger diameters (>100 km) this zone is replaced by a fragmentary ring of peaks in approximately the same region (Figs. 4.1 d,e).

The appearance of this inner ring marks the transition from craters to so-called *basins* (Hartmann and Kuiper, 1962). Impact basins have been subdivided into three morphologic types (Hartmann and

Wood, 1971). *Central peak basins*, such as Compton, are relatively small basins with a fragmentary ring of peaks surrounding a central peak (Fig. 4.1d). They occur in the 140–175 km diameter range and are transitional to peak-ring basins. *Peak-ring basins*, which have a well-developed ring but lack a central peak (Fig. 4.1 e), are found in the 175–450 km diameter range; a well-known example is the Schrödinger Basin. The largest basins are *multiring basins*, which have as many as six concentric rings. Multiring basins are generally more than 400 km in

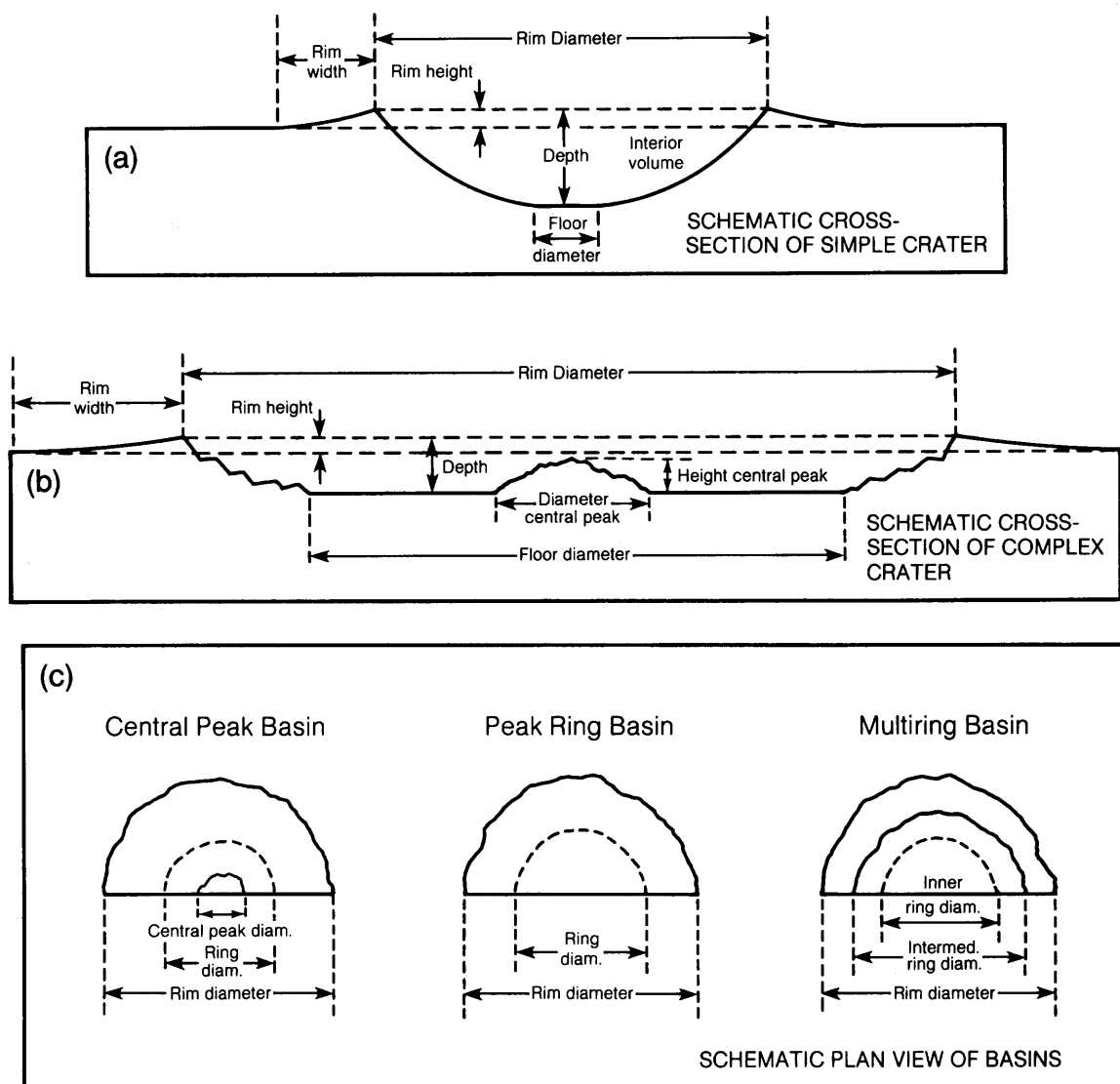


Fig. 4.2. Schematic views of lunar impact structures, indicating principal morphologic elements. (a) Simple crater, (b) complex central peak crater, (c) various basins. For statistical (morphometric) data on these elements, see Table 4.1.

diameter; the best example is the Orientale Basin, which has been only partly flooded by lavas (Fig. 4.28). The definition of diameters for the various basin shapes can vary among workers, depending on the exact criteria and datasets examined.

The most comprehensive classification of lunar crater shapes is that of *Wood and Andersson* (1978). Their catalog, which is based on observations from Lunar Orbiter IV photographs, is a compilation of morphologic and morphometric data for 11,462 craters. In the catalog, crater shape classification is more detailed than that outlined above, and 18 different crater types are recognized. Some, however, represent rare variants. There also is some argument as to whether all observable crater forms represent distinct morphologic types, whether some forms are transitional stages between accepted end members (*Ravine and Grieve*, 1986), or whether some forms are the result of the effects of varying target properties on crater shape (*Cintala et al.*, 1977).

The catalog of *Wood and Andersson* (1978) also includes criteria for the classification of progressively eroded and degraded impact structures. Estimates of "degradation" (extent of erosion) are based on such features as rim continuity, rim sharpness, and infilling of the crater cavity by mass wasting. *Class 1* craters are the freshest and least eroded; *class 5* craters are the most degraded and are only marginally recognizable as impact features. Obviously, the signature of a 1-km-diameter crater is obliterated faster than that of a 100-km-diameter crater. Degradational state and the associated classification become important, therefore, when one evaluates the relative formation ages of specific craters or crater populations (*Soderblom*, 1970; *Wilhelms*, 1985; see also section 4.4).

Morphometry. Morphometric studies are concerned with the measurement of landform shape and dimensions. For fresh lunar craters, they describe the fundamental diameter-dependent variations in crater shape as outlined above, such as the statistical variation of crater depth with rim diameter. Morphometric measurements are based on Lunar Orbiter and higher-resolution Apollo imagery, or on derivative map products such as Lunar Topographic Orthophotomaps.

Detailed measurements of lunar imagery have made it possible to represent the different geometrical characteristics of lunar impact craters by equations of the form

$$y = aD^b$$

where y is a given crater characteristic (e.g., depth, rim height), D is the diameter of the crater (measured from rim to rim), and a and b are constants.

Specific equations for a large number of crater characteristics are summarized in Table 4.1, which also shows variations in such features as the volume of central peaks.

4.1.2. The Cratering Process

Upon impact, the projectile's kinetic energy is transformed into *shock waves* that travel forward from the interface into the target and rearward into the projectile (Fig. 4.3). In the target, particle motion induced by the shock wave accelerates the impacted materials radially downward and outward. At the same time, the projectile is decelerated by shock waves that propagate rearward, opposing the direction of flight. Specific energies of the highly compressed target and projectile materials are increased; upon adiabatic decompression after passage of the shock wave, this increase appears as waste heat. At cosmic impact velocities (15–20 km/sec) and associated pressures (up to several hundred GPa), substantial volumes of the target and virtually all of the projectile may be melted, vaporized, or even ionized. Subsequent unloading from these high-pressure states is initiated by the release waves or *rarefaction waves* that form as the shock wave reaches free surfaces, such as the rear of the projectile or the ground surface at some distance from the impact point. Rarefaction waves modify the initial shock particle motions and ultimately set up a flow field that initiates and eventually completes the actual crater excavation (e.g., *Maxwell*, 1977; *Orphal*, 1977; *Croft*, 1980).

Cratering mechanics. The processes that form small simple craters are well understood from experiments (*Gault et al.*, 1968; *Stöffler et al.*, 1975), calculations (*Maxwell*, 1977; *Orphal et al.*, 1980), and observations at terrestrial and lunar impact structures (*Roddy et al.*, 1977; *Dence et al.*, 1977; *Grieve et al.*, 1981; *Basilevski et al.*, 1983; *Stöffler et al.*, 1985). During early penetration of the projectile, a roughly hemispherical cavity with a radius not much larger than that of the projectile is formed, and most of the impactor's energy and momentum are rapidly transferred to the target (*Holsapple and Schmidt*, 1986). A roughly hemispherical shock front propagates outward from this cavity into the target. Total energy transfer, combined with the radial engulfment of increasing volumes of material and the resultant associated decrease in specific energy, will determine the attenuation rate of the shock wave and the fractional target volumes shocked to specific peak pressures (e.g., *Ahrens and O'Keefe*, 1977).

Interaction of the shock wave with the target's free surface begins very early and essentially at the impact point; a rarefaction wave results. Because the

TABLE 4.1. Morphometric relations for fresh lunar impact craters (see Fig. 4.2).

Crater Characteristic	D, km*	N	Exponent (b)	Coefficient (a)	Source
<i>Simple Craterforms</i>					
Depth	<15	171	1.010	0.196	Pike (1974b)
Rim height	<15	124	1.014	0.036	Pike (1977)
Rim width	<15	117	1.011	0.257	Pike (1977)
Floor diameter	<20	38	1.765	0.031	Pike (1977)
Interior volume	<13	47	3.00	0.040	Croft (1978)
<i>Complex Craterforms</i>					
Depth	12-275	33	0.301	1.044	Pike (1974b)
Rim height	15-375	38	0.399	0.236	Pike (1977)
Rim width	15-375	46	0.836	0.467	Pike (1977)
Floor diameter	20-125	53	1.249	0.187	Pike (1977)
Diameter (central peak)	17-175	175	1.05	0.016	Hale and Head (1979)
Basal area central peak	17-136	19	2.19	0.09	Hale and Grieve (1982)
Height central peak	17-51	15	1.969	0.589×10^{-3}	Hale and Grieve (1982)
Central peak volume	17-51	15	5.078	0.987×10^{-7}	Hale and Grieve (1982)
Central peak volume	80-136	4	3.599	0.397×10^{-5}	Hale and Grieve (1982)
Interior volume	19-150	21	2.31	0.238	Croft (1978)
<i>Basins</i>					
Diameter ring in central peak and peak ring basins	140-435	12	1.125	0.245	Head (1977)
Diameter inner ring in multiring basins	420-1160	13	0.943	0.708	Pike and Spudis (1987)
Diameter intermediate ring in multiring basins	420-1160	13	0.970	0.845	Pike and Spudis (1987)

* This column indicates the range of rim-to-rim crater diameter values (D) used to establish relations for other crater characteristics; N is the number of craters used. Relations are of the form $y = aD^b$, where y is the crater characteristic (e.g., crater depth, rim height, etc.), D is the rim-to-rim crater diameter, and a and b are constants. Linear crater dimensions (depth, height, diameter, etc.) are in km. Volumes (central peaks, crater interiors, etc.) are in km³.

shock-induced particle motions are small when compared with shock-wave and rarefaction-wave velocities, the shocked material near the impact point has not moved substantially by the time the rarefaction waves arrive. The initial shock-produced particle motions are therefore modified because the rarefaction wave fronts generated at the target surface are not parallel with the direction of shock acceleration (other than along the centrosymmetric axis).

Through the interactions of the shock waves and rarefaction waves, the initial radial accelerations in the target are changed to motions with distinct upward components, especially for near-surface strata. A subsurface flow field (Fig. 4.3) is thus established and controls both excavation and ejection processes. In detail, the exact geometry and other aspects of this flow field are poorly understood for impacts. However, qualitatively analogous flow fields occur during explosive cratering events, as described and analyzed for nuclear explosion craters by Maxwell (1977) and for laboratory explosion and impact experiments by Oberbeck (1977).

Components of the target volume that travel along upward and outward flowlines at sufficient velocity to be excavated and thrown above the initial target surface will form crater *ejecta* and will define the *excavation cavity* of the crater. Materials beyond this excavation cavity are also set in motion, but their flow directions and velocities do not result in ejection. These materials are displaced, either by downward compression in the central part of the crater or by structural uplift in the rim area outside the excavation cavity (Fig. 4.3).

At the instant that the shock-induced particle flow ceases, the total excavated and (temporarily) displaced target materials define the so-called *transient cavity*. The latter is substantially deeper than the excavation cavity, but their diameters are similar. This is an important concept: *A crater's maximum depth of excavation is shallower than the maximum depth of the transient cavity.* As the name implies, the latter is a temporary phenomenon. The compressed materials immediately unload, leading to predominantly upward motion in the crater's center. Some of the materials temporarily displaced

as structural rim uplifts are gravitationally unstable and slide downward and inward, thus modifying the transient cavity by collapse. Once all motion ends, the result is a geometrically simple, bowl-shaped cavity that resembles neither the “excavation” nor the “transient” cavity precisely.

Reconstructions of well-studied terrestrial simple craters suggest that the transient cavity has a depth-to-diameter ratio of $\sim 1/3$ (Dence *et al.*, 1977). There is, however, no direct information on the equivalent dimensions of lunar simple craters. The maximum depth of excavation at terrestrial simple craters has been estimated as $\sim 0.14 D$ by Grieve *et al.* (1981) and

as $\sim 0.1 D$ based on a first-order analytical model of Maxwell (1977; see also Croft, 1980), where D is the diameter of the transient cavity.

The transient crater may be an ideal that never truly exists as a physical reality. Computer models, using continuum mechanical code calculations, indicate that maximum cavity depth is reached prior to maximum radial growth (Orphal *et al.*, 1980). As a consequence, incipient rebound of the crater floor may occur before ejection and radial growth are finished. In any case, the brecciated and fractured walls of the transient cavity and the elevated rim area are highly unstable and collapse inward,

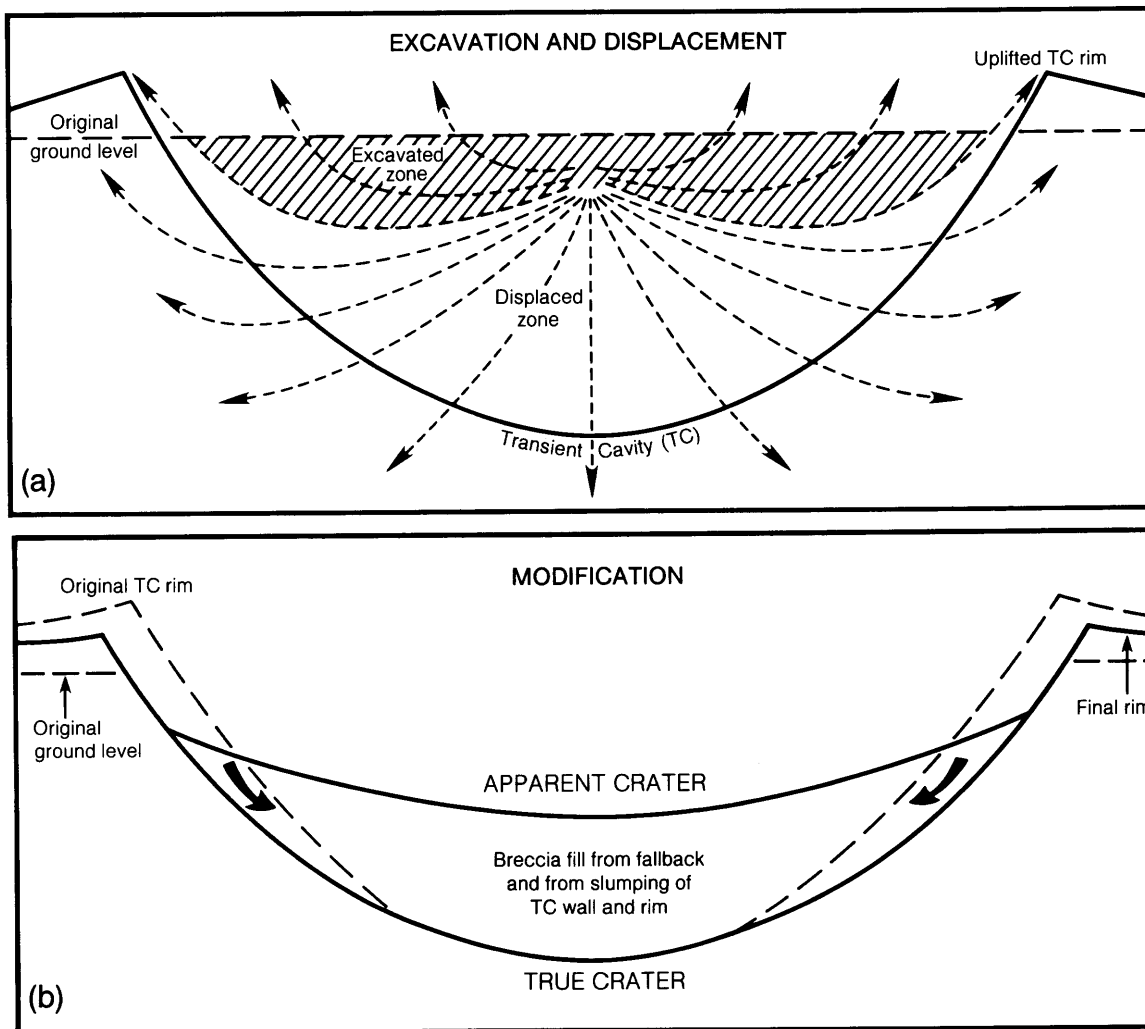


Fig. 4.3. Model of the formation of a simple crater. **(a)** Formation of the transient cavity by a combination of excavation and displacement induced by the cratering flow field, which in turn is established by the shock and rarefaction waves. **(b)** Inward collapse of the transient cavity walls and rim to form an interior breccia lens and the final apparent crater [see text (section 4.1.2) for further details].

enlarging the diameter slightly and partially filling the crater with a lens of brecciated material that is commonly observed in terrestrial simple craters (Grieve and Garvin, 1984; Fig. 4.3). Thus the final form of a simple crater is a bowl-shaped depression underlain by a breccia lens (Fig. 4.3). The visible crater form is known as the *apparent crater*, while the form that includes the continuation of the wall under the breccia lens is known as the *true crater* (Grieve, 1981; Fig. 4.3).

There is less consensus on the details of cratering mechanics during formation of complex craters and basins (Schultz and Merrill, 1981). Considerable observational evidence from complex terrestrial craters (Dence *et al.*, 1977) supports the hypothesis that the rim terraces and central structures are indicative of extensive structural movement. Terraces are clearly composed of material that has collapsed inward from the rim area. Central peaks are uplifted from beneath the transient crater floor (Grieve *et al.*, 1981).

The majority of cratering models for complex craters focus on uplift and collapse hypotheses in which the transient cavity is modified under conditions of low material strength (Melosh, 1977, 1982). The driving forces for modification have been considered to be gravity and elastic rebound (Ullrich *et al.*, 1977; Grieve and Robertson, 1979). Small central uplifts are obscured in lunar craters with smaller diameters than those that display rim terraces (Wood and Andersson, 1978; Pike, 1980), supporting the hypothesis that rebound of the crater floor produces central peaks by inward and upward material flow, which in turn may facilitate rim collapse and terrace formation.

In lunar ring basins the major structural ring is usually interpreted as a collapse feature and taken to be the actual crater "rim" (Figs. 4.2c, 4.28a). However, the formation of additional rings interior and exterior to this main ring, or rim, is not well understood. As the diameter of a complex crater increases, the size of the central peak also increases up to ~80 km diameter (Hale and Head, 1979), where the height appears to stabilize at an equilibrium elevation. At this diameter, concentric floor roughening is obscured in the approximate position at which an interior ring appears in larger-diameter structures (Hale and Grieve, 1982). Observations at terrestrial structures indicate increasing degrees of structural uplift with increasing diameter. Floor roughening, and ultimately an interior ring, may represent the excess volume of uplifted material that could not be accommodated in a central peak.

These observations have led to models of ring formation in which an initial central peak is uplifted beyond its equilibrium height and collapses to form

a peak and ring (Fig. 4.4d). To form additional interior rings, it has been suggested that the central uplifted area may oscillate up and down to produce a series of rings (Murray, 1980). This is a variant of the "tsunami" hypothesis (Baldwin, 1974), in which the rings are likened to frozen ripples formed after throwing a stone into water. Other hypotheses have been offered for basin rings, for example, the "nested crater" hypothesis (Hodges and Wilhelms, 1978). The origin of rings outside the main rim is obscure but some attempts have been made to explain them as a structural discontinuity associated with impact-induced rupturing and fracturing (Croft, 1981). It is clear that our understanding of basin-sized events, which involve energies in the range of 10^{32} ergs (O'Keefe and Ahrens, 1975) or the equivalent of billions of megatons of TNT, is incomplete. Many of the unanswered questions must await detailed on-site geologic investigations of basin rings on the Moon.

At present, the uplift and collapse hypotheses, in which the uplifted material behaves hydrodynamically during modification, appear most promising. These hypotheses are based on the assumption that much of the target material behaves as if it has little or no strength for some time following initial cavity formation, similar to the behavior of experimental craters in water and mud (Gault and Greeley, 1978; Gault and Sonett, 1982). The model of basin formation shown in Fig. 4.4 considers that at least initially the transient cavity is similar to that of simple craters. It is rapidly modified, however, by extensive uplift, while minor near-surface excavation may be continuing. Thus the reconstructed cavity would appear like a sombrero with the volume corresponding to the high crown limited to the central region (Croft, 1981). Whether this model corresponds to reality is speculation. It does, however, have points in common with some observational data at smaller terrestrial structures and with cratering experiments in low-strength materials.

The initial cavity shape of a ring basin is related to excavation depth. This concept is especially important in trying to establish the source of lunar samples, all of which have been collected as loose fragments on the surface. Such studies are especially important in two areas: attempting to estimate depths from which deep-seated fragments have been excavated by impact basins (Spudis, 1984), and attempting to construct a lunar stratigraphy (Wilhelms, 1985) from the isolated fragments sampled by astronauts and robot missions.

A lack of consensus still exists on these matters, partly because of some confusion about terminology and partly from disagreement over the details of cratering mechanics for large basin-forming events.

In particular, there has been disagreement over which ring in a multiring structure, if any, corresponds to the rim of the original excavated cavity. These difficulties can be illustrated by considering the range of estimates in the literature for the maximum diameter and depth of excavation for the Orientale Basin (Table 4.2; see also Fig. 4.28).

In summary, the processes occurring during formation of relatively small, simple, bowl-shaped craters appear to be well understood from terrestrial and lunar field observations, laboratory experiments, and theory (see the summary by *Holsapple and Schmidt*, 1986). The phenomena associated with complex craters, especially with basin-forming impacts, are poorly understood, despite considerable efforts to "scale" observations from controlled laboratory experiments to large natural structures.

The problems in such scaling efforts arise less from dimensional aspects than from uncertainties about material properties and behavior, for example, (1) the finite (tensile) failure strengths of severely shocked rocks (*Curran et al.*, 1977), (2) possible

differences in energy partitioning between laboratory experimental velocities and impacts at cosmic speeds (*Ahrens and O'Keefe*, 1977), and (3) estimating the proper balance between work done against the intrinsic dynamic strength of rocks *vis-à-vis* work done against the prevailing gravity field. After all, a crater can form only if rock is broken and lofted out of the growing cavity. At small cratering scales the strength parameter dominates, but the growth of large structures is controlled primarily by gravity.

Such theoretical scaling calculations are critical to understanding the cratering process. They are important in attempts to reconstruct the characteristics (size, velocity, density) of the populations of projectiles responsible for an observed crater population. Ideally, one would like to relate some measured crater properties (e.g., diameter) to the total kinetic energy of the projectile and thus determine the mass, momentum, and velocity of the projectile that formed it. Such reconstruction is difficult at present and is still highly model-dependent. Indeed, as illustrated by the Orientale

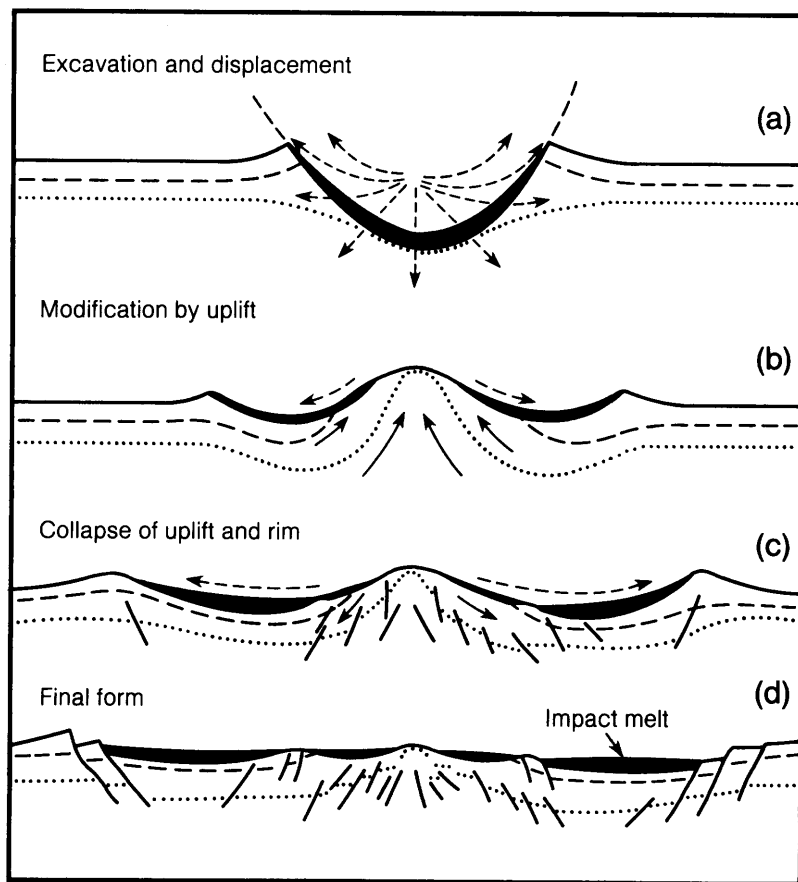


Fig. 4.4. Possible model for the formation of an impact basin with a central peak and interior ring. **(a)** Excavation and displacement to form a transient cavity initially similar to that of a simple crater. **(b)** Modification of the transient cavity by uplift of the cavity floor above the original ground surface, accompanied by minor near-surface excavation. **(c)** Collapse of the overheightened central peak uplift. **(d)** Formation of outer final rim by downfaulting to form terraces and the appearance of an interior ring, which contains the excess of the originally uplifted material that could not be accommodated in the central peak. See text for further details and alternate models (after *Grieve et al.*, 1981).

TABLE 4.2. Estimates of maximum excavation diameter and depth for the Orientale Basin (Fig. 4.28a).

Excavation Diameter, km	Morphologic Feature Used to Estimate Diameter of Excavation	Excavation Depth, km	Source
—	—	130	<i>Dence (1973), as cited by Head et al. (1975)</i>
600	Outer Rook Mts.	85	<i>Moore et al. (1974)</i>
620	Outer Rook Mts.	6–20	<i>Head et al. (1975)</i>
850	Cordillera Mts.	85	<i>Hodges and Wilhelms (1978)</i>
850	Cordillera Mts.	—	<i>Murray (1980)</i>
500–600	Inner-Outer Rook	50	<i>Spudis et al. (1984)</i>
480	Inner Rook Mts.	50	Terrestrial analogy, calculated from <i>Grieve et al. (1981)</i>

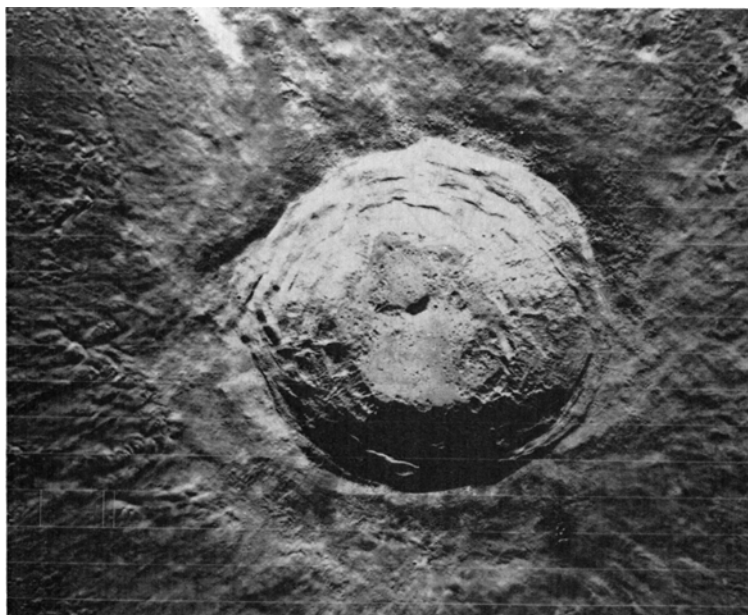
Basin (Table 4.2), there is not even consensus on what feature marks the rim of the original excavation cavity.

The nature of ejecta. Ejection of debris from an impact crater is a remarkably ordered process. With increasing radial distance from a crater, the material ejected from the crater (*ejecta*) forms successively continuous deposits, discontinuous deposits, and rays (Fig. 4.5). Materials ejected early in the cratering process originate close to the target surface and close to the point of impact. Pressure gradients are highest in this zone, and the ejecta are therefore dominated by small fragments traveling at high speeds. They also take off at relatively high ejection angles. As the excavation process continues, mate-

rials of larger average size, slower velocity, and lower ejection angle emanate from the growing cavity. While individual ejecta fragments follow their own ballistic trajectories, they cumulatively form a relatively thin, coherent “curtain” of material, as illustrated in Fig. 4.6 (*Shoemaker, 1962; Oberbeck, 1975*). There is distinct order in such an ejecta curtain; the near-surface target strata produce a relatively fine-grained high-velocity component, with steep take-off angles, higher in the curtain. More deepseated target strata occur predominantly as coarser fragments and boulders at the curtain’s base.

Both theory and models of cratering predict that ejecta deposited near the crater rim should be coarser grained than ejecta far from the rim. This

Fig. 4.5. The well-preserved central peak crater Aristarchus (D = 40 km). The crater is surrounded by a hummocky, continuous ejecta deposit. At greater radial distance, the deposits become discontinuous, as evidenced by chains and clusters of secondary craters. Near the limit of the lobate continuous deposits, the secondary craters are partially filled and draped by mixed primary ejecta and by local materials that moved outward by ground-hugging flow. Also note the well-developed wall terraces and other evidence for slumping in the crater interior (NASA Photo LO V-198M).



prediction has been confirmed by observations on the maximum size of ejecta blocks (Moore, 1972; Table 4.3) and by the decreasing number of discernible blocks in lunar photographs with increasing distance from the crater (Cintala *et al.*, 1982).

This relation between the original position of an ejecta fragment within the target and the resulting ejection velocity, ejection angle, and particle size produces a high degree of order during ejecta deposition. Deep-seated, coarse materials barely make it over the crater rim and compose essentially the coarse rim deposits, while materials of decreasing target depth are deposited at increasingly larger radial distances. This situation produces an inverted stratigraphy in the ejecta deposits, relative to the stratigraphy in the original target. Any radial traverse from the periphery of an ejecta blanket toward the crater rim will encounter materials from progressively deeper target strata.

This concept, which has been demonstrated at terrestrial impact structures (e.g., Hörz *et al.*, 1983) is paramount for any geologic exploration of the lunar surface (Shoemaker, 1972; Gault *et al.*, 1968; and many others). For example, it is possible to use the morphometric information summarized in Table 4.1 to determine that the near-rim deposits of a specific crater originated at or close to the bottom of the excavation cavity and thus at some absolute depth. A series of craters, with increasingly larger diameters, may thus be used to probe deeper and deeper formations in a given geologic terrane, thus enabling reconstruction of first-order stratigraphic and structural relationships at depth principally from simple surface observations. Such considerations indeed greatly affect our current perception of the lithologic make-up of the lunar crust based on rocks and remote-sensing information gathered from the surface (Spudis *et al.*, 1984; Wilhelms, 1985).

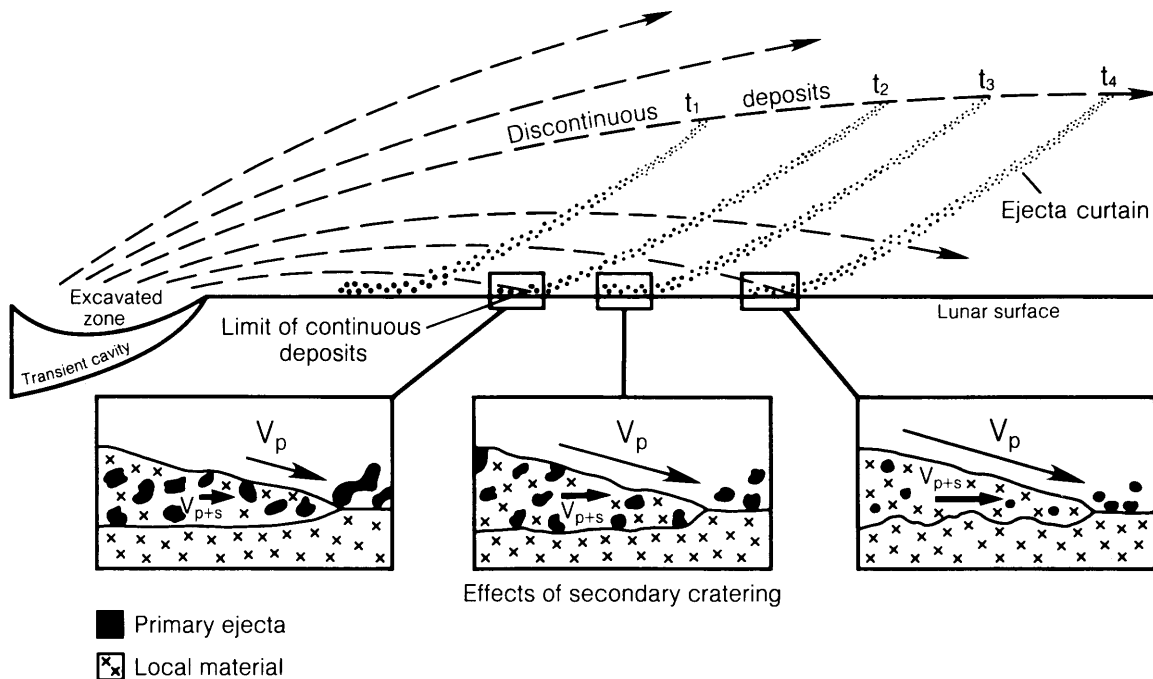


Fig. 4.6. Ejection processes and interaction of ejecta with the lunar surface. Ejecta leave the crater cavity along discrete, relatively shallow ballistic trajectories. At any given time (t) these trajectories define an outrunning ejecta curtain. Coarse-grained, low-velocity ejecta travel along low-angle trajectories and are concentrated at the base of the curtain. They impact close to the crater and excavate modest amounts of local substrate material (see insert; V_p = impact velocity of ejecta; V_{p+s} = radial flow velocity of the resultant debris surge combining "primary" and "secondary" ejecta). Finer-grained fragments reside higher in the ejecta curtain, having been ejected at increasingly higher V_p and steeper angles. As the curtain sweeps radially across the surrounding target, higher-velocity ejecta impact the surface causing local materials to be incorporated in the debris surge, resulting in increasingly higher flow velocities of the debris surge (after Oberbeck, 1975).

TABLE 4.3. Dimensional relations of crater ejecta.

Crater Characteristic	D, km*	N	Exponent (b)	Coefficient (a)	Source
Radial distance of continuous ejecta	1.3-436	84	1.006	1.169	Moore et al. (1974)
Radial distance of continuous ejecta	0.56-1300	8	0.976	1.064	Oberbeck et al. (1974)
Distance rays can be traced from rim	3.2-132	50	1.25	4.41	Moore et al. (1974)
Maximum diameter of ejecta blocks	0.1-98	60	0.66	2.99×10^{-2} 9.97×10^{-3}	Moore (1972)
Thickness of ejecta at the rim*	1.2-970	5	0.74	0.014	McGetchin et al. (1973)

* This column indicates the range of rim-to-rim crater diameter values (D) used to establish relations for other crater characteristics. N is the number of craters used. Relations are of the form $y = aD^b$, where y is the crater characteristic (e.g., crater depth), D is the rim-to-rim crater diameter, and a and b are constants. Linear dimensions (crater diameter, distances, etc.) are in km.

†Includes terrestrial crater and nuclear explosion crater data.

The ejecta deposits surrounding impact sites are generally highly centrosymmetric, regardless of the angle at which the projectile struck the surface. This condition reflects the fact that, for most impact angles, the shock and rarefaction waves are propagated with near-spherical symmetry. Experiments summarized by Gault (1973) indicate that, at cosmic velocities, projectile trajectories inclined at $<15^\circ$ to the local horizontal are required to produce elongated, noncentrosymmetric crater cavities and associated, noncentrosymmetric ejecta blankets. Therefore, for most craters, the ejecta distribution is generally centrosymmetric, and three "facies" can be recognized with increasing radial distance (see, e.g., Moore et al., 1974 and Fig. 4.6).

1. The *continuous ejecta*, deposited closest to the crater, completely drape all preexisting ground around the impact site. The extent of such continuous ejecta blankets increases linearly with crater diameter (Moore et al., 1974). The outer periphery of the continuous ejecta is lobate and grades into the zone of discontinuous ejecta.

2. *Discontinuous ejecta* deposits are characterized by patchy and localized deposition of ejecta material. These deposits frequently contain shallow and elongate *secondary craters* that tend to occur in clusters.

3. *Ejecta rays*, which are an extreme form of discontinuous ejecta deposits, occur beyond the zone of discontinuous ejecta as relatively thin, long streaks oriented radially to the crater. For large lunar craters, such as Copernicus and Tycho, these streaks may extend over a substantial fraction of the lunar

globe, while ejecta rays emanating from large ring basins may extend over the entire surface of the Moon.

The ejecta thickness at the crater rim and the variation of that thickness with crater diameter in different craters has been estimated from both lunar and terrestrial data (Table 4.3). One relationship derived from both lunar and experimental craters, including nuclear explosion events, is

$$t = 1.7 \times 10^{-3} r^3 D^{2.74}$$

where t is ejecta thickness at increasing range from the crater center, r is radial range from the crater center, and D is crater diameter (all units in kilometers; McGetchin et al., 1973). Unfortunately, predictions from this relationship for the most important ejecta deposits on the Moon, those from the large multiring basins, can be 'ambiguous. The crater diameter in the relationship is the diameter of the excavated cavity, estimates of which, as noted previously, can vary widely, as in the case of Orientale (Table 4.2). Pike (1974a) has also called into question the validity of the relationship defining ejecta thickness at the crater rim because it is based in part on nuclear explosion craters, which may not be exactly analogous to impact craters.

Secondary craters. Based on laboratory impact experiments related to ejecta dynamics, Oberbeck (1975) was able to expand on the early calculations by Shoemaker (1962) to estimate the fraction of crater ejecta that travels at sufficient velocities to produce secondary craters upon landing. This fraction increases with increasing crater diameter. In

fact, the cumulative volume of material excavated by these secondary impacts can exceed the primary crater volume, because low-velocity impactors (such as ejecta) excavate more efficiently than high-velocity meteoroid projectiles, which partition large fractions of their energy into waste heat.

This model for secondary crater formation leads to the conclusion that large-scale ejecta blankets are mixtures of material from the primary crater and additional material from relatively local sources that served as target(s) for the secondary craters. As illustrated in Fig. 4.6, this local fraction *increases* with radial range, because primary ejecta velocity increases systematically with distance. Many large-scale, mappable lunar ejecta deposits, especially those associated with basins, may be entirely dominated by locally excavated materials (e.g., Morrison and Oberbeck, 1975; Hörz et al., 1983; Pieters et al., 1986). For this reason Oberbeck (1975) suggested using the term "continuous deposits" rather than "ejecta."

Shock metamorphism. During a typical lunar impact the shock pressures in the target rocks readily exceed millions of bars. Such pressures are generally expressed in GPa (1 GPa = 10 kbar or 150,000 psi). During impact events, large volumes of

the target are subjected to pressures of tens to hundreds of GPa. Such high pressures are not known from internally-driven processes, especially within planetary crusts (see Fig. 4.7). In addition, temperatures and strain rates in impact events can be orders of magnitude higher than those produced by internal processes. Rocks traversed by shock waves respond irreversibly to these unusual conditions by producing unique deformation features and phase changes known collectively as *shock metamorphism* (French and Short, 1968).

An example of calculated shock pressures for representative impact conditions on the Moon is illustrated in Fig. 4.8 (Ahrens and O'Keefe, 1977). This figure illustrates how the peak pressure generated at the target/projectile interface attenuates (along the vertical axis of symmetry). Such calculations form the basis for estimating the fractional crater volumes that are subjected to specific shock stresses and the associated thermodynamic states of the compressed target and projectile materials.

At high shock pressures, a significant amount of shock energy is deposited in the target rocks, raising their temperatures far above the melting or vaporization points. Model calculations indicate that extensive melting and vaporization occur in a typical

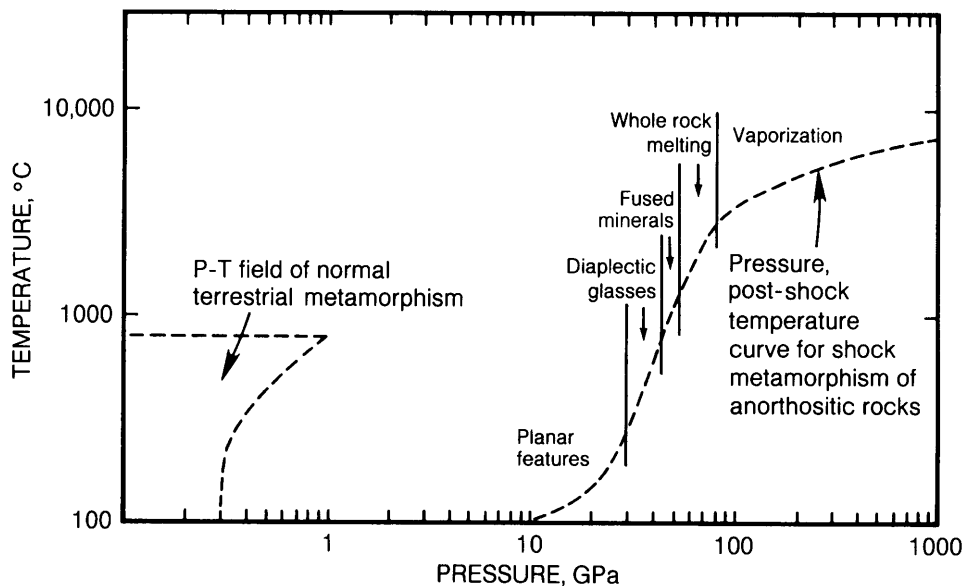


Fig. 4.7. Comparison of pressures and temperatures typical for internally driven metamorphism of crustal rocks on Earth with those characteristic of shock-induced metamorphism. The range of shock pressures for specific shock deformation effects and phase transitions apply to the feldspar-rich rock, anorthosite. Shock metamorphism also differs from internally driven metamorphism by orders of magnitude in timescales and strain-rates. Relatively modest stresses and temperatures may be generated and sustained in the Earth's crust for millions of years; in contrast, shock metamorphism operates on timescales of minutes, seconds, or less, depending on crater size (after Stöffler, 1971).

pressure (along the vertical axis) in a gabbroic anorthosite (igneous rock type) target impacted by gabbroic anorthosite projectiles at 5, 15, and 45 km/sec impact velocity. The radial distance (R) is normalized to the diameter of the projectile (R_0). Note that (1) absolute peak pressure is strongly related to impact velocity; (2) the decaying shock is divided into (a) a near-field attenuation, characterized by relatively slight pressure decay impact. Vapor masses on the order of a few projectile masses and melt masses about 100 times the projectile mass can be generated (O'Keefe and Ahrens, 1975; Orphal et al., 1980).

The degree of shock metamorphism produced by a given shock pressure depends heavily on a material's behavior at ultrahigh pressures and temperatures, i.e., on its so-called *equation of state*, which relates such parameters as compressibility, specific energy, entropy, specific volume, and phase changes at such conditions (e.g., Kinslow, 1970; Marsh, 1980). The transition from elastic to plastic behavior of dynamically loaded rocks and minerals occurs at relatively high stresses, typically on the order of 5–12 GPa. At pressures between 40 and 100 GPa thermal effects begin to dominate, and melting begins. Pressures exceeding 150 GPa will cause vaporization; ionization will occur at a few hundred GPa.

At shock stresses <10 GPa, crystals of most minerals, especially silicates, respond by brittle failure, producing fractures, shattering, microbrecciation, mosaic textures, and occasionally twinning (e.g., in ilmenite; Sclar and Bauer, 1973; Fig. 4.9a). These microdeformations are not readily distinguished from those generated by other means, for example, tectonic deformation (Stöffler, 1972, 1974; Bauer, 1979). However, the development of unusual striated

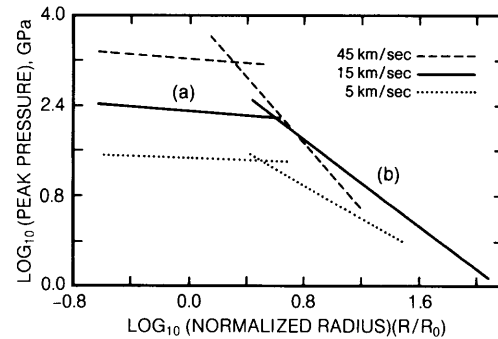
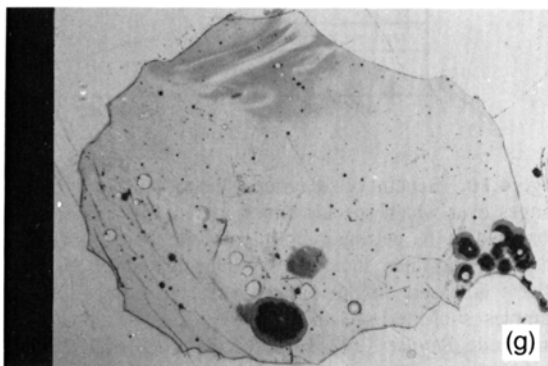
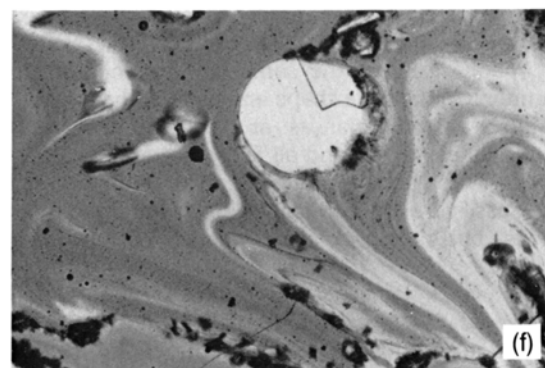
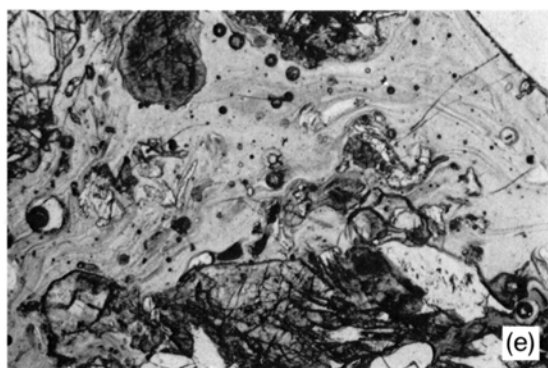
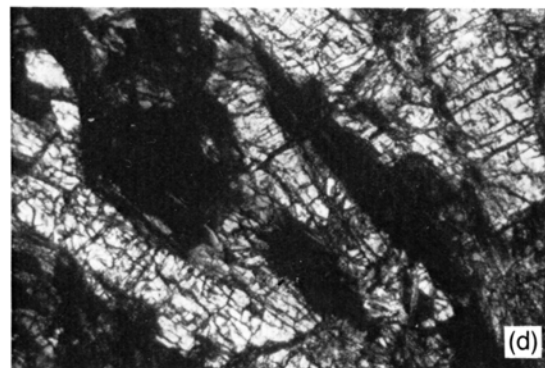
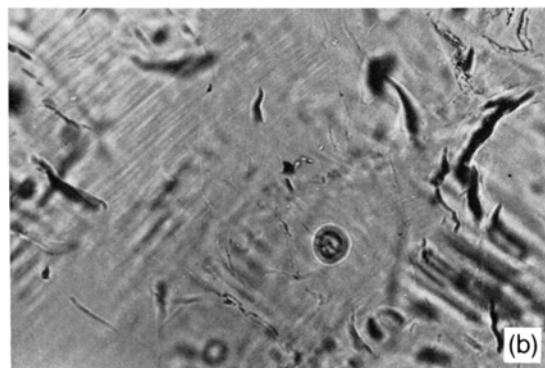
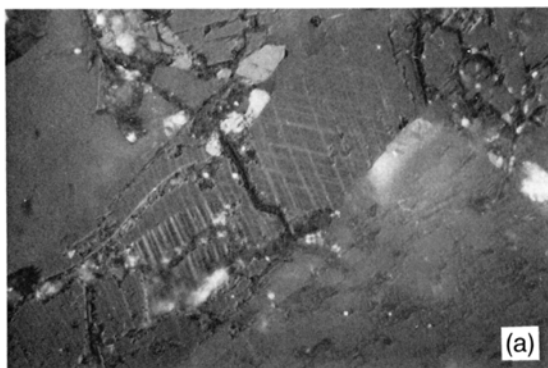


Fig. 4.8. The attenuation of the peak shock with distance, and (b) a far-field regime of relatively rapid pressure decay; (3) the near-field attenuation rate is relatively insensitive to impact velocity, but the far-field rate increases with increasing impact velocity. As a consequence, energetically equivalent impacts caused by projectiles of different sizes and velocities will not necessarily produce identical effects in the target (after Ahrens and O'Keefe, 1977).

Fig. 4.9. Typical shock-metamorphic effects in lunar rocks and minerals, arranged in order of increasing shock pressure from (a) through (h). (For systematics of the lunar rock numbering system see section 2.2.) FOV is field of view (horizontal dimension). (a) Shock-induced twinning of ilmenite indicates modest shock-stress (<10 GPa). Lunar rock 10085,319; reflected light; FOV = 0.22 mm. (b) "Planar elements" (shock lamellae), shown here in a lunar feldspar, are among the most diagnostic shock features formed at pressures of 10–30 GPa. Lunar rock 79155; transmitted light; FOV = 0.22 mm. (c) "Diaplectic feldspar glass" (white areas); plane polarized light (see (d)). (d) Identical field of view as (c) under crossed polarizers; the isotropic feldspar areas are black, revealing their amorphous, glassy state. Note that the original outlines of feldspar grains are perfectly preserved, which implies that no melting took place during formation of these unusual glasses. Such glasses are known only from shocked rocks and form at pressures of 30–45 GPa. The glassy feldspar is surrounded by highly fragmented, but still crystalline, pyroxene; such intense fracturing (mosaicism) is typical of shocked pyroxene, but it is not a unique shock indicator. Lunar rock 15684; FOV = 2.2 mm. (e) Incipient shock-melting in lunar rock 15684. The schlieren-rich, flow-banded nature of these glasses indicates that they are chemically heterogeneous; they are in fact composed of different proportions of feldspar and pyroxene melts. The contacts with mineral grains in the host rock are thermally eroded (i.e., rounded) and in various stages of disaggregation, and abundant broken-off fragments (clasts) occur in the melt. Such mixed melts are typical of shock-stresses of 45–60 GPa. Plane-polarized light; FOV = 2.2 mm. (f) Heterogeneous "whole rock" impact melt produced by conversion of the entire target rock to a melt at high shock pressures (>80 GPa). Flow lines (schlieren) of different colors generally differ only modestly in chemical composition. Many schlieren are the result of incomplete clast digestion by the probably superheated melt. Lunar sample 65315,82; FOV = 2.2 mm. (g) Relatively homogeneous glassy "whole rock" impact melt; note, however, that some faint schlieren are still present, at least locally. This is one of the optically most homogeneous lunar impact melts and as such is somewhat atypical [(f) is more typical of impact-produced melts and glasses.] Lunar sample 60095,34; plane-polarized light; FOV = 1.8 mm. (h) Completely crystallized impact melt. Depending on the cooling history of an impact melt, different types of crystallization products and textures may be produced, resulting in a wide variety of rock textures. Many textures may be similar to those that develop during the cooling of normal igneous melts, such as this "ophitic-subophitic" example, a textural term derived from the study of conventional basaltic lavas. Lunar rock 68415; plane-polarized light; FOV = 2.2 mm.



conical fractures (*shatter cones*) in rocks shocked at about 5–10 GPa is apparently a unique shock wave effect.

Solid-state deformations that are diagnostic of shock are generally produced at shock levels >10 GPa. Pressures in this region exceed the transition between low-pressure elastic failure and the high-pressure *Hugoniot Elastic Limit*. Two prominent and easily observed deformation phenomena develop only under such shock conditions: the so-called *shock lamellae* (also called *planar elements* and *planar features*) and the isotropic mineral *diaplectic glasses* (also called “*thetomorphic*” glasses). Shock lamellae are microscopic sets of parallel deformation planes a few micrometers in width that occur along specific crystallographic planes (Fig. 4.9b) (see Hörz, 1968; Roberts, 1968). These features develop prominently in quartz and feldspar, but they are also known from pyroxenes and olivines (Chapter 5). At pressures between 20 and 30 GPa, one commonly observes multiple sets of shock lamellae of differing crystallographic orientations in individual mineral grains. The crystallographic orientation of shock lamellae in quartz is related to peak shock pressure, and the observed fabric of shock lamellae may be used to estimate the pressure history of naturally-shocked samples (e.g., Robertson and Grieve, 1977).

Diaplectic glasses are produced at higher shock pressures by *in situ* conversion of the crystal into an amorphous glass of the same composition, which commonly retains the shape and habit of the original grain. Diaplectic glasses are only known from tectosilicates (quartz and all feldspars), and they are formed over a pressure range of about 28 to 45 GPa. The glasses are optically isotropic and amorphous to X-rays, but they lack any evidence of flow and melting.

Both shock lamellae and diaplectic glasses are considered the most unique and diagnostic solid-state deformation features produced by shock waves. There is an extensive literature describing their detailed mechanisms of formation and especially the structural states of diaplectic glasses, which possess, for example, higher densities and refractive indexes than glasses produced from quenched silicate melts (see, e.g., French and Short, 1968; Stöffler, 1972, 1974; Hörz and Quaide, 1973; Arndt et al., 1982; Ostertag 1983; Stöffler, 1985).

Above 50–70 GPa, postshock temperatures are high enough to melt most minerals and rocks (Figs. 4.9e–h and 4.10). Feldspars may display signs of incipient melting at pressures as low as 45 GPa (Stöffler, 1972; Schaal and Hörz, 1977). Such mineral-specific melting is also a diagnostic indicator of shock processes; monomineralic melts are essen-

tially unknown in more conventional melt processes that are governed by equilibrium thermodynamic processes. Incipient melting during shock generally favors the phases with highest compressibility, unlike phase-equilibrium melting. For instance, the juxtaposition of genuine feldspar melts with intact mafic minerals, which have lower intrinsic melting temperatures, is commonly observed in shocked rocks. Furthermore, shock melting commences at grain boundaries, especially in porous materials, where reverberations of the shock wave may deposit extra waste heat. As a result, highly localized melts (*mixed mineral melts*) are produced that are clearly mixtures of the two neighboring phases. As illustrated in Fig. 4.11, shock-induced melting phenomena occur over a wide pressure range, and the amount of melt produced is related to peak pressure. At pressures at or above 70–80 GPa, depending somewhat on the nature of the major constituent minerals, the entire rock will be melted to form a glass.

There are substantial differences between the effects of shock on coherent crystalline materials (rock), or on porous, granulated materials (e.g., lunar soil) of the same composition (Kieffer, 1971, 1975; Ahrens and Cole, 1974). Shock-recovery experiments indicate that, in porous targets, intragranular solid-state deformation effects are less obvious and

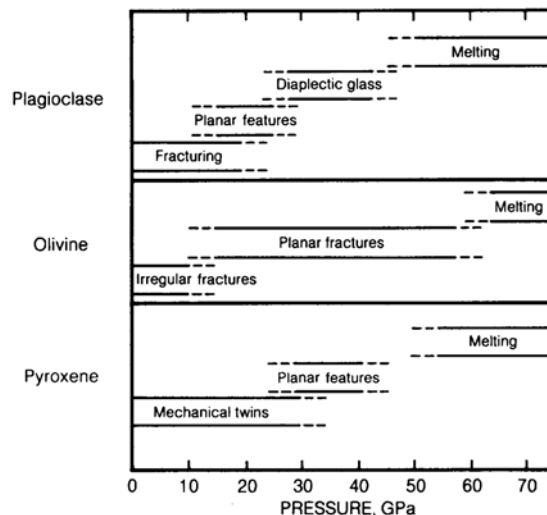


Fig. 4.10. Schematic diagram illustrating the pressure ranges over which specific shock-metamorphic effects, as observed in the petrographic microscope, appear in major rock-forming lunar minerals. Pressure calibration of these effects is based on the optical analysis of single crystal samples subjected to laboratory shock waves of known amplitude (Stöffler, 1972, 1974; Schaal et al., 1979; Reimold and Stöffler, 1978; Bauer, 1979; Ostertag, 1983).

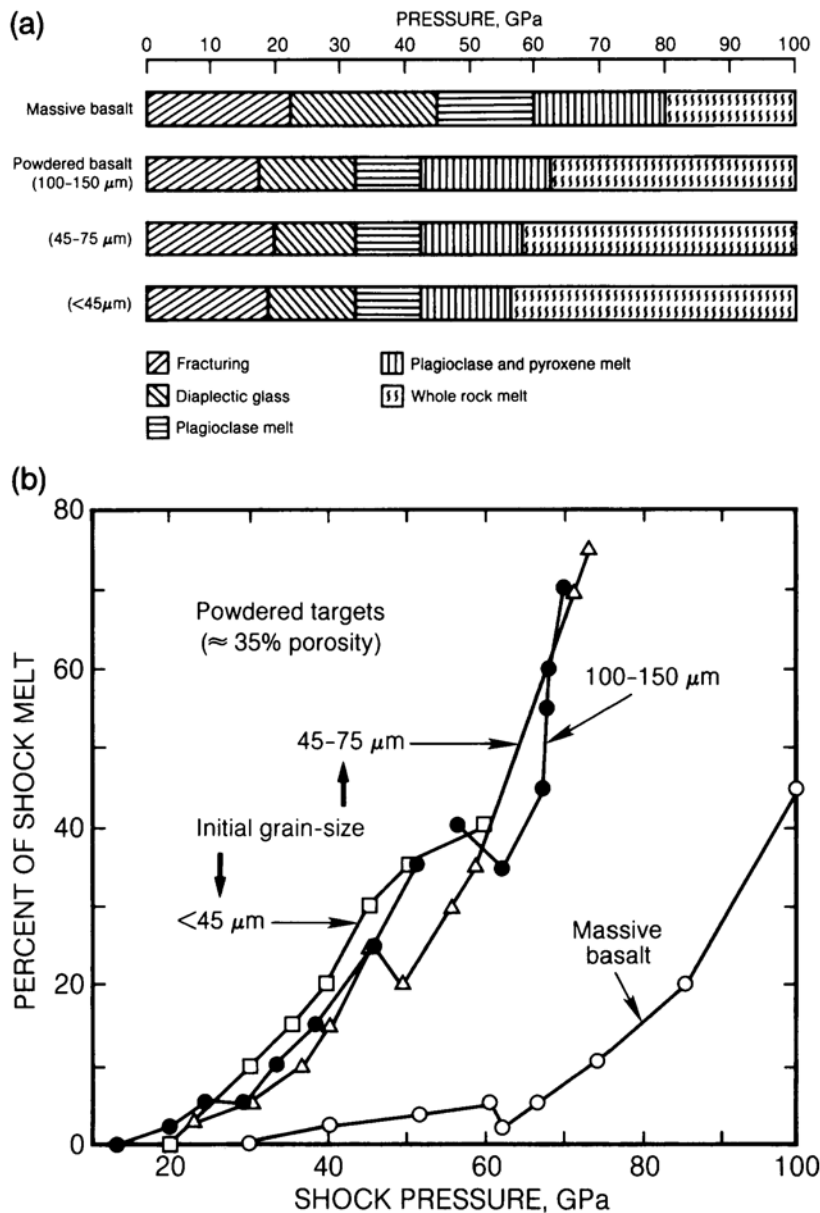


Fig. 4.11. Schematic diagram of experimental shock pressure ranges over which particular shock effects appeared in a typical, nonporous lunar basalt and in powders of various grain-sizes (regolith analogs) prepared from the same sample. **(a)** Summary of petrographic observations. Note that qualitatively similar effects occur in both the dense and powdered samples, but the threshold pressures for development of equivalent features are lower in the powdered materials. **(b)** Detailed comparison of the melting behavior of dense, nonporous basalt and its powdered, porous equivalent. Note that powdered samples melt with substantially greater ease than nonporous targets (after Schaal *et al.*, 1979).

intergranular effects dominate (Gibbons *et al.*, 1975; Schaal *et al.*, 1979). In addition, the onset of melting occurs at lower shock pressures in porous or granulated materials. Intergranular melts develop in powdered lunar basalt at shock pressures as low as 20 GPa, and whole-rock melts are formed at 55 GPa (Fig. 4.11). This more pronounced shock melting in lunar regolith and similar materials, compared to more coherent equivalents, is due to increased reverberation(s) of the shock wave at the free

surfaces of component grains, where the density contrast between "solids" and "voids" is maximized. This condition leads to highly localized stress concentrations and to a highly heterogeneous deposition of energy, including the local production of high residual temperatures at relatively modest average shock stress.

The overall response of individual rocks to shock waves is controlled largely by the response of their major component minerals. While differences are

observed between diverse rock types, all rocks become completely molten at or above 100 GPa. Impacts at cosmic velocities will produce such pressures within a large volume of target, so that a significant part of the target will therefore be melted no matter what its detailed lithology and mineral composition.

Impact melts. The above considerations have important implications for naturally-occurring *impact melts*, a term that designates completely molten target material produced by the intense shock waves of meteoroid impact. This section emphasizes lunar impact melts, which constitute a prominent rock type in the Apollo sample suite. Material identified as impact melt composes some 30–50% of all hand-specimen-sized rocks returned from highland landing sites and some 50% of all soil materials, including mare collections (Ryder, 1981). How can such impact melts, which range in texture from completely noncrystalline glasses to completely crystalline rocks, be distinguished from internally-derived volcanic melts and their crystallization products?

The *melt zone* of a crater is the region within which shock pressures are high enough (~80 GPa or higher) to produce complete melting of the target rock. Even if this zone is composed of dramatically different lithologies, all will melt, and the melt will become part of the material that flows during the crater's excavation stage. Detailed studies of terrestrial impact melt sheets (e.g., Masaytis *et al.*, 1975; Dence *et al.*, 1977; Phinney and Simonds, 1977; Grieve, 1981; and many others) show that the divers melts tend to be homogenized, and that the resulting glasses or crystalline rocks, depending on cooling rate, represent remarkably homogenized mixtures of the original target lithologies.

Chemical composition is therefore one criterion applied to distinguish impact melts from conventional igneous rocks. The criterion is simple: Impact melts are simple mixtures of preexisting target rocks. In many cases, the mixed compositions of impact melts have unique characteristics that cannot be produced by conventional internal melting processes, which involve the partial melting of a compositionally restricted source rock.

A second criterion for recognizing impact melts is the special nature of rock and mineral inclusions and the effects they produce on the surrounding melt. During crater excavation, the impact melt bodies move along the crater floor and walls. In the process they pick up numerous inclusions (*clasts*) of the target rocks ranging in size from large blocks to small mineral grains. Impact glasses, which obviously cooled and quenched rapidly, always contain large amounts of these clasts, which may

extend down to submicroscopic sizes (e.g., Stahle, 1972). These clasts frequently show distinct shock effects. Partial digestion of these clasts by the melt typically results in texturally heterogeneous glasses with variegated streaks (*schlieren*), consisting of glasses of different compositions.

Progressively more crystallized impact melts, reflecting slower cooling rates, display an increased tendency to digest this clastic material. In completely crystallized impact melts, clastic material may no longer be observed on the scales of thin section and even hand specimens (millimeter to centimeter), yet larger clasts are always observed in the field (Phinney and Simonds, 1977). However, the digestion of these relatively cold clasts by the superheated impact melt produces local disturbances of the average thermal environment within the cooling impact melt sheet, giving rise to textural heterogeneities on unusually small scales (<1 cm) relative to those observed in rocks produced by igneous processes. In addition, all clasts found in impact melts are samples of the primary target rocks and can be used to determine the exact nature of those rocks and to model the melting process. As described by Stahle (1972) and Phinney and Simonds (1977), the observed clast population does not necessarily reflect the exact mixture of lithologies originally present in the melt zone. The surviving clasts are biased toward "cold" (unshocked) and refractory starting materials.

A third criterion for distinguishing between conventional igneous rocks and impact melts is the identification of projectile remnants in the impact melts, as pioneered by Anders and coworkers (e.g., Anders *et al.*, 1973). In the impact process, the entire projectile suffers shock stresses sufficient to melt, if not to vaporize and ionize, virtually all of the projectile. Part of this melted and vaporized projectile will be disseminated throughout the melt zone.

Chemical analyses have been the most effective means of detecting such projectile remnants in impact melts. In particular, siderophile elements such as Ni, Co, Ir, Au, Pt, and others have been especially diagnostic. They are highly enriched in meteorites relative to the indigenous target rock (lunar or terrestrial) concentrations, so that small amounts of a projectile can be readily detected in an impact melt. Furthermore, specific elemental ratios differ as well between and among diverse classes of meteorites, allowing the projectile type to be identified from its chemical signature in the impact melt.

For these reasons, siderophile elements have been used extensively as clues in identifying melts of impact origin on the Moon (see section 6.3) and on the Earth. The siderophile content in lunar and

terrestrial melt rocks can be used to demonstrate an impact origin by detecting an enrichment of meteoritic siderophiles over indigenous values. Furthermore, from the elemental ratios, it is possible in many cases to determine what type of projectile may have struck (e.g., *Palme*, 1980). Clearly, these methods require a detailed knowledge of the siderophile element content in the initial target rocks, and it has not been successfully applied to all lunar impact melts because there is uncertainty about the initial siderophile concentrations in the lunar rocks (e.g., *Anders*, 1978; *Wänke et al.*, 1978; *Ringwood*, 1978).

On Earth, this geochemical approach was applied by *Alvarez et al.* (1980) to interpret their discovery of a siderophile-rich layer at the Cretaceous-Tertiary boundary (65 m.y. ago) as the result of a giant impact that seemingly triggered a major mass extinction in the "recent" geologic record of Earth.

Studies of terrestrial impact melt sheets, some several hundred meters thick (e.g., Manicouagan Crater, Canada; *Floran et al.*, 1978), indicate that compositional and textural arguments can be combined to distinguish successfully between impact melts and internally-derived igneous rocks. For a few lunar samples, however, these arguments can become interpretative and are not settled (e.g., *Anders*, 1978; *Ryder et al.*, 1980).

By studying divers lunar impact melts in detail, a variety of major questions related to the evolution and composition of the lunar crust were successfully resolved, as detailed in section 6.4. Many others still remain open. For example: What are the original pristine igneous rocks composing the initial lunar crust that gave rise to the observed, "mixed" impact melts? What was the stratigraphic and selenographic distribution of these pristine rocks? Do grossly similar impact melt compositions, as revealed by cluster analysis, imply a common parent crater for a number of melt specimens, or do they result from a number of separate impacts into grossly similar targets? Many of these questions can only be answered by further field work to provide the necessary structural and stratigraphic control.

Unfortunately for resolving these problems, most information on terrestrial impact melts derives from melt sheets inside the crater cavity, where they typically pool in the bottoms of simple craters or form an annulus between the central uplift and topographic rim of large complex craters (see Fig. 4.12). Few terrestrial impact melts have been recovered as ejecta outside the crater rim; the well-preserved and relatively young Ries Crater of Germany is one example where this has been done (*Pohl et al.*, 1977). No terrestrial analog for the melt pools mapped in the rim vicinity of lunar craters (e.g., *Hawke and Head*, 1977) is known on Earth. Are the

impact melt ejecta identical both inside and outside the crater rim? The make-up of the unmelted ejecta no doubt differs vastly between those regions.

Furthermore, the concept of close compositional homogeneity of impact melts is demonstrably violated by terrestrial tektite melts (*tektites* are small bodies of heterogeneous silicate glass generally believed to have formed in terrestrial impact craters). While the exact origin of tektites is poorly known (*Engelhardt et al.*, 1987), they undoubtedly formed during the early cratering stages as high-velocity ejecta. But major chemical differences exist between the tektites or the tektite-like impact melts found around and undoubtedly related to several terrestrial craters [the Ries Crater (moldavites; *Engelhardt et al.*, 1987), Lonar Crater (lonarites; *Murali et al.*, 1987) and Zhamanshin impact structure (irghizites; *Florensky*, 1975)] and the much larger volumes of impact melt found inside the craters.

4.1.3. Crater Frequency and Bombardment History

The statistical study of lunar crater populations provides several kinds of critical data. The distribution of crater diameters reflects the mass distribution of incoming projectiles, and the number of craters in a given area tells us how many objects struck. This information gives fundamental insights into the collisional dynamics of the solar system, because it defines both the mass frequency and time-integrated flux of impacting objects. Crater statistics are also indispensable to understanding lunar surface evolution because of one simple fact: Older surfaces accumulate more impact craters than young ones. The number of craters observed in any region therefore defines important chronological information because it can tell us the relative ages and times of emplacement of different geological formations. If we can then determine the absolute emplacement ages of these formations (e.g., by age-dating of samples), then we can calculate absolute crater production rates and absolute projectile fluxes. Such measurements have indeed been accomplished for the Moon as one of the greatest successes of the Apollo program, and from them we have learned a great deal about collisional processes in the inner solar system and about lunar geologic evolution during the past 4 b.y.

Crater frequencies. The relative frequencies of lunar crater diameters are illustrated in Fig. 4.13. In these plots, ΣN , which is defined as the number of craters equal to or larger than a given diameter D in a unit area, is plotted against d , which is measured in meters. The three panels cover three different diameter intervals: 10^{-5} mm to 1 mm (a), 1 cm to 1 km (b), and 100 m to 1000 km (c).

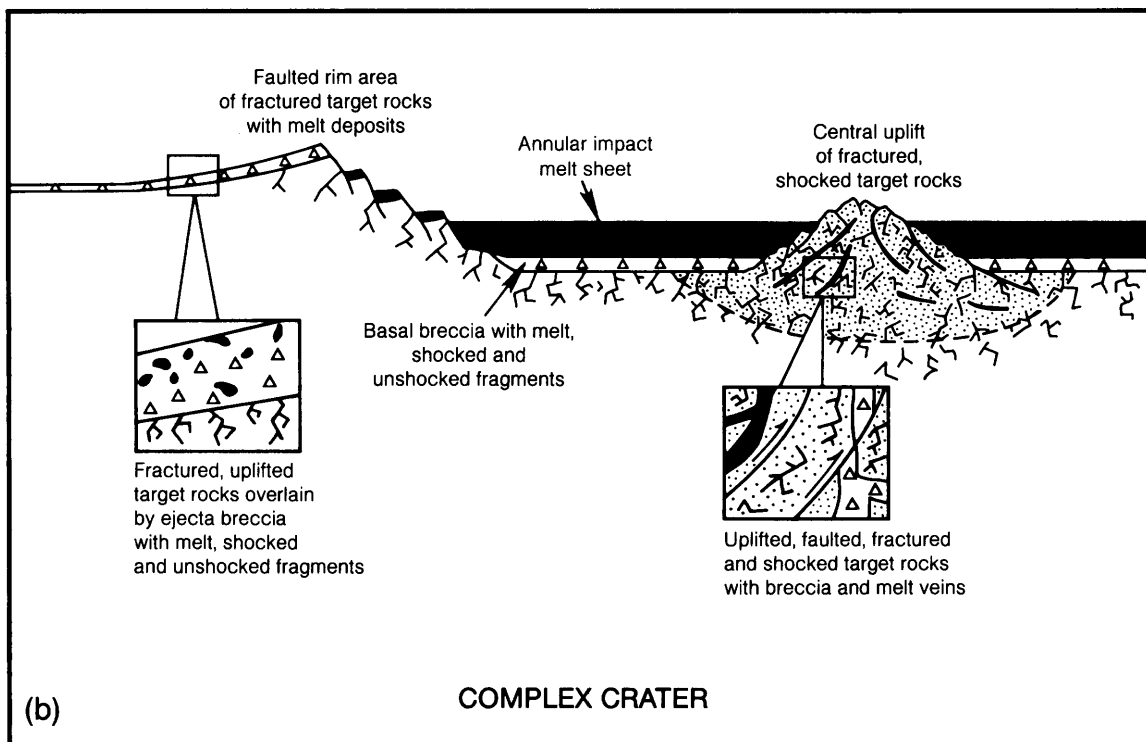
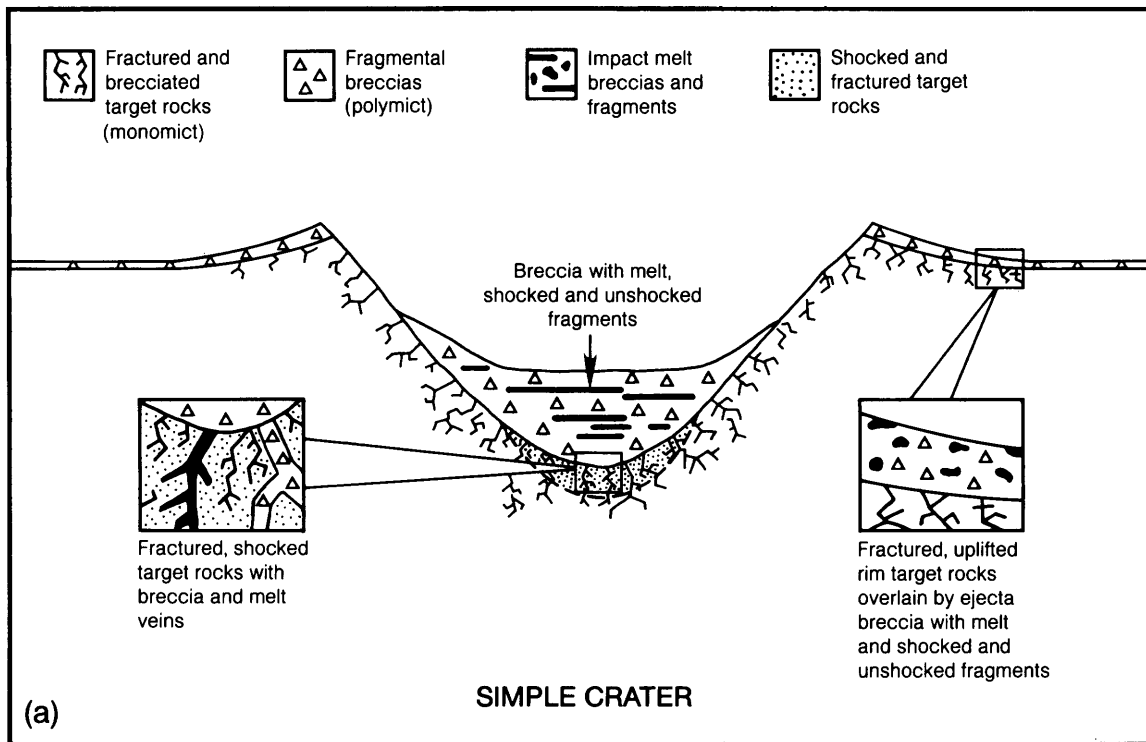


Fig. 4.12. Schematic cross-sections of simple and complex impact craters indicating the spatial distribution of impact-produced rock types; for emphasis and clarity, cross-sections are not to exact scale. **(a)** Simple craters are characterized by an interior, fragmental *breccia lens* containing both unshocked and shocked materials, including impact melt. This breccia lens overlies the highly fractured and shocked crater floor. The floor may have been slightly displaced as a result of the impact, but it still preserves the original structural and stratigraphic relations of the target. Veins of impact melt or fine-grained breccias may be injected into this crater floor along impact-induced fractures. The uplifted rim is composed of (1) highly fractured target rocks that have been slightly displaced and (2) ejecta from the crater. The ejecta are fragmental, but the deposits preserve an inverted stratigraphy, and increasing amounts of shocked and melted materials occur toward the top. **(b)** The interior of a complex crater is characterized by a fragment-containing, massive, impact-melt sheet that surrounds the central peak as an annulus. Breccias, which contain fragments derived from a number of sites within the crater (*polymict breccias*), occur at the base of the melt-sheet and overlie highly fractured, moderately shocked, bedrock. Fracturing and deformation of this bedrock may continue to depths (d) approaching substantial fractions of the crater diameter (D) (i.e., $d = 0.1$ to $0.2 D$). The central uplift exposes originally deep-seated, highly disturbed shocked rocks, cut by breccias whose fragments tend to be of a single rock type (*monomict breccias*). The rim area is structurally displaced, terraced, and pervasively fractured. The underlying bedrock of the terrace is covered by ballistic ejecta; most of the latter are highly polymict and moderately shocked. Bodies of ejected melt tend to pool in surface depressions on top of the breccias. Impact melts, together with both polymict and monomict breccias, may also be injected into fractures in the crater basement, as well as into the central uplift. Some of these veins may even have been generated in place during rapid subsurface movements of large blocks. Such rapid movements can produce intense fracturing along the block margins and can generate sufficient frictional heating to produce local melting.

These three different diameter ranges are studied by different observational techniques; they also reflect real differences between major geologic units and processes. Microcraters (panel a) largely control the evolution of particulates in the lunar soil, the erosion of surface rocks, and the exposure history of individual soil components to the space environment. Intermediate-size craters (panel b) are largely responsible for the comminution of near-surface bedrock and the build-up of the lunar regolith (see Chapter 7). Finally, the “large” lunar craters and multiring basins (panel c) have profoundly affected lunar crustal evolution, have dominated global morphology and stratigraphy, and were particularly important during early lunar history.

The <1-mm data (panel a) are based on optical and electron microscope observations of returned lunar rock surfaces; smooth glassy surfaces make particularly good microcrater detectors, as illustrated by the glass-coated surface of rock 64455 (Fig. 4.13d). At this size range, measured crater diameters may be used to calculate projectile masses with a fair degree of confidence because high-fidelity impact simulations and calibrations can be performed on the same scale in the laboratory (e.g., Gault, 1973; Vedder and Mandeville, 1974). Because the surface-exposure ages of many of these cratered rocks are also known, thus giving the integrated time that the rock has been at the surface (e.g., Arvidson et al., 1975a), the flux of micrometeoroids may be calculated as well.

Within experimental error, this calculated lunar micrometeoroid flux is consistent with totally independent measurements by contemporary space-

craft, as recently summarized by Grün et al. (1985). Figure 4.14 represents current best estimates for the flux of small particles; the data reflect spacecraft measurements, augmented at the large mass end ($>10^{-3}$ g) by a variety of astronomical observations (see Grün et al., 1985). This particle population has apparently interacted with the lunar surface for aeons. It also defines the major collisional hazard to humans and machines, a major concern for large-scale and long-term lunar surface operations (see section 3.10).

Panels b and c in Fig. 4.13 represent crater studies made using photogeologic methods. The craters shown in panel b are largely confined to young basaltic mare surfaces, those in panel c to ancient highland terrains; crater counts for structures >200 km in diameter refer to the entire Moon. The data in panel b are characterized by substantial uncertainties, with a possible gap at the smallest crater sizes. These deficiencies result partly from the fact that the imaging systems employed in lunar orbit have limited spatial resolution, and thus fail to detect smaller craters. However, the effect is largely due to natural causes. The lunar surface is not a simple and easily interpreted projectile detector for craters <100 m in diameter because it is not possible to distinguish with confidence between small primary impact craters and the numerous craters formed by secondary impacts from larger craters.

An additional problem with craters <100 m in diameter is that the lunar surface does not permanently record all the small primary impact craters that form on it. In most regions of the Moon, so many 100-m craters have formed over geologic time

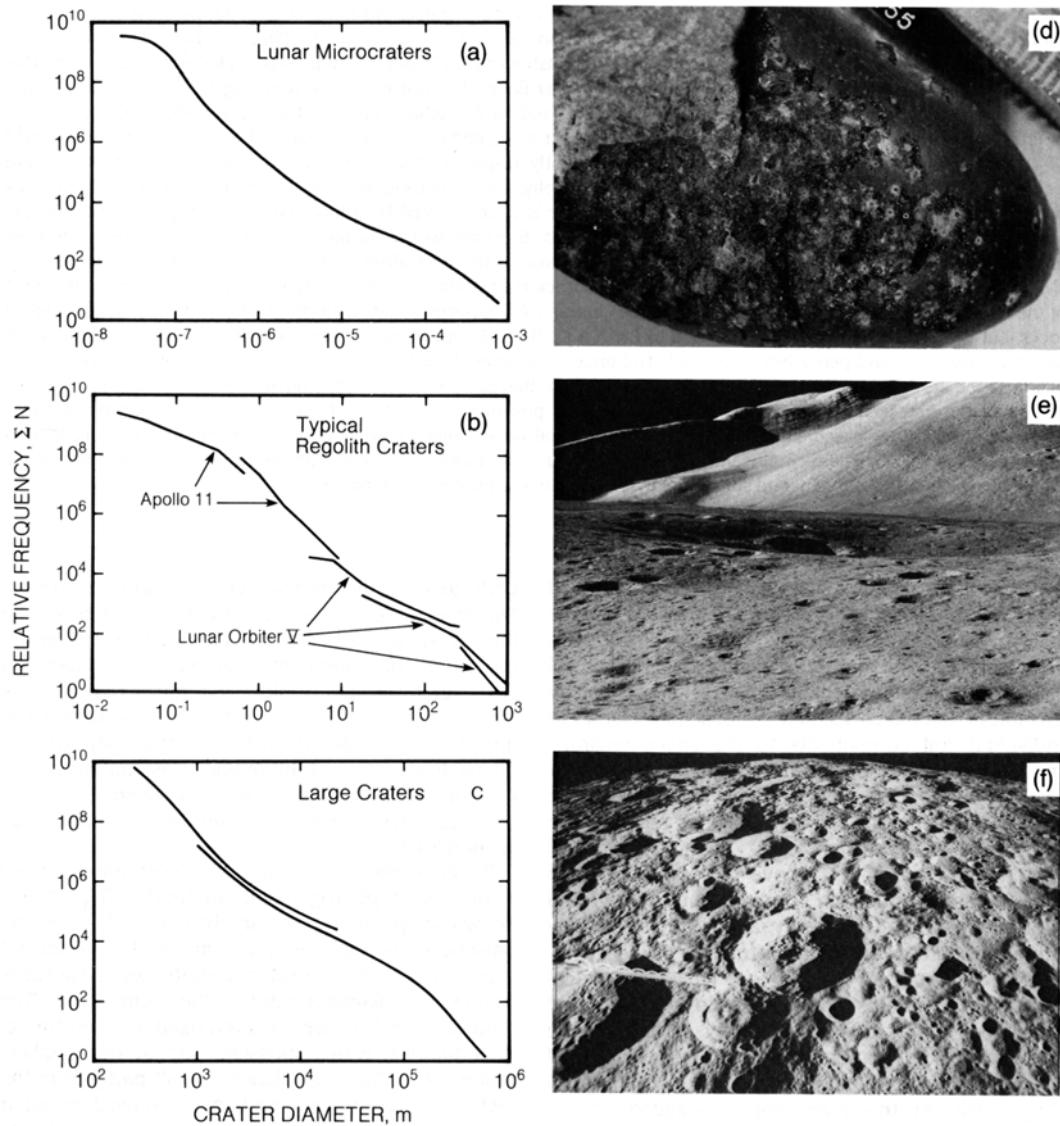


Fig. 4.13. The cumulative size-frequency distributions of lunar impact craters ranging from submicrometer-size features to structures 1000 km across. Horizontal axes show crater diameters (in meters). Vertical axes show cumulative number of craters equal to or larger than a given diameter per unit area, or ΣN . **(a)** Lunar microcraters, **(b)** typical regolith craters, and **(c)** large impact structures (see text for details). Also shown are representative lunar scenes that illustrate the dominant geological effects of these crater-size regimes: **(d)** lunar rock 64455, a sample draped with impact-produced glass, in which small craters have been produced; this sample illustrates the erosive capabilities of the micrometeorite environment (NASA Photo S-73-22656); **(e)** typical lunar surface scene from Apollo 15 showing numerous craters in the 1–10-m diameter range; such craters are responsible for much of the regolith gardening and evolution (NASA Photo AS15-87-1148); **(f)** heavily-cratered lunar highlands displaying large numbers of craters >10 km in diameter (NASA Photo AS16-M-0594). A large body of information (collected by various groups) is synthesized in this figure. For summaries see (for **(a)**) Morrison and Clanton (1979); Hartung et al. (1978); (for **(b)**) Shoemaker (1970); Soderblom (1970); Neukum (1977); and (for **(c)**) Neukum et al. (1975); Wilhelms (1985); BVSP (1981).

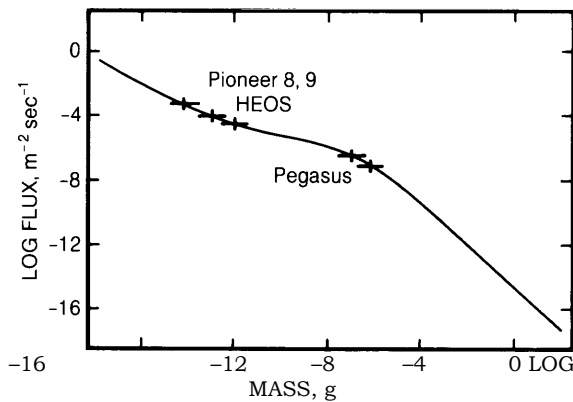


Fig. 4.14. The flux of micrometeoroids ($\sim 10^{-17}$ to 10^2 g in mass) at 1 A.U., as estimated from lunar rock analyses, direct *in situ* measurements by various spacecraft (Pioneer, HEOS, and Pegasus), and divers Earth-based observations (after McDonnell, 1977; Grün *et al.*, 1985).

that a “steady state” has been reached where each freshly created crater destroys a preexisting one. The lunar surface has thus been “saturated” with small craters (Gault, 1970) and only the “survivors” can be observed, which may be a small fraction of all the craters formed. On the Moon, the younger mare basalt surfaces, 2–3 b.y. old, yield excellent statistics for craters approximately 0.5–10 km in diameter (Neukum *et al.*, 1975). Unfortunately, most mare surfaces are too young to have recorded large numbers of craters >10 km diameter.

These problems of saturation and differential obliteration also affect the interpretation of the “large” structures shown in panel c. In the geologically older lunar highlands, so many craters >10 km in diameter have formed that the crater populations may be saturated at this level, causing relatively “small” craters (<10 km in diameter) to be underrepresented. Additional complexities stem from the different views of individual workers as to what constitutes the actual crater diameter, especially in large multiring basins, and on individual and somewhat subjective identifications of highly degraded craters. In addition, secondary craters from large basins may be as large as a few tens of kilometers across (Wilhelms *et al.*, 1978) and may therefore affect the crater frequencies shown in panel C at the small size end.

Crater densities and projectile flux. Since the lunar surface records impact history in a cumulative, time-integrated fashion, measurement of the absolute spatial crater density (N/km^2 , where N is the cumulative number of craters with diameters greater than a specified size) constitutes a measure of relative exposure age. Absolute and relative crater

densities have therefore become valuable tools for lunar stratigraphy, a discipline that attempts to establish the chronologic sequence(s) of geologic events (section 4.4).

Relative age-dating of different craters can also be obtained from quantitative measurements of their degradational states. Impact is the most active erosional process on the Moon, and the relative degradation of different craters, measured in various ways, is therefore a measure of the cumulative exposure time to the meteorite flux (e.g., Soderblom, 1970; Soderblom and Lebofsky, 1972; Boyce, 1976; BVSP, 1981).

The return of actual basalt samples from several different lunar maria made it possible to use radioactive age-dating methods to determine the crystallization ages of specific basalt flows and therefore their time of eruption and solidification. Measured basalt eruption ages range from 3.1 to 3.9 b.y. (Wasserburg and Papanastassiou, 1971; see also section 6.1). The absolute crater densities for craters >4 km in diameter obtained from these dated flows are illustrated in Fig. 4.15. Other lunar data in Fig. 4.15 are model-dependent to some degree, but are still valuable in understanding crater production rates through geologic time.

Most rocks returned from the older lunar highlands have narrowly restricted ages between 3.8 and 4.0 b.y. and are for the most part only slightly older than the oldest basaltic mare surfaces. Highland regions, however, typically display 10 to 50 times as many large impact craters (>15 km) than do the volcanic flows of the maria. The conclusion is therefore inescapable that there was a markedly higher crater-production rate between 3.8 and 4.0 b.y. ago than over the last 3.8 b.y. Some workers interpret this difference as the tail end of the original planetary accretionary process and use the data to calculate half-lives for the depletion of the initial inventory of impacting planetesimals (e.g., Hartmann, 1975; Neukum and Wise, 1976; Wetherill, 1981; Baldwin, 1981). Others propose that a cataclysmic increase of infalling projectiles occurred at approximately 3.8–4.0 b.y. ago (Tera *et al.*, 1974).

Samples of lunar impact melts collected from nonvolcanic surfaces are clearly the materials needed to obtain formation ages of individual craters (e.g., Grieve, 1982). For this reason, the relatively narrow age distribution of these samples, from about 3.8–4.0 b.y., is surprising. The simplest interpretations of this observation entail a high projectile flux between 3.8 and 4.0 b.y. ago, yet significant differences exist in the details of different mechanisms. Much current debate focuses on whether impact melts from large basin-forming events are present in the sample collection and, if so, how many (e.g.,

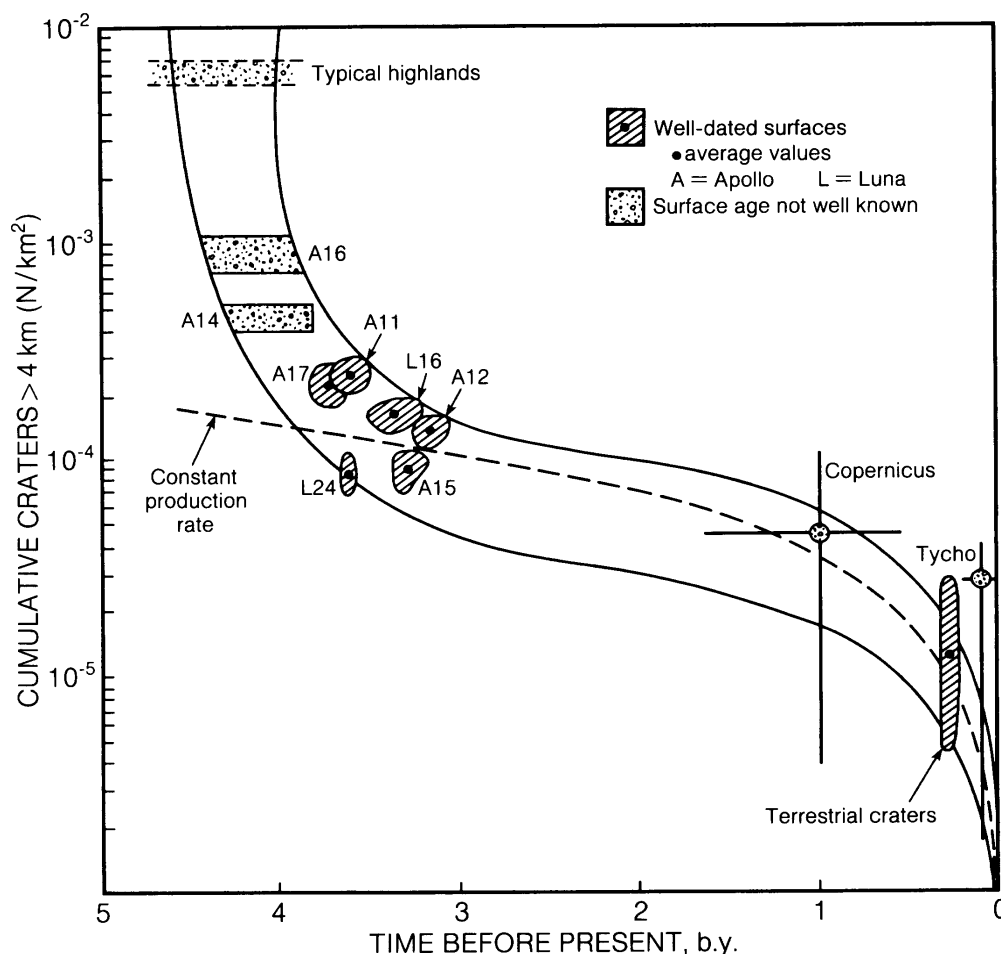


Fig. 4.15. Lunar crater production rates through geologic time, as reconstructed from the measurement of crater densities on the lunar surface and from absolute age dating of returned lunar rocks. As indicated in the text, firm correlations may be reconstructed only for (1) the well-characterized basalt surfaces (3.8–3.2 b.y. old) and (2) the contemporary meteorite flux, based on current astronomical observations ($t = 0$). The terrestrial cratering rate applies to only the last 200 m.y. and the ages for lunar craters Tycho and Copernicus are inferred from indirect evidence. Cratering activity was clearly very high prior to 3.8 b.y., as indicated by the lunar highland rocks, but details of this bombardment history cannot yet be reconstructed. The absolute production rates refer only to craters >4 km in diameter (and are expressed as number formed per km²). Note that the inferred crater production rate differs markedly from the curve representing a constant crater production rate around 4 b.y. ago (based on BVSP, 1981).

James, 1981; Wilhelms, 1985). If the sample collection were dominated by impact melts from a few basins, the ages measured would represent chiefly the times of basin formation, regardless of other crater-forming events. In the Apollo sample collections, the oldest basin represented would likely be Nectaris (from Apollo 16), variously interpreted to have formed at 3.8 b.y. (James, 1981; Spudis, 1984) to ~3.9 b.y. ago (e.g., Wetherill, 1981). A large number

of basins are younger than Nectaris (Wilhelms, 1984), including Serenitatis and Imbrium, impact melts of which are possibly present in the Apollo 17 and Apollo 15/14 sample collections, respectively.

All interpretations involving the presence of numerous samples of basin-related impact melts in the collection and the associated formation ages of 3.8–4.0 b.y. require that several gigantic, basin-forming impactors collided with the Moon up to

approximately 3.8 b.y. ago. Other workers, however, point out that a very large fraction of all smaller, non-basin-forming impacts occurred after formation of the Nectaris Basin and they attribute most melt samples and their formation ages to these subsequent non-basin-forming impacts. In summary, the true production rate for large lunar highland craters is not well known, and the flux implied by Fig. 4.15 for periods older than 3.8 b.y. remains speculative. While we are confident that intense bombardment occurred in early lunar history, absolute cratering rates remain uncertain.

The age of <1 b.y. estimated for the relatively young craters Copernicus and Tycho (Fig. 4.15) is based on circumstantial evidence and is uncertain. This young age is, however, in accord with independent estimates of the terrestrial cratering record for the past 200 m.y. (Grieve, 1982) and with present-day astronomical observations of solar system objects that cross the Earth/Moon space to become potential projectiles (Shoemaker, 1983).

The question of the apparent exponential increase in projectile fluxes in early lunar history is intimately related to the equally fundamental question of how many large impact craters and multiring basins were formed at all on the Moon (e.g., Baldwin, 1974, 1981; Strom, 1977; Neukum, 1977; Hartmann, 1980; Wetherill, 1981; and many others). Does the observable crater population faithfully reflect all the large craters that formed (Strom, 1977; Neukum, 1977), or does it merely reflect the survivors? The fact that many craters are partly to nearly obliterated is taken by some workers to suggest that large numbers of "early" craters were indeed destroyed (Hartmann, 1980) and that current crater populations reflect the surface saturation conditions described by Gault (1970).

The nature of the returned highland samples has been used in attempts to resolve this problem. Ryder (1981) has estimated that the Apollo collection contains 30% (by volume) of impact melt. If this figure is indeed representative of all highlands, then the existence of multiple cratering is strongly indicated, because single (terrestrial) impacts never seem to produce more than 10% impact melt in their ejecta (Grieve *et al.*, 1977). In addition, Lange and Ahrens (1979) have emphasized that the observed age distribution of lunar highland impact melts is incompatible with models involving simple exponential decays of the impactor populations that are required to produce the observed crater population. Most workers therefore agree that the highlands have been saturated for craters <4 km in diameter and that the current crater populations merely represent the survivors, rather than all impact structures formed.

4.1.4. Geological Processes

As indicated in section 4.1.2, meteorite impact is a major transport process, because it redistributes materials both laterally and vertically, either by sedimentation from ballistic trajectories or by upward subsurface motion. Impact is also a major erosional process. Depending on the size of the event, impacts can pulverize surface boulders, shatter subsurface bedrock, or even dislodge crustal sections tens of kilometers deep. Impact is also the most important metamorphic process on the Moon, causing characteristic shock deformation, heating, melting, vaporization, and even ionization of pre-existing minerals and rocks. Impact processes alter the textures of rocks and generate new ones, such as glasses, impact melts, and fragmental rocks (*breccias*) containing either a single rock type (*monomict*) or multiple rock types (*polymict*). A detailed classification of impact-generated rock types and their nomenclature is presented in Table 6.11 in Chapter 6 (see also Stöffler *et al.*, 1980).

The ejection of material from impact structures, and the subsurface effects beneath them, combine to produce a lunar crust and surface composed of lithologically diverse impact deposits. Some ejecta deposits from individual young impact basins are distinctive enough to be mapped as discrete geological formations and stratigraphic units; they have distinct surface characteristics and well-defined structural/temporal relations to neighboring units (e.g., Wilhelms and McCauley, 1971; see geological map, Plate 10.10). Despite their apparent uniformity, these lunar ejecta units must be highly complex. Even within the relatively small ejecta deposits surrounding terrestrial craters, there is exceptional textural and structural complexity, diversity of grain size, and variability in rock types (Hörz *et al.*, 1983). The complexity and internal variability of large-scale lunar ejecta deposits must be larger still, partly because many individual components have been repeatedly processed by impact cratering. For example, it is typical for lunar impact breccia samples to contain fragments of impact melts and older breccias from a number of craters. Textural, mineralogical, chemical, and chronological evidence for these "breccia within breccia" relationships is common (e.g., Quick *et al.*, 1981 a,b).

Multiple cratering on the lunar surface is a random process in space and, to some extent, in time. Therefore, a variety of statistical (probabilistic) models have been used to explore the effects of continuous meteorite bombardment, and especially of multiple impacts on the lunar surface. Figure 4.16 illustrates some first-order results by plotting the relative times necessary to cover specified fractions

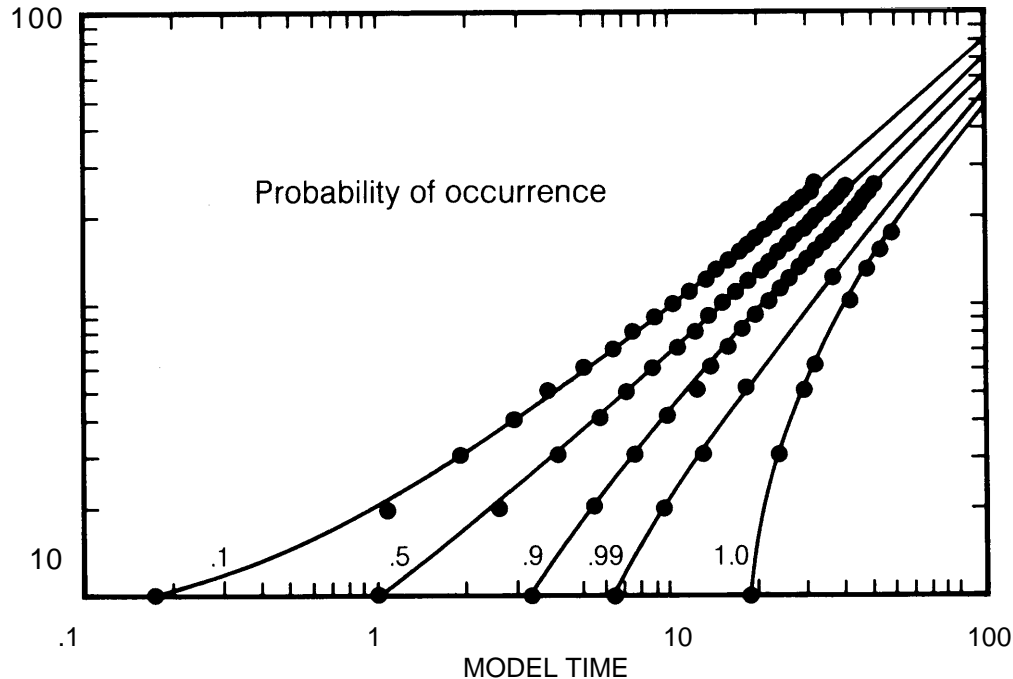


Fig. 4.16. Statistical results, using a probabilistic Monte Carlo technique, which illustrate how often a given area of the lunar surface may be impacted. The analysis uses an arbitrary model time that is linearly related to the number of impacts generated by computer. The smallest surface element considered is equivalent to the surface area of the smallest impact crater employed in the calculation. Unit time is defined as the interval that is long enough to provide a probability of 0.5 for impact to occur in any surface element; a period of time about 7 times longer is needed to increase this probability to 0.99 (i.e., 99% of the surface is cratered). At the end of this time 90% (probability 0.9) of the surface has been impacted twice, 50% has been impacted at least five times, and 10% has suffered approximately eight impacts. By the time the last surface element is cratered for the first time (with probability 1.0), >90% of the entire surface has already suffered more than 10 impacts.

of the lunar surface with craters. In this model, craters were represented by simple circles simulating measured crater-diameter size frequencies; they were allowed to form at random surface coordinates and times. "Unit" time is defined as the period necessary for any given point to be impacted at least once with a probability of 0.5; this time corresponds, by definition, to the time necessary to crater 50% of any given model surface. Note that it takes approximately 20 times longer to crater every surface point at least once (probability 1.0) (Fig. 4.16). While this is being accomplished, many surface points will simply suffer repeated impacts; 90% of the given surface will have received about 10 impacts and 10% will have been cratered 20 times. This example demonstrates that any fractional element within a large surface area may have experienced a substantially different impact history when compared with the "average" of the entire exposed surface.

Lunar rock erosion. Small impacts by particles less than one micrometer to several centimeters in diameter will erode lunar rocks by two principal mechanisms. Very small impacts have an "abrasive" effect, akin to energetic sandblasting, and each impact removes a relatively small amount of rock. In contrast, more energetic events, involving larger projectiles up to centimeters in size, will completely shatter an entire rock by "collisional fragmentation" (Gault and Wedekind, 1969; Matsui *et al.*, 1982). Examples of these erosive processes are illustrated in Fig. 4.17. These processes are clearly gradational and partial disruption of surface boulders has been commonly observed.

"Abrasive" impacts may be thought of as impacts into infinite half-space targets, with a large mass ratio of target rock/projectile. With larger projectiles, and smaller rock/projectile ratios, the target rock acts as a finite-sized object and shatters if the

impact energy exceeds a definite value. The erosion rate by abrasion has been calculated to be on the order of 1 mm/ 10^6 years for typical kilogram-sized lunar rocks (Ashworth, 1977). Larger, more massive rocks have higher erosion rates, because increasingly larger impacts begin to contribute to the abrasive process. Absolute abrasion rates, therefore, increase with increasing mass of the target rock.

The survival times of lunar surface rocks for collisional fragmentation by large impacts are much shorter than for abrasion (Fig. 4.18). The experiments of Gault and Wedekind (1969), Gault (1973), Fujiwara *et al.* (1977), Matsui *et al.* (1982), and others have shown that collisional fragmentation destroys rocks faster and more effectively than abrasion.

These calculated abrasion rates and collisional lifetimes for lunar rocks compare favorably with the observed size population of lunar rocks (Hörz, 1977; Langevin and Arnold, 1977). A typical surface rock of 1 kg mass can be expected to survive on the Moon for approximately 10 m.y. Observed rocks, including many Apollo samples, have therefore resided on the lunar surface for periods comparable to the time it took the Colorado River to carve out the Grand Canyon (about 15 m.y.). Terrestrial erosion processes are orders of magnitude more efficient at wearing down exposed rock surfaces.

The “gardening” of the regolith. Small meteorite impacts, involving submillimeter-sized projectiles, dominate the small-scale evolution of the lunar surface. Such repetitive and frequent impacts agitate the lunar surface by shattering, burying, exhuming, tumbling, and transporting individual grains in a random fashion. These processes gradually develop a fine-grained powdery layer on the lunar surface above the actual bedrock. This layer, called the *regolith*, is then continuously “gardened” and churned (Morris, 1978a). The actual “gardening” process has been investigated through detailed lunar soil studies described in Chapter 7.

A number of models have been developed to describe the rate and depth of this gardening process (Shoemaker, 1970; Gault *et al.*, 1974; Langevin and Arnold, 1977). Two typical results are illustrated in Fig. 4.19. Owing to the steep mass-frequency distribution of the micrometeoroid population (i.e., smaller projectiles are much more abundant than larger ones), the rate of gardening or “turn-over” decreases rapidly with depth. In 10^6 years, the regolith is gardened (overturned) once to a depth of almost 1 cm at the 50% probability level, but during the same period the uppermost millimeter is turned over a few tens of times and the outermost 0.1 mm a few hundred times (Fig. 4.19a).

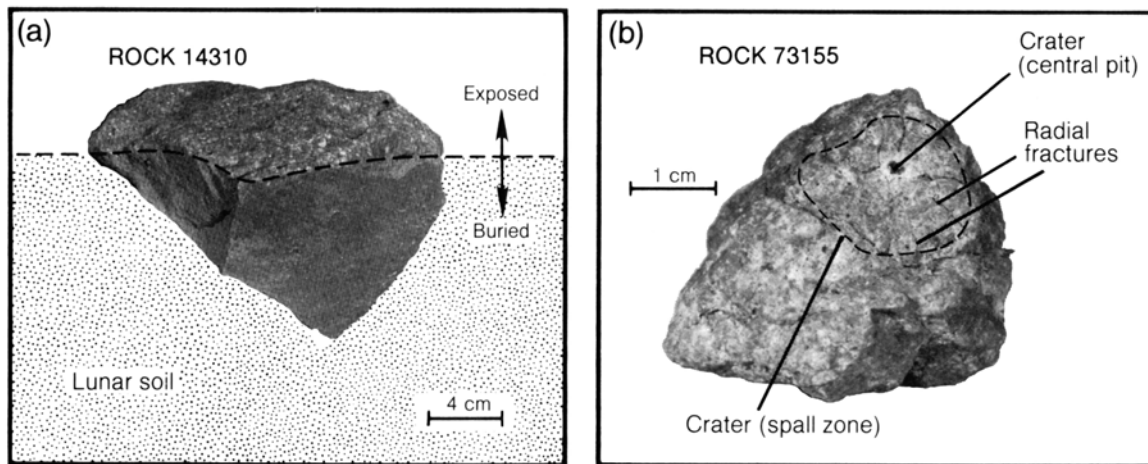
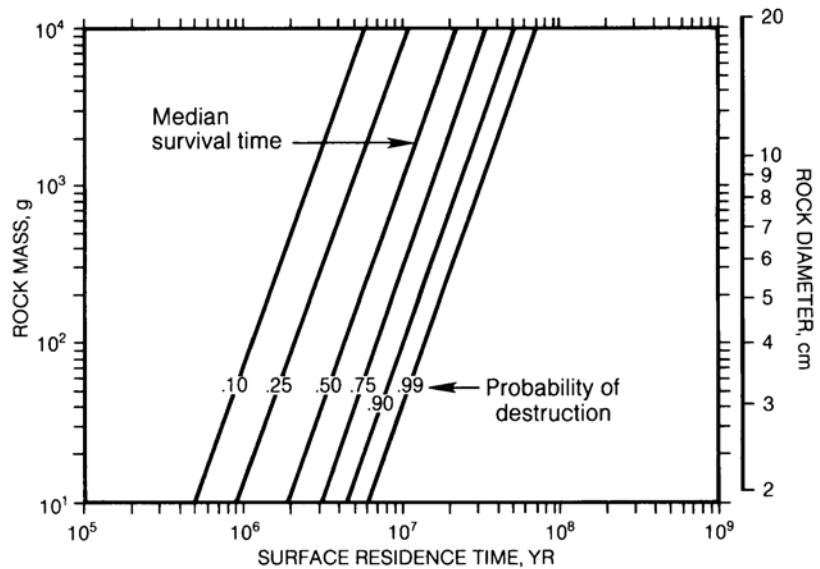


Fig. 4.17. Erosional processes recorded by lunar surface rocks. **(a)** Abrasion by multiple, small-scale impacts, akin to energetic sandblasting. The upper rock surfaces, rounded and smooth, were exposed to space and thus to micrometeoroid impacts; they contrast strongly with the lower, angular, fresh fracture surfaces that were buried in the soil. Such rocks with simple exposure histories are rare in the Apollo collection; most lunar rocks have tumbled on the surface a number of times. As a result, they display microcraters and other signs of space erosion on all surfaces (NASA Photo S-71-21830). **(b)** A rare example of a more energetic impact that almost broke up an exposed lunar rock. The large impact crater is characterized by (1) a central, glass-lined depression (central pit, commonly termed “pit-crater”), around which occur (2) a prominent “spall zone,” characterized by mass loss and removal of surface material by tensile failure, and (3) prominent, penetrative fractures that emanate radially from the impact. A slightly more energetic event would have largely destroyed the entire rock (NASA Photo S-73-17057).

Fig. 4.18. Possible surface residence times of lunar rocks before they are destroyed by collisional breakup caused by energetic impacts. This model combines probabilistic modeling with experimentally determined threshold energies that are necessary to destroy a given rock mass (after Hörz *et al.*, 1975).



In developing the regolith, a major role is played by the rare larger impacts (Fig. 4.19b). Such impacts can create a layered regolith column, despite the tendency of more numerous smaller impacts to homogenize the upper part of the regolith. The model illustrated in Fig. 4.19b emphasizes the role of larger craters and illustrates how a typical layered regolith column may be produced. Random impacts are allowed to remove materials from a surface point initially at "0" elevation by excavation and negative elevation change or to deposit materials onto the same point by ballistic sedimentation (positive elevation change). Over time, constructive and destructive impact events are continually competing; in this hypothetical regolith, a particularly destructive event occurred at 240 m.y., destroying all previous sedimentary history.

Because of these infrequent but large-scale events that destroy the preexisting record, stratigraphic gaps (*unconformities*) must therefore be common in lunar regolith profiles. Profiles in core samples collected only meters apart may reveal very different depositional histories, and unique interpretations of the profiles in core samples, some a few meters deep, is possible only in rare cases (see Chapter 7). Despite these diversities in depositional histories and surface exposures between individual grains or individual soil samples, there are not necessarily any great differences in the mineralogy, rock types, or chemical composition. Most regoliths are largely derived from underlying local bedrock, and they show a relatively limited compositional variety at any given Apollo site (Papike *et al.*, 1982).

Large-scale regolith evolution. The projectiles responsible for pulverizing rock and for macroscopic regolith evolution are largely in the 10- to 1000-cm diameter range. The effects of such impacts can be modeled by Monte Carlo statistical simulations, such as those of *Quaide and Oberbeck* (1975; Fig. 4.20). Figure 4.20a shows how the median regolith thickness evolves as a function of absolute number of impact events. Crater populations on the younger mare surfaces do not exceed $N = 10^8/\text{km}^2$ (diameter, $D > 1$ m) and regolith thicknesses are typically only a few meters. Regolith thicknesses >10 m, however, may occur in the highlands. Figure 4.20b addresses the macroscopic evolution of regoliths at the Apollo 11 and 12 sites, for which both the crater populations and the regolith thicknesses are well understood.

These figures also compare the effects of time-constant vs. exponentially decaying meteorite fluxes for the Apollo 11 and 12 sites. The important point is that, for either type of flux, the overall growth rates of the regolith decrease with time. This is caused by the gradual development of the regolith itself, which acts to shield the bedrock. As time goes on, and the regolith thickens, increasing numbers of "small" craters develop entirely in the regolith layer and fail to penetrate bedrock. It takes increasingly larger craters, which are relatively rare, to deepen the regolith by penetrating the entire layer and excavating new bedrock. Therefore, today's regolith growth rates are significantly lower than those in early lunar history, when the regoliths were thinner and the overall impact flux was higher.

Because all Apollo rock samples are loose pieces in the regolith, there is substantial interest in estimating the source depths from which individual bedrock fragments have been derived. Figure 4.20c illustrates the progressive change of mean source depths in an evolving mare regolith, while Fig. 4.20d portrays fractional regolith volumes derived from specific depths. Such models can place constraints on the nature and stratigraphy of the local bedrock beneath the regolith, using the data obtained by analyzing the surface soils.

The many crater cavities that penetrate the regolith combine to produce a highly irregular surface at the bedrock/regolith interface, although

much of the relief is subsequently filled and smoothed by mass wasting and ejecta deposition (Soderblom, 1970; Shoemaker, 1970; Boyce, 1976). As a result of these processes, regolith thickness can be highly variable locally. Figure 4.21 illustrates the distribution of regolith depths calculated from Monte Carlo methods and compares them with depths inferred from photogeologic measurements for specific lunar surface areas. In these measurements regolith depths are determined from the presence of distinct "benches" within small craters. These benches form because of the contrast in physical strength between the relatively competent bedrock and the overlying unconsolidated, fragmental rego-

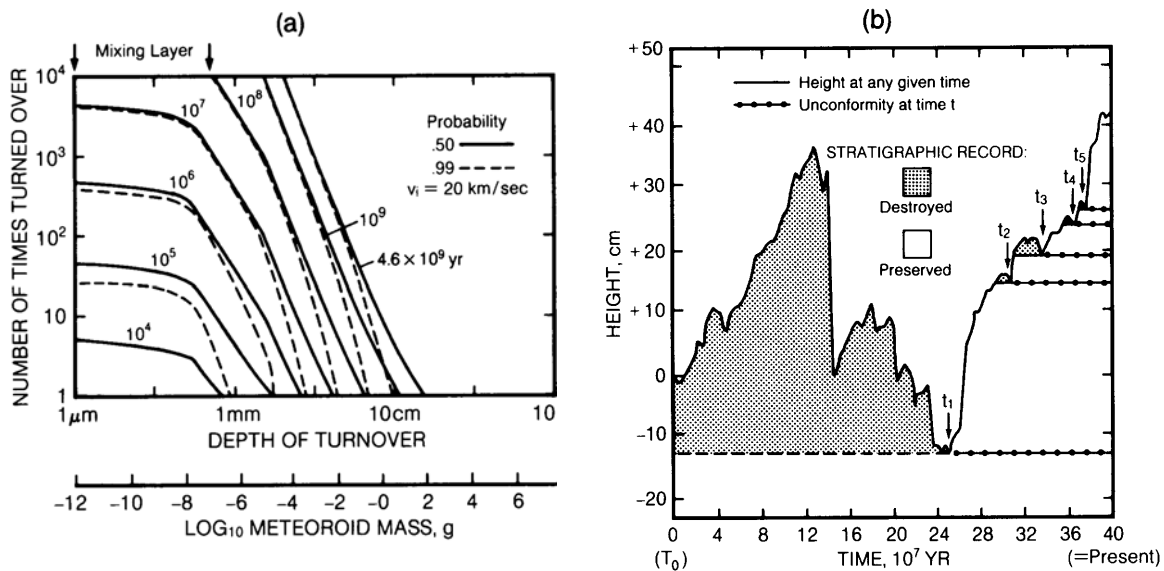


Fig. 4.19. Gardening of the near-surface regolith. **(a)** This figure combines probabilistic calculations with laboratory cratering experiments in fine-grained unconsolidated targets. These data are used to convert projectile kinetic energy into realistic estimates of crater volumes, diameters, and depths. The figure shows the number of times a given area of lunar surface is affected by cratering and the excavation and overturning depths involved for a specific time interval (indicated by a number adjacent to the curves), for both 0.50 and 0.99 levels of probability. This complex figure is best read along a vertical line corresponding to a fixed depth below the surface. Intersections of this line with the curves indicate varying time durations, and the number of overturns during that period can be read from the vertical axis. It is clear that near-surface zones (a few millimeters or less) of the regolith are highly active (e.g., 10–100 turnovers in a million years). However, the turnover rate decreases very rapidly with depth; zones deeper than 10 cm have little probability of being turned over during the entire lifetime of the Moon at *present* cratering rates (after Gault *et al.*, 1974). **(b)** Results of probabilistic calculations that model successive deposition or erosion of fine-grained regolith material at an arbitrary point on the lunar surface. This model incorporates both crater excavation (negative relief changes) and the addition of crater ejecta (positive relief changes). The time axis gives absolute time duration (i.e., it begins at the left side of the graph, at T_0). The vertical axis indicates the elevation change of the regolith surface relative to a starting point of 0 elevation at T_0 . The graph thus depicts the historical evolution of a regolith profile. In this model, substantial buildup of the regolith occurred early, but a large impact at $12\text{--}16 \times 10^7$ yr destroyed almost the entire deposit. Additional buildup and modest destruction then continued, but at 24×10^7 yr, all previous regolith history (to a depth of 12 cm) was destroyed by an even larger impact. Continuous buildup dominates after that and is only slightly affected by minor mass removal. Considering the absolute scales involved, it appears obvious that highly diverse and complex regolith histories will be encountered over small distances, i.e., on the scale of Apollo landing sites and between the locations of cores collected on a single mission (after Langevin and Arnold, 1977).

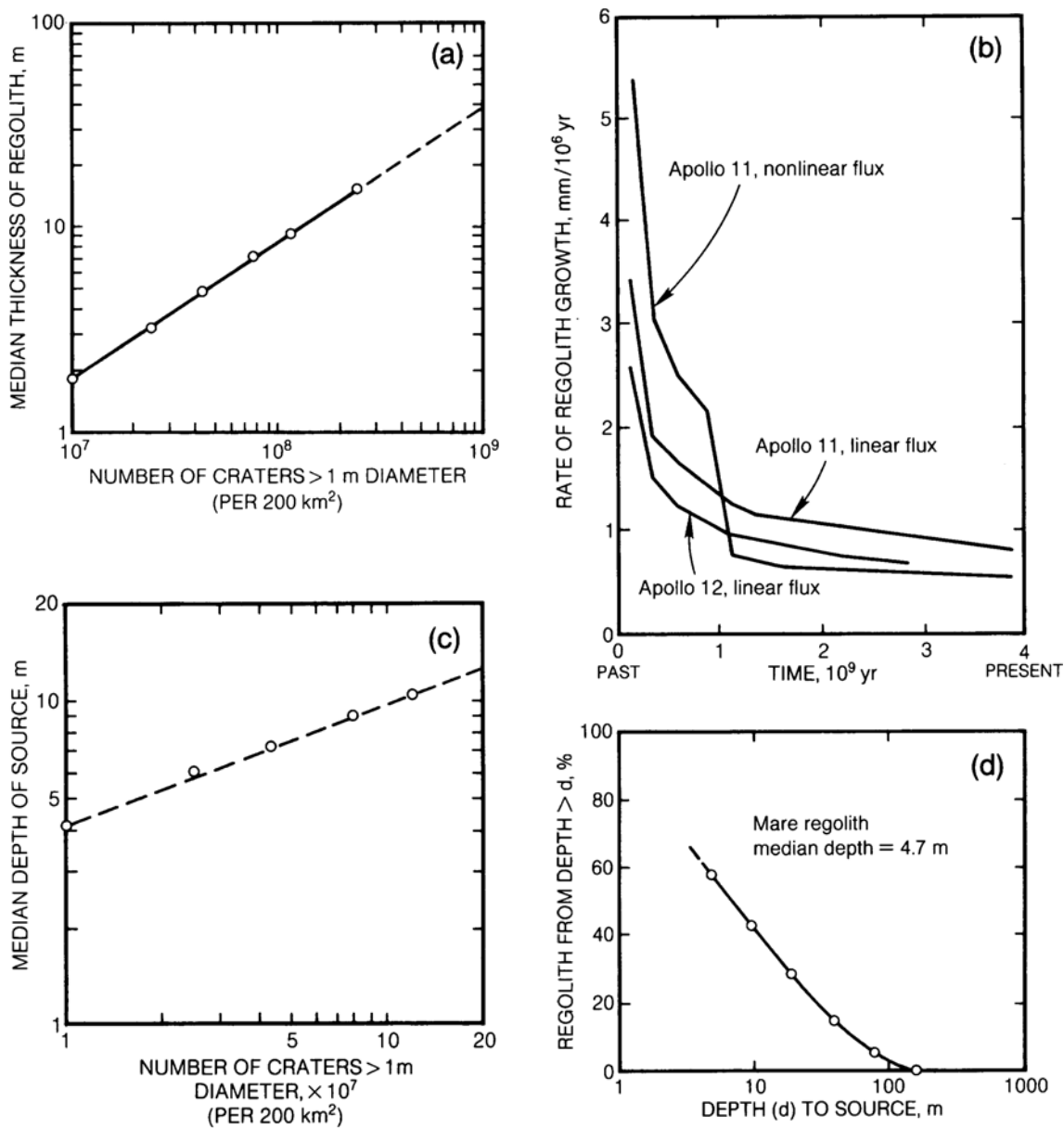


Fig. 4.20. Some aspects of large-scale lunar regolith evolution, using models that combine probabilistic calculations, impact experiments, and photogeologic analyses of lunar mare surfaces. **(a)** How the median regolith thickness increases as a function of absolute number of craters on the surface. The regolith thickness is not linearly proportional to the number of craters because, as time goes on, increasingly larger (and less frequent) craters are needed to penetrate the regolith and to produce fresh bedrock ejecta. **(b)** The rate of regolith growth at the Apollo 11 and 12 landing sites, allowing for differences in crater density and assuming linear and nonlinear impact flux models. The regolith originally developed at >3–5 mm/m.y., but typical contemporary regolith growth rates have dropped to <1 mm/m.y. **(c)** Calculated median source depth for fragments located in an evolving regolith. Note that median source depths for most mare regoliths are a few meters; such regoliths are dominated by the comminution of local bedrock. **(d)** Cumulative mass fractions derived from sources deeper than a few meters for a regolith typical of Apollo 12, having a median depth of 4.7 m. Virtually no fragments are derived from >100-m depth (all figures after *Quaide and Oberbeck, 1975*).

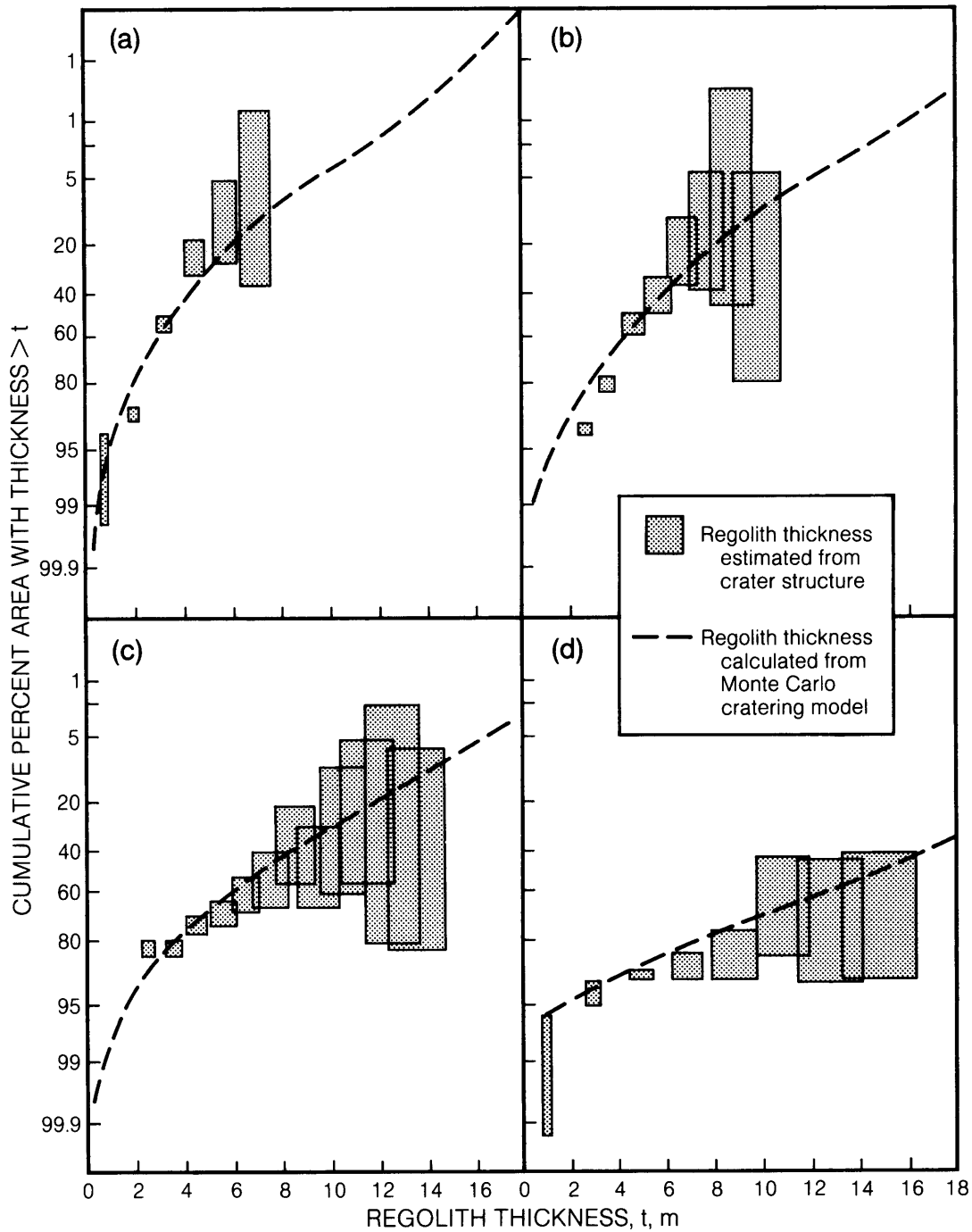


Fig. 4.21. Thickness variations of the lunar regolith obtained by photogeologic studies of four representative lunar surface areas, compared with thickness distributions obtained from Monte Carlo calculations. [(a) Apollo 12; (b) Apollo 11; (c) densely cratered mare; (d) Apollo 16 (after Oberbeck and Quaide, 1968).] The close agreement between calculated and observed results provides strong support for the general models of regolith formation by random meteorite impacts.

lith (Oberbeck and Quaide, 1968). The close agreement between observed and calculated regolith depths supports the Monte Carlo calculations of Quaide and Oberbeck (1975).

Large-scale bombardment of the highlands. The epoch of intense bombardment that occurred in early lunar history is not readily modeled. Many essential parameters have little or no experimental or observational constraints, and major assumptions must be made. The most crucial uncertainties involve estimates of the absolute numbers of large impact craters produced (as discussed in section 4.1.3). There are also serious uncertainties about the shapes and sizes of the transient crater cavities and the volumes of material excavated from them. As a result, current models are highly divergent.

Short and Foreman (1972) were the first to suggest that the aggregate volume of ejecta from all major lunar craters, evenly spread over the entire Moon, must be at least 2.5 km deep. Similar results were obtained by Monte Carlo modeling by Hörz *et al.* (1977) and Aggarwal and Oberbeck (1979), and by analytical approaches (Hartmann, 1980). Calculations by Cashore and Woronow (1985) produced estimates of much deeper ejecta stacks, possibly tens of kilometers in thickness. Regardless of these differences, there is little doubt that cumulative ejecta thicknesses on the lunar highlands must be measured in kilometers. Hörz *et al.* (1977) and Hartmann (1980) calculate thicknesses approaching 10 km using model bombardment histories about 10 times more intense than that indicated by the present crater populations.

These calculations refer to ballistic ejecta only. They do not consider the substantial subsurface mass movements typical of large-scale impacts. In these events, the lunar crust must be disturbed to great depths, as illustrated in Fig. 4.22. In a terrestrial analog, Pohl *et al.* (1977) have shown that the bedrock beneath a young, 26-km-diameter crater (Ries Crater, Germany) is seismically disturbed to depths of 4.5 km, although its excavation cavity is estimated to be only 1.5 km deep. By analogy, the lunar crust may well be fractured and brecciated to depths approaching 10 km, judging from the sizes of preserved craters, and significant fracturing, cataclasis, and brecciation may be present at average depths approaching 20 km. Still greater depths of disturbance may have been developed over large areas of the Moon if substantial numbers of large, multiring basins once covered the entire Moon, but have since been obliterated.

Because of these uncertainties, the average depth to which the lunar crust is mechanically disturbed is not known. Conservative estimates conclude that

ejecta blankets are at least 2–3 km thick (mega-regolith) and that structural disturbance (fracturing, brecciation, etc.) is over 10 km deep in the highland areas. These are average values; data for specific regions may be substantially different. As illustrated in Fig. 4.22, these estimates appear consistent with seismic profiling and measured sound-velocities (V_p).

Available data are not sufficient to test these estimates. Seismic measurements can, in principle, distinguish between solid and fragmented rock, but many fragmented and displaced masses may have been recompacted and densified by subsequent impacts. The occasional occurrence of recrystallized lunar rocks (*granulites*) in the Apollo samples (see section 6.4.6) may imply that recrystallization at elevated temperatures has occurred at depth within the Moon. Even highly-fragmented ejecta from large craters may recrystallize if heated sufficiently. These compaction and recrystallization effects can blur the ideally sharp contact between impact-transported melt or breccia and underlying fractured bedrock. Actual seismic measurements do not reveal a pronounced discontinuity in the lunar highlands akin to the sharp regolith/bedrock interfaces detected on the younger mare basalt surfaces (see Chapter 7). The limited seismic profiling of the lunar crust reveals a gradual velocity increase with depth, which may be consistent with the presence of disturbed rock masses as deep as a few tens of kilometers (Fig. 4.22).

Lateral mass transport. Most current models for impact craters spread the ejecta centrosymmetrically around the crater, typically within <2.5 crater diameters from the center. These models are based on photogeologic studies of the “continuous” deposits around lunar craters (Moore *et al.*, 1974; see Fig. 4.5). Unfortunately, the ejection velocities for the more distant “discontinuous” ejecta are not sufficiently known to be meaningfully incorporated into these models. This omission is a significant flaw in these models, for the discontinuous deposits clearly consist of high-speed ejecta, and the amount of such material ultimately determines the transport efficiency of the impact event at large distances from the crater (Pieters, 1986). Distant ejecta is also geologically significant, because it may distribute “exotic” components across the Moon (or even farther away; see discussion of “lunar meteorites” in Chapter 2). At the global scale, our views on the homogeneity or heterogeneity of the present lunar crust also depend on the efficiency of lateral mass transport. Considerable quantities of ejecta from large multiring basins may be distributed globally, and these continuous deposits can cover and conceal substantial surface areas (Moore *et al.*, 1974; Davis and Spudis, 1985). All remote-sensing informa-

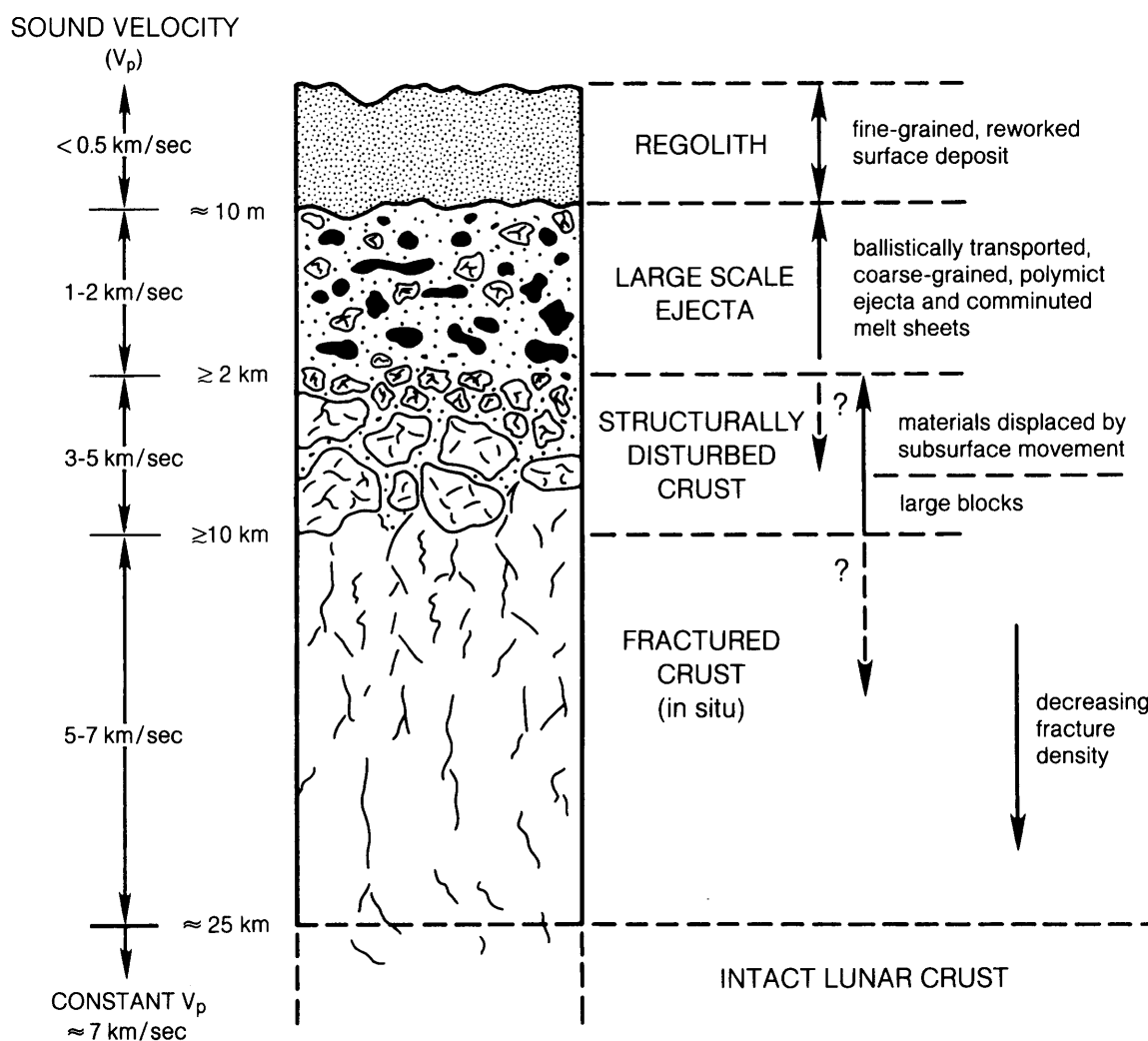


Fig. 4.22. Highly schematic cross-section illustrating the idealized effects of large-scale cratering on the structure of the upper lunar crust; see discussion of megaregolith in the text. A structurally disturbed lunar crust is also inferred from seismic measurements, e.g., from sound velocity (V_p) (Toksöz *et al.*, 1973). The depth scale in the figure is highly uncertain, because the total number of large craters and basins remains unknown. Highly variable depth effects must exist in different regions, depending on the degree to which an area has been affected by basin-sized impacts.

tion (optical imagery, infrared spectra, chemical data) is obtained from the surface layer and can therefore refer only to the last swath of ejecta deposited over any given province.

Arvidson *et al.* (1976) calculated the mass fraction of regolith material at any specific sampling site that is derived from specific craters at given radial ranges (Fig. 4.23). The results suggest that regolith is largely locally derived, with only about 1% of the ejecta derived from distances >10 km from the sampling

site. The models of Quaide and Oberbeck (1975) yield similar results. Petrologic-geochemical studies (e.g., Rhodes, 1977) also indicate that the bulk of the regolith at any site is derived from fairly local sources. In general, substantial (>10%) amounts of "exotic" materials from distant terrains are not observed in most lunar soils (Hörz, 1978). Nevertheless, because of the potential importance of such components, considerable effort has been spent in petrographic and geochemical searches for exotic

components from distant and lithologically different terrains (e.g., *Basu and Bhattacharya*, 1986; see Chapter 7).

At regional and global scales, the lunar surface is both chemically and lithologically heterogeneous, a conclusion supported by the diversity of the Apollo sample suite, by compositional remote sensing from lunar orbit, and by Earth-based telescopic methods (see Chapter 10). Major outstanding questions are whether and to what degree this observed surface heterogeneity reflects the existence and preservation of an initially heterogeneous lunar crust beneath the surface. In other words, we do not know whether the observed lunar surface patterns are only a superficial reflection of the last large-scale ejecta deposits, or whether they are in fact related to properties of the deeper lunar crust (*Warren and Taylor*, 1981; *Davis and Spudis*, 1985).

Basin-related ejecta deposits are clearly massive enough to conceal substantial fractions of the underlying original lunar surface. A better understanding of ejection processes from large craters and multiring basins is necessary to determine whether the current surface distribution of the diverse lunar rock types reflects their initial distribution, or if the observed provinces are the simple result of large-area ejecta deposition. In evaluating this mechanism, it is important to remember that the crater ejecta are confined to within <2.5 diameters of the parent crater, even around multiring basins. The currently recognized basins cover only a small portion of the Moon; if those are all the basins ever formed, it

seems likely that only a modest redistribution of crustal rocks has occurred; if so, then the observed differences arise from the heterogeneous nature of the lunar crust.

Although many unanswered questions remain, it is possible to identify the next steps that must be taken to solve them. Concerted laboratory efforts are needed to understand impact and ejection processes in more detail, with emphasis on the high-speed ejecta components. Better observational constraints are also needed for the lunar surface itself. Improved remote geochemical sensing at high spatial resolution would provide precise and high-resolution compositional gradients across highland/mare boundaries or across the contacts between chemically contrasting lava flows. Exact measurements of the compositional gradients across such chemically contrasting contacts would greatly help to establish the time-averaged fraction of surface components that derives from known distances and the extent of transport of "exotic" materials into local regions.

4.2. BASALTIC VOLCANISM

The presence of volcanic activity and lavas on the surface of a planet reflects the planet's thermal state and its evolution. Unless the planet somehow generates high enough internal temperatures to melt rocks, volcanic activity may never begin or, having begun, may not last long. On the Earth, melts form in the mantle, the deep layer that underlies the Earth's outer crust; the necessary heat is provided by the decay of natural radioactive elements. A complex method for melting rocks in the Earth's mantle is by the movement of large crustal plates that drag down (*subduct*) crustal rocks to lower depths where they can melt. Subduction does not occur on the Moon, where all lunar volcanism apparently resulted by melting of mantle rocks mixed with little or no recycled crust.

Although we have well-documented samples from only two terrestrial planets, the Earth and the Moon, there is indirect evidence that the lavas produced by partial melting of the mantles of all the terrestrial planets are chemically similar (*BVSP*, 1981). This situation reflects the fact that the mantle compositions are also similar, because all of the terrestrial planets were probably assembled from similar materials when the solar system formed.

When mantle materials are heated, melts are generated from those minerals that melt most easily at mantle pressures. These are *partial melts*, and they do not have the same composition as the original mantle material from which they form. The most common partial melts produced are called *basalts*. They are characterized by relatively low SiO_2

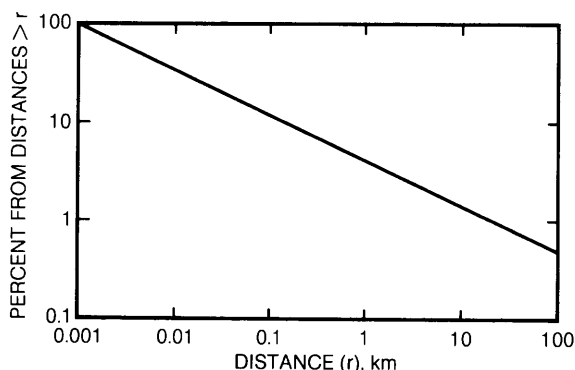


Fig. 4.23. Graph showing analytical model results for the cumulative mass fraction of the regolith at a given location that has been brought to the site as ballistic ejecta from varying distances. Virtually all ($>95\%$) of the regolith material is locally derived (from <5 km); only $<1\%$ apparently comes from sources > 10 km distant (after *Arvidson et al.*, 1975b).

contents (45–55%) and by relatively high MgO and FeO contents. None of them resemble the higher-SiO₂ lavas produced on Earth by the deep reprocessing of crustal rocks.

Because such melting has apparently occurred on all the terrestrial planets—and is still occurring on Earth—many scientists are now studying complex mantle processes such as partial melting, the pooling of melt (*magma*) into deep *magma chambers*, and the ascent of magma to the surface.

For the necessary melting and basaltic volcanism to occur on the Moon, temperatures of >1100°C at depths of 150–200 km are required. The mere existence of basaltic lavas at the lunar surface therefore provides important data about past temperatures within the Moon.

The duration of lunar volcanic activity is related to the thermal state of the mantle and thus to the thermal evolution of the Moon. Current data indicate that major lunar volcanic activity ceased at approximately 3 b.y. ago, implying that mantle temperatures had then dropped below those necessary to sustain partial melting.

Studies of lunar basalts are important for determining the composition of the Moon's mantle. Because they are “partial” melts, the lunar basalts are chemically complementary to the residual unmelted mantle materials left behind. Using the thermodynamic principles involved in equilibrium partial melting, the complementary residue may be characterized and the original bulk composition of the Moon's mantle may then be calculated.

All of the smooth, dark regions visible on the Moon's nearside consist of lavas that partly or completely fill the multiring basins (Figs. 4.24 and 4.25). Basaltic lavas cover an area of 7×10^6 km², 17% of the Moon's surface (Head, 1976). Nearly all of the basalts occur on the nearside.

Most of the facts concerning lunar basaltic volcanism are derived from the analysis of returned samples (section 6.1) and from the characterization of volcanic landforms (section 4.2.1). The sequence and duration of volcanic activity, as exemplified by successive filling of multiring impact basins, is described in section 4.2.2, and estimates of the total volume of basaltic lavas generated are summarized in section 4.2.3. The possibility that there was early volcanic activity on the Moon is discussed in section 4.4.

Not all products of basaltic volcanism are necessarily lava flows. “Fire fountaining,” driven by gases exsolving from the magma, occurs during basaltic lava eruptions, dispersing the melt as fine droplets. These droplets form *pyroclasts* or *volcanic ash* that may be strewn over large areas. Pyroclastic materials are recognized in the lunar sample collection and

can also be identified by remote-sensing techniques, especially by infrared reflectance spectra that reveal their glass-rich nature (Adams *et al.*, 1974; Hawke *et al.*, 1979). Pyroclastic deposits on the Moon are widely dispersed and are readily worked into the regolith by impact gardening; identification of these deposits in surface photographs is possible only at a few well-preserved locations.

4.2.1. Volcanic Landforms

Mare lava flows. The dark-colored flat mare plains were formed by large-volume eruptions of low-viscosity basaltic lavas (BSVP, 1981; see section 6.1). Samples of lava and volcanic ash returned to Earth confirmed the commonly held hypothesis of a volcanic origin for the mare plains (Baldwin, 1948, 1963). Several other hypotheses for the flat basin fills had been put forth, including pyroclastic flows (Mackin, 1964) and deep dust, mass-wasted from the highlands (Gold, 1966). Much earlier, Galileo had likened these smooth surfaces to water, i.e., “oceans,” thus the Latin term “mare.” In current usage, *mare basin* designates a circular, multiring impact structure and *maria* the dark-colored lavas within such basins.

Although lunar lava flows were identified through pre-Apollo telescopic observations and on Lunar Orbiter imagery, the best descriptions of these landforms are based upon maps and panoramic photography generated during the extended Apollo J missions (Apollo 15–17; Schaber, 1973a). Figure 4.26 shows in detail several lava flows of Mare Imbrium, but qualitatively similar observations also apply to other mare basins. In the Imbrium Basin, lavas were erupted from the southwest basin edge (18° to 23°N, 28° to 32°W; Fig. 4.26). From this center, three successive sets of flows extend into the basin for 1200 km, 600 km, and 400 km, respectively, over slopes of about 1:1000 (Fig. 4.26b). Lobate flow scarps bounding these flows have heights ranging from 10 m to 63 m and average ~35 m (Gifford and El Baz, 1978). These combined flows cover an area of $\sim 2 \times 10^5$ km² (an area equal to that of Nebraska or Senegal), with an estimated basalt volume of 4×10^4 km³. The presence of leveed flow channels and localized lava ponds (dammed by wrinkle ridges; see below) on these lava flows provide strong support for the concept of extraordinarily large flow distances over essentially flat terrain.

Such thin flows, 20–40 m thick, would be expected to chill and solidify quickly; the apparently long flow distances are therefore surprising. This apparent inconsistency was in part solved by direct viscosity measurements of molten lunar basalt (Weill *et al.*, 1971). The viscosities are unusually low, only a few tens of poise at 1200°C. Furthermore, similar

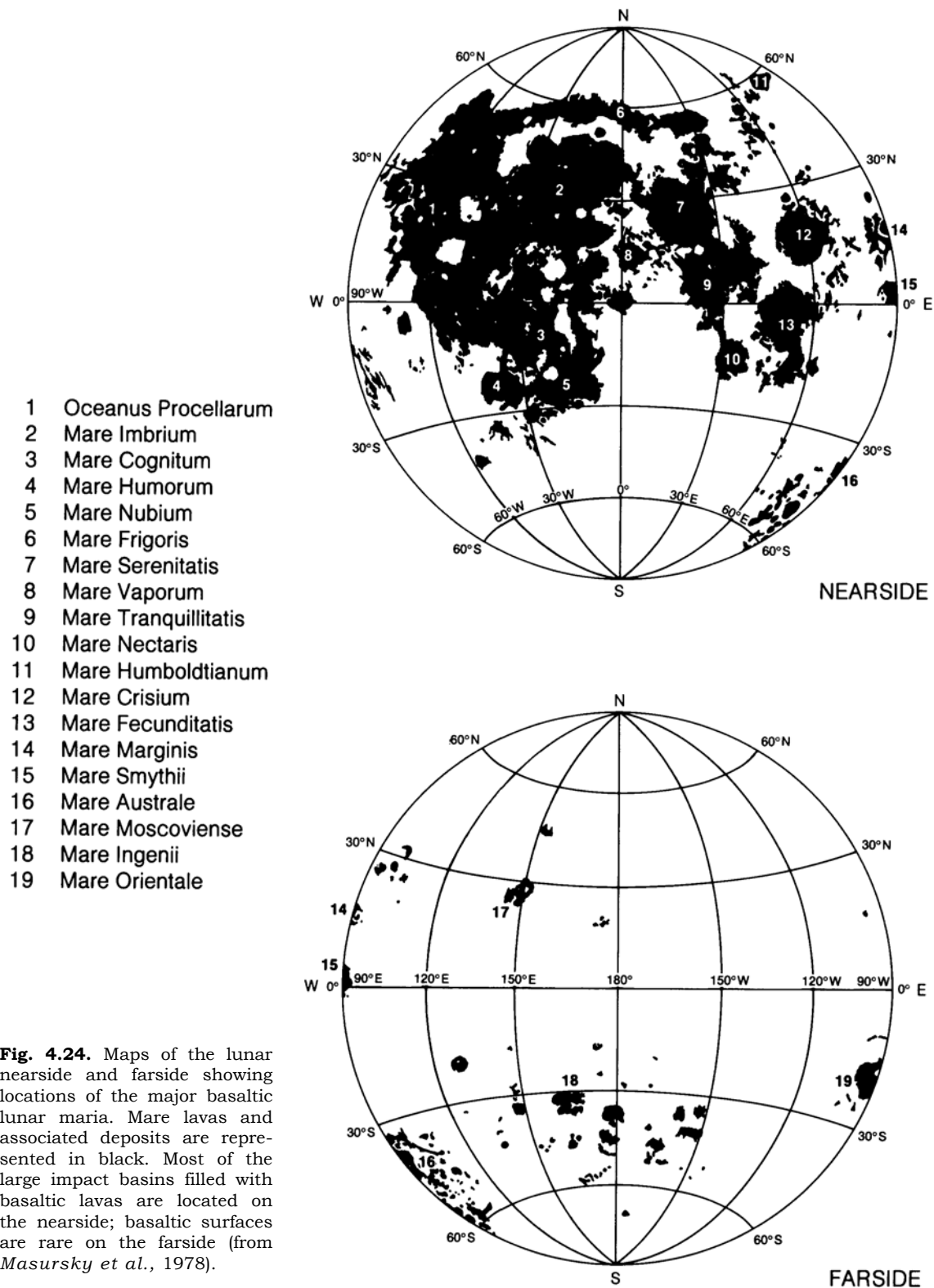


Fig. 4.24. Maps of the lunar nearside and farside showing locations of the major basaltic lunar maria. Mare lavas and associated deposits are represented in black. Most of the large impact basins filled with basaltic lavas are located on the nearside; basaltic surfaces are rare on the farside (from Masursky *et al.*, 1978).

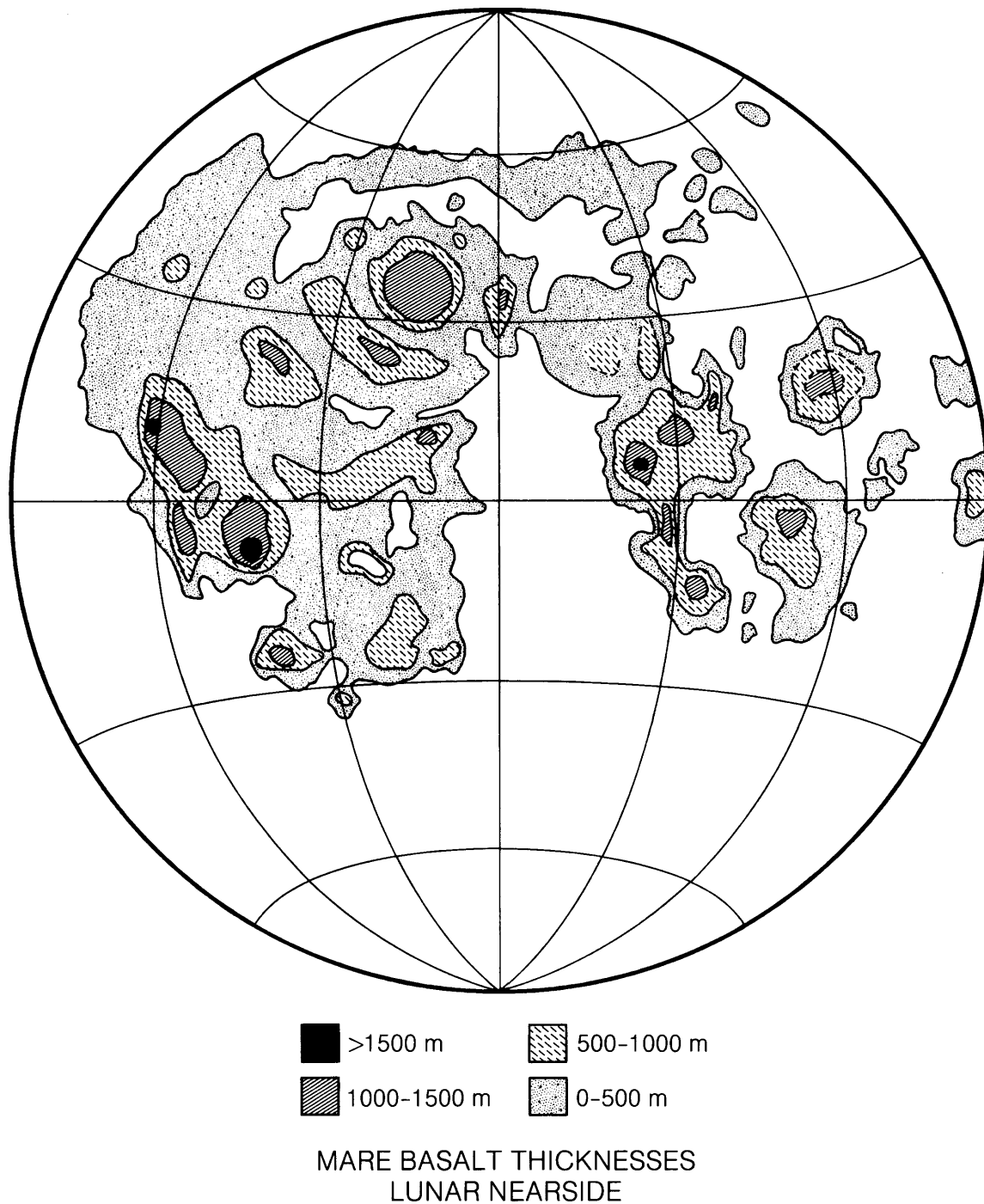
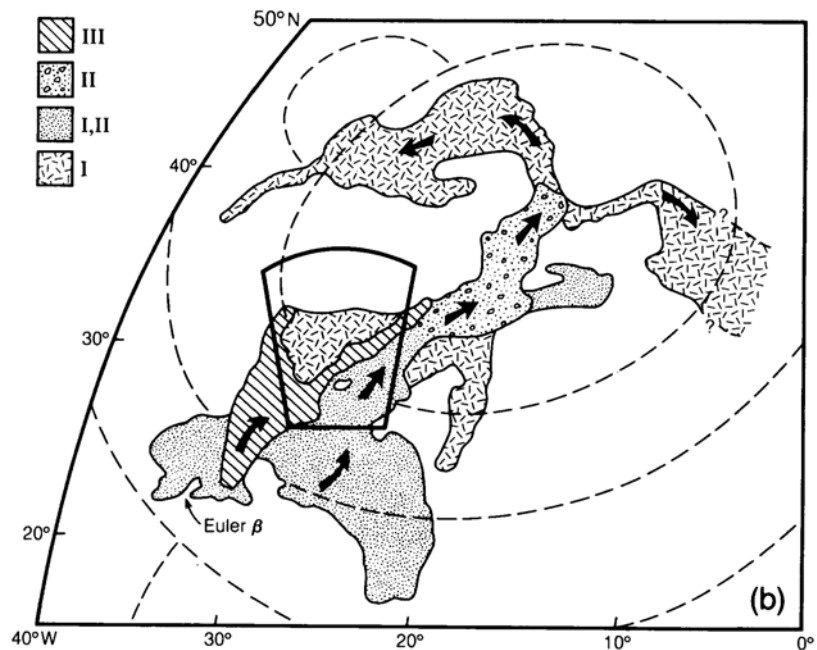


Fig. 4.25. Estimated thickness of mare basalts in the nearside maria based on the “flooded crater” method of DeHon (1974, 1979) and DeHon and Waskom (1976). Isopach interval is 500 m. Note the substantial basalt depths in the basin centers, where no flooded craters are seen because they have been totally inundated by basalt flows. Most flooded craters occur in the relatively shallow shelf areas.



Fig. 4.26. Sequence of eruption of large-scale lava flows in Mare Imbrium, a 1200-km-diameter impact basin. **(a)** Oblique, northwest-facing photograph of Mare Imbrium, illustrating lobate flows-carps, leveed channels (running southwest to northeast), and con-centric wrinkle ridges. Mount La Hire (center-right), about 30 km long at the base, is surrounded and partially submerged by lavas. Lavas are channeled between La Hire and part of a massif to the northwest (NASA Photo ASI5-1556). **(b)** Location and extent of the major basalt flows of Mare Imbrium according to *Schaber* (1973a). Crater counts reveal three major episodes (I, II, III) of basalt extrusion, spanning approximately 0.5 b.y. The sources for these flows are believed to be fissure vents located in the southwest rim of Mare Imbrium. Arrows indicate direction of flow; dashed lines are basin ring structures. "I, II" are areas where lava flows from episodes I and II overlap and cannot be individually mapped. The heavy outline shows the area of **(a)**.



eruption processes on Earth have formed the flood basalts of the Columbia River Plateau, Washington State, and have been reconstructed through studies by *Shaw and Swanson* (1970). At high eruption temperatures ($\sim 1250^\circ\text{C}$), low viscosities (<30 p), and high eruption rates, the Columbia River basalts are believed to have erupted 10^{-1} to 10^{-2} km³/day of lava for each kilometer of active fissure. For comparison, the youngest of the Imbrium lava flows was erupted from a 20-km-long fissure located at the intersection of major basin rings. By analogy with the Columbia River basalt flows, 0.1 to 2.0 km³ of lava per 24-hour period could have erupted from this Imbrium fissure, assuring the high eruption rates required for lava to flow to great distances.

The thin lava flows studied in the Imbrium Basin are not unique. By applying petrologic models to basalt samples from the Apollo 11, 12, and 15 sites, *Brett* (1975a) determined that those samples had come from lava flows less than 10 m thick. In the walls of Hadley Rille, at the Apollo 15 site, there are at least three different basalt flow layers observed within 60 m below the mare surface. Supporting evidence for flows about 20 m thick came from many additional photogeologic and petrogenetic studies (*Howard et al.*, 1973; *Gifford and El Baz*, 1978; *Spudis and Ryder*, 1985).

Many lunar lava flows lack distinct scarps, an observation that could reflect several possible causes—even lower viscosities, higher eruption rates, pooling of flows in shallow depressions, or subsequent destruction by impact cratering. In areas of continuing eruption, younger thin lava flows could also have covered and subdued older flow fronts (see maps in Chapter 10).

The primary landforms resulting from lunar basaltic volcanism are vast, smooth plains, indicating low lava viscosities and high eruption rates. Photogeologic, spectral, and other methods have been used to distinguish numerous individual flows, to recognize discrete eruptive periods, and to establish relative ages (e.g., *Schaber*, 1973a,b; *Boyce*, 1976). First, younger flows clearly overlap, spill over, or inundate older flows. Some different flows may have subtly different albedos and photometric properties, indicating different chemical compositions (*Pieters*, 1978). Flows from different eruptive periods invariably display different crater densities, indicating a substantial hiatus between eruption cycles (*Boyce*, 1976).

Crater-density or crater-erosion ages for diverse basaltic mare surfaces indicate that production of basin-filling volcanic lavas lasted about 500 m.y. in most major basins. [Detailed infrared reflectance observations (*Pieters*, 1978), combined with cratering ages (*Boyce*, 1976; BSVP, 1981) for a large number

of flows, are presented in detail in Chapter 10.] These synoptic observations indicate a great diversity in basalt compositions as well as in extrusion ages.

Remote-sensing studies indicate that we have not sampled all the compositional varieties of lunar lavas; neither have we sampled the oldest or youngest flows on the Moon.

Prominent basalt eruptions over the entire Moon lasted a minimum of 800 m.y., i.e., from 3.9 to 3.1 b.y. ago, as determined by radiometric age dates on lunar samples (*Head*, 1976a; also see section 6.1). On the basis of observed low crater densities on some formations, minor eruptions could have continued until as recently as 2 b.y. ago (*Schultz and Spudis*, 1983). The onset of basaltic activity is also not clearly defined. The oldest mare basalt sample, extracted from a highland breccia, apparently crystallized at 4.2 b.y. ago (*Taylor et al.*, 1983). However, corresponding surface units are not visible.

Indications of early basaltic activity are also supported by some photogeologic studies. *Schultz and Spudis* (1979) describe impact craters with low-albedo ejecta blankets ("dark halo craters") from a number of highland sites peripheral to large mare basins; they explain them as the results of impacts into basaltic deposits that are buried under a thin veneer of highland ejecta. It is also possible that very early basalt flows, buried by younger ones, exist inside the mare basins; clearly only the youngest (last?) flows composing the actual surface can be studied by remote sensing and photogeology. Although neither the onset nor the termination of lunar basaltic volcanism can be accurately defined at present, any activity after 3 b.y. ago is certainly of minor volumetric importance.

Vast expanses of basaltic lava flows dominate the mare basins, but other volcanic landforms, such as ash rings and lava domes, are present. Most are small in scale and of limited lateral extent. Many may be considered accessories to the major flows, and these illuminate the details of processes during flow emplacement. Others indicate different eruptive styles, including explosive volcanic activity. All are, however, a natural consequence of basaltic volcanism.

Sinuuous rilles. Meandering channels, called *sinuous rilles*, commonly begin at crater or crater-like landforms and end by fading downslope into the smooth mare surface or into a chain of elongate pits (*Greeley*, 1971; Figs. 4.27a,b). Sinuous rilles range in size from a few tens of meters to 3 km in width and from a few kilometers to 300 km in length (*Schubert et al.*, 1970). The channels are U- or V-shaped, but the original cross-sections have been modified by fallen debris from channel walls or ejecta from nearby craters. Their mean depth is ~ 100 m.

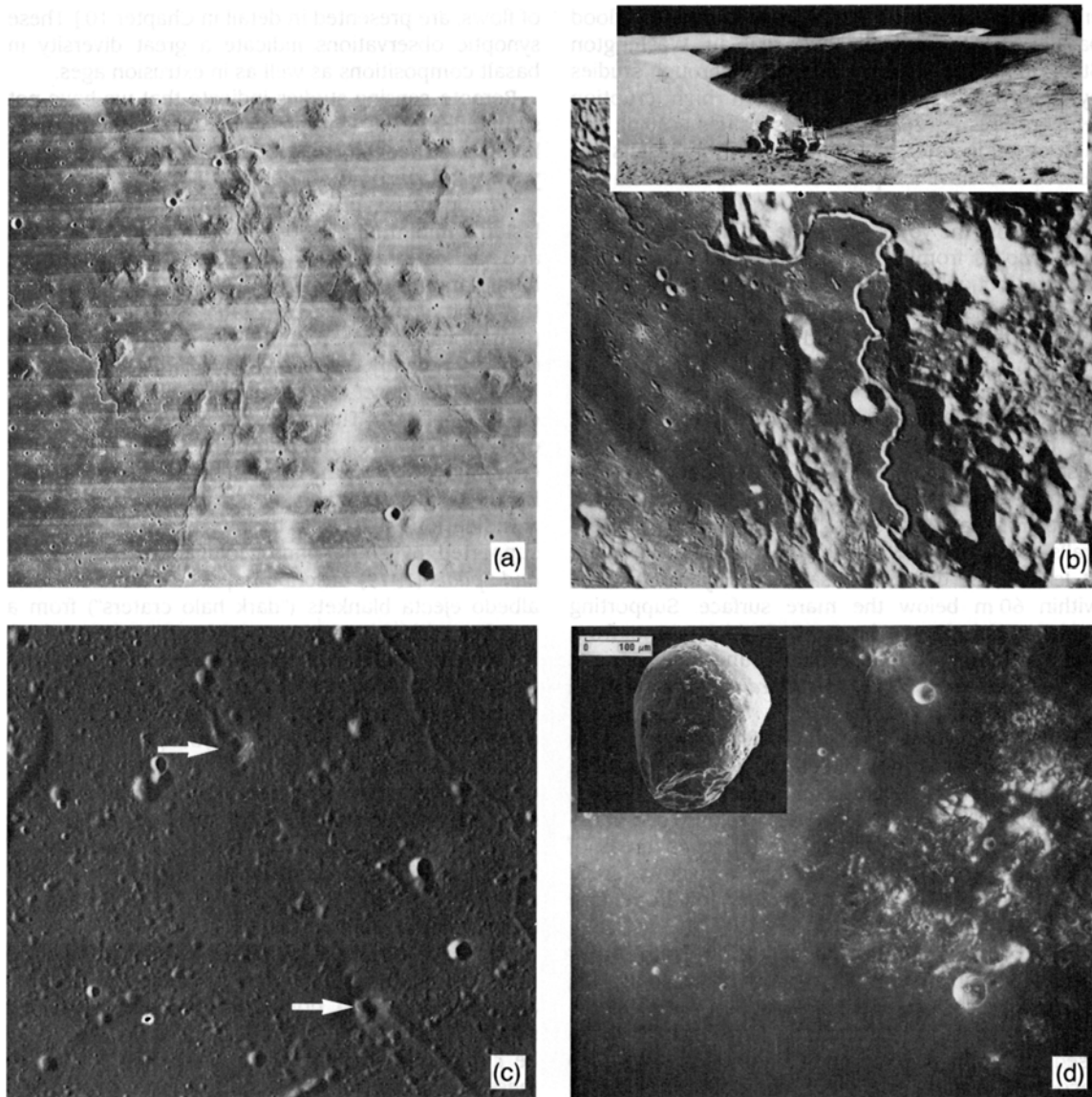


Fig. 4.27. Small volcanic landforms associated with basaltic volcanism. **(a)** Marius Hills, a plateau believed to be of volcanic origin, located in Oceanus Procellarum. This image shows dome-like landforms, sinuous rilles, elongate depressions, crater chains that may be partly collapsed lava tubes, and wrinkle ridges. The width of this image is ~165 km (NASA Photo LO IV-157 H-2). **(b)** Oblique orbital view of Hadley Rille, approximately 120 km long. The rille originates in a deep, wedge-shaped cleft (bottom right of picture) and disappears under the mare surface along the highland massif/mare contact (upper left) (NASA Photo AS15-M-0855). The surface photograph of Hadley Rille (inset) was taken during the Apollo 15 mission. The rille is 1500 m wide and 300 m deep and exposes several basalt flows, cumulatively at least 60 m thick (Greeley and Spudis, 1986) (NASA Photos AS15-84-11450 and 11453). **(c)** A chain of cone-like landforms (arrows), with craters and short rilles, located in Mare Serenitatis. The chain is approximately 25 km long (NASA Photo AS17-P-2317). **(d)** Dark pyroclastic mantle deposits, which cover part of the southeastern Serenitatis Basin and its rim (Taurus Mountains) near the Apollo 17 landing site. These deposits form an irregular band around the basin perimeter and over part of the adjacent highlands. The Apollo 17 landing site is located in the valley, center-right (NASA Photo AS15-M-1115). Inset: Scanning electron photograph of a partly crystalline glass droplet typical of the dark mantle deposit sampled by the Apollo 17 astronauts at Shorty Crater. The irregular coatings consist of flattened glass droplets and vapor condensates. These droplets are believed to have formed in lava fountains.

Although present everywhere on the Moon where there are mare deposits, most rilles are located along basin margins. The highest concentrations of sinuous rilles are in the Marius Hills (14°N, 50°W) and on the Aristarchus Plateau (27°N, 50°W). *Guest and Murray* (1976) mapped their distribution on the lunar nearside and farside.

Before Apollo, the three most popular hypotheses for the origin of sinuous rilles, which had already been detected by telescopic observations, were (1) collapsed lava tubes or open lava channels (*Baldwin*, 1963), (2) erosion of mare lavas by pyroclastic flows (*Cameron*, 1964), and (3) erosion by water (*Firsoff* 1961). The Apollo 15 site was deliberately chosen on the edge of Hadley Rille to study processes of rille formation. No pyroclastic materials were found, much less hydrated minerals or water (*LSPET*, 1972; *Howard et al.*, 1972). The relationship between sinuous rilles and basaltic lava flows was confirmed, but their detailed formation remains poorly understood.

Analogies with terrestrial lava channels and totally enclosed lava conduits, termed *lava tubes*, seem obvious. Molten lava commonly advances in open channels, and the build-up of levees by lateral spattering and overflow frequently accompanies these molten lava rivers. Build-up of substantial levees, together with crusting over of the lava surface may, in extreme cases, lead to lava tubes through which lava continues to flow. Widening and deepening of these channels by melting of the underlying rock by very hot lavas is also observed on Earth (*Hulme*, 1973; *Peterson and Swanson*, 1974). Such processes must have combined to form sinuous rilles on the Moon (*Oberbeck et al.*, 1971). However, there is a problem in scale. The terrestrial rilles are modest in size; the lunar ones are typically a factor of 30–50 larger than the terrestrial features in width, depth, and length. Roofs free-spanning >100 m across lava tubes can exist in the lower gravity of the Moon (*Oberbeck et al.*, 1969), but the unusually large sizes of lunar sinuous rilles seem to require a combination of reduced gravity, high melt temperature, low viscosity, and high extrusion rates.

Mare domes. Domes are broad, convex, circular to oval landforms of modest positive relief on the lunar maria (*Smith*, 1973; *Head and Gifford*, 1980). This term may have been an unfortunate choice because “volcanic dome,” when used on Earth, usually implies eruptions of highly viscous, silica-rich lavas (*MacDonald*, 1972) and, indeed, some observers argued initially for such silicic volcanism on the Moon. At this writing, no observations have been made of silicic lavas on the Moon.

Eighty low domes (slopes of 2° to 3°) have been mapped on the Moon’s nearside (*Guest and Murray*,

1976). Basal diameters range from 2.5 km to 24 km, and the domes may be 100 m to 250 m high. Most of the domes are located in the Marius Hills, where there are many other unusual volcanic features (Fig. 4.27a). Some domes have summit craters or fissures, and some grade laterally into the lavas of the surrounding mare surface. Domes with steep sides (7° to 20°) are also present in the Marius Hills. We know little about the formation mechanism(s) of domes, but they could have been formed by eruption of more viscous basaltic lavas, by intrusion as shallow subsurface laccoliths, or by mantling of large blocks of older rock by subsequent lavas. Interpretation of their origins must wait for future sampling and mapping.

Lava terraces. Small terraces within some craters and along mare-highland boundaries have been interpreted as “shorelines” left after withdrawal of erupted lava, either by drainage back into vents or by flow into a lower basin (*Holcomb*, 1971; *Young*, 1976; *Spudis and Ryder*, 1986).

Cinder cones. On Earth, cinder cones and spatter ramparts are the most common subaerial volcanic landforms developed around vents. They are developed by the explosive ejection of blobs or sprays of molten rock, which are then deposited as lava bombs and cinders around a vent. Less viscous sprays of smaller melt droplets can form fine ash that is interbedded with such coarser-grained deposits. Cones and spatter ramparts are commonly associated with basaltic lava flows, but they make up only a small part of the total volume erupted from a vent.

On the Moon, conelike landforms have been described on the maria in association with rilles. They are generally of very low albedo. Most cones are less than 100 m high, with diameters of approximately 2–3 km at the base (*Guest and Murray*, 1976; *Head and Wilson*, 1979). Some have summit craters less than 1 km in diameter (Fig. 4.27c). Lines of cones associated with rilles are interpreted as fissure vents.

Dark-haloed craters and pyroclastic deposits. Extrapolation to the Moon of the conditions that generate terrestrial cinder cones predicts that such features should be relatively modest, broad, pancake-shaped volcanic landforms, primarily because of the low gravity that allows wider areal dispersion of the spatter and bombs (*McGetchin and Head*, 1973). It has not been established that such features do exist on the Moon, but this origin has been proposed to explain the numerous *dark-haloed craters* on the lunar surface.

Dark-haloed craters are located along the margins of mare basins and along rilles or lineaments. Most are shallow depressions with rim deposits 2 km to 10 km in diameter. Like cinder cones, they generally

have albedos that are distinctly lower than the surrounding basalt surfaces.

A dark-haloed crater, named "Shorty," was sampled at the Apollo 17 site (Fig. 4.27d). It turned out to be nonvolcanic, but is apparently an impact crater that penetrated a deposit of loose glassy and partly crystalline droplets of orange to black color, producing low-albedo ejecta. This material, initially called the "orange soil," turned out to be pyroclastic deposits of volcanic origin (Heiken *et al.*, 1974; Butler, 1978; Delano, 1986) that clearly predate the formation of Shorty Crater. Whether other "dark-haloed" craters on mare surfaces are also impact craters that penetrate pyroclastic deposits or whether they are genuine volcanic features is currently undetermined (Schultz and Spudis, 1979; Head and Wilson, 1979).

Dark-haloed craters of unambiguous impact origin are also found in some highland areas adjacent to maria (Schultz and Spudis, 1979). It has been suggested that their ejecta consist largely of basaltic materials, excavated from below a thin veneer of material that has been ballistically transported or mass-wasted from the adjacent highlands. These underlying basalt flows may in fact be among the oldest ones on the Moon, indicating the existence of basaltic volcanism before 3.9 b.y. ago.

In summary, a variety of "dark-haloed" craters are recognized on the Moon; they may or may not be of volcanic origin. Dark-haloed craters located along rilles or in straight lines, similar to those located in the basaltic fill of Alphonsus Crater (Head and Wilson, 1979) or those spatially associated with the source area of the youngest Imbrium lavas (Schaber, 1973a,b), are excellent candidates for volcanic landforms.

The low-albedo volcanic materials around dark-haloed craters, even if exhumed by impact processes, are nevertheless of extreme interest, because they may have been originally associated with explosive, volatile-rich volcanic activity. Some dark albedo materials, e.g., the Apollo 17 "orange soil," are clearly pyroclastic deposits. Studies of this material from Shorty Crater revealed that the orange (glassy) and black (partly or completely crystalline) droplets formed during lava fountaining of low-viscosity, Fe-Ti-rich basaltic magmas (e.g., Heiken *et al.*, 1974). The surfaces of individual droplets have unusual concentrations of condensed volatiles, including Zn and S (Butler, 1978). Compositions of the droplets themselves are similar to compositions predicted in unmodified partial melts from the mantle (Delano, 1986). However, they could also represent magma that had been contaminated during its ascent by assimilation of wall rocks, so that the "basalt" rock compositions observed would therefore not represent the original mantle melts.

The observations of Apollo 17 orange glasses have helped to confirm the volcanic origin of green glass spherules returned from the Apollo 15 site. In addition, systematic searches for pyroclastic components in regoliths sampled by other missions have revealed the presence of still different pyroclastic glasses (e.g., Delano, 1986). Although these glasses are of trivial volume, they are important samples in understanding lunar volcanism, for they demonstrate that lava fountaining took place on the Moon. A similar pyroclastic origin may explain the dark mantle deposits of significant areal extent that occur along the inner rim of Mare Serenitatis (Adams *et al.*, 1974; Hawke *et al.*, 1979).

4.2.2. Filling of the Maria

Basaltic volcanism and large-scale impact basins are spatially related on the Moon. Basin formation, followed immediately by collapse of the transient basin cavity, leads to large-scale fracturing of the crust and thus provides both the structural framework and the conduits along which basaltic magmas generated at depth may ascend to the surface. Most such conduits seem to be located just within the edges of the mare basins, where large-scale slump zones should be prominent (Schaber, 1973a,b; Head, 1976a).

Deep melting can be produced by several mechanisms associated with the formation of large impact basins. The lower thermal conductivity of thick basin-filling ejecta blankets, which is related to their high porosity, can produce significant upwarping of mantle isotherms, thus promoting localized melting below a basin (Arkani-Hamed *et al.*, 1973). Other factors include the actual physical uplift of mantle materials during basin formation, the decrease in hydrostatic pressure caused by the sudden removal of overburden, and the resulting decrease in melting temperature with decreasing confining pressure (Brett, 1976). In addition, massive, unfractured sheets of fresh impact melt produced during basin formation, possibly a few kilometers deep, may act as an impermeable plug that forces the ascending lavas from the center of the basin to its edges.

Significant time may elapse between the formation of a large *mare basin* by impact and its subsequent filling with basaltic lava flows to form the dark lunar *maria*. Current information fixes the formation of the Imbrium Basin at about 3.9 b.y. ago, but the lavas that fill it (sampled by the Apollo 15 mission) are about 3.3 b.y. old.

Many details of how basins are formed and filled with lavas are not well understood, but there is little question that basin formation has provided the

structural framework for widespread basalt eruptions. With few exceptions, the lava flows that form the dark lunar maria are confined to basin interiors, but on occasion the lavas seem to have spilled over the basin rims to flood adjacent terrains.

It is important to note that not all large impact basins have triggered subsequent volcanic activity. Most basins on the nearside are flooded by basalts, but only a few on the farside are flooded. This difference may be caused by the existence of a thicker farside crust, a condition that is also suggested by gravity observations and other geophysical considerations (*Bills and Ferrari, 1976; Solomon et al., 1982*). The processes leading to filling of the basins with lavas also appear to be generally related to the chronology of basin formation. Many old, highly-degraded basins are devoid of volcanic activity and lava fillings; most major, well-preserved basins, i.e., the geologically younger ones, seem to be filled by lavas (*Head, 1976a*). There are exceptions to these trends, however, and there is still no general consensus nor any accepted model to relate volcanic activity directly to the time of basin formation or to the thickness of the lunar crust. Clearly, most volcanic activity has occurred over a limited area of the Moon and is confined, with minor exceptions, to the lunar nearside (*Head, 1976a; BVSP, 1981*).

The sequences of basaltic eruptions, and their implications for basalt origin and for the long-term evolution of the basins themselves, are illustrated best by the youngest basins: *Oriente* (*Head, 1974a; Moore et al., 1974*), *Imbrium* (*Schaber, 1973*), and *Serenitatis* (*Head, 1979; Solomon and Head, 1980; Solomon et al., 1982*). *Mare Orientale*, the youngest large lunar basin, is only partly filled with basaltic lavas. Its interior seems dominated by a relatively flat-lying sheet of nonbasaltic(?) impact melt, which shows modest local topographic relief. The subsequently erupted basaltic lavas have spilled over part of this melt sheet and occupy only the basin interior. *Oriente* may thus represent the earliest phases of basin-filling by lavas. Eruptions began within the innermost ring (the "Inner Rook"; see Fig. 4.28a) and along the ring's concentric fault systems. Well-preserved fissure vents and domes are also visible in association with the next outward ring, the Rook Mountains, which form the major inner ring of *Oriente*. Eruption vents are located along ring faults (Figs. 4.28b,c).

Mare Imbrium, although older than *Oriente*, is the youngest major basin located entirely on the lunar nearside; its ejecta deposits cover a substantial fraction of the entire nearside. Total lava fill in the *Imbrium* Basin is more substantial than in *Oriente* (*Head, 1982*). Unlike *Mare Orientale*, no sheet of apparent impact melt is visible. Significantly, most of

the annulus between the major interior ring and the major topographic rim (the Apennine Mountains) is also covered by lava flows, except for the *Palus Putredinus* region in *Imbrium's* southeast corner. As described by *Schaber (1973a,b)*, lavas were erupted predominantly from the basin periphery, in this case close to the major topographic rim (Fig. 4.26). Did earlier eruptions occur in more interior locations, as in *Oriente*? We do not know. It is clear, however, that there are three distinct eruptive episodes in *Mare Imbrium*, based on crater-density ages; the volcanic activity represented by these (last) three eruptive episodes spans 0.5 b.y. (3.7 to 3.2 b.y. ago).

The *Serenitatis* Basin is somewhat older than *Imbrium*. Its interior rings are completely flooded, and basaltic lavas occupy the entire basin inside the major topographic rim. As in the case of *Imbrium*, three major episodes of lava flows are observed (Fig. 4.29). The history of the *Serenitatis* Basin has been extensively modeled by *Solomon and Head (1980)*. They propose an early, dilatational stage of the entire lunar crust during basin formation and basaltic activity, followed by a compressional stage as the crust cooled and contracted (*Golombek, 1979; Binder, 1986*). The oldest lavas, Stage I, erupted in the southern basin rim of *Serenitatis*. Some of them spilled over into the adjacent *Mare Tranquillitatis*, where they were collected by the Apollo 11 mission and dated at 3.65 to 3.85 b.y. ago.

During this period, the center of the *Serenitatis* Basin sank under the load of the Stage I lavas. The subsequent Stage II lavas therefore erupted into a newly created shallow depression. They form an approximately concentric annulus within the Stage I lavas; overlap relationships and crater densities leave little doubt that these lavas were erupted later. The last eruptive episode, Stage III, produced the youngest basalts; these occupy the basin center because downwarping had continued. Some Stage III lavas, however, also spilled into embayments around the adjacent *Imbrium* Basin, illustrating that topographic slopes and gradients were small.

The major conclusion of this model (*Solomon and Head, 1980*) is that basin floors downwarp under successive basalt fillings and it is therefore possible that total basalt-fill thickness, predominantly from early eruptions, may exceed a few kilometers. This process also accounts for the existence of compressional ridges (Fig. 4.29c; see also *Muehlberger, 1974*). The continued downwarping causes centrosymmetric foreshortening, and thus compression, forming concentric bands of compressional ridges.

Most petrologic models of lunar basaltic magmas suggest that they originated by partial melting at depths of 200–400 km (*Kesson, 1975; BVSP, 1981; Delano, 1986; Binder, 1986*; also see section 6.1.8).

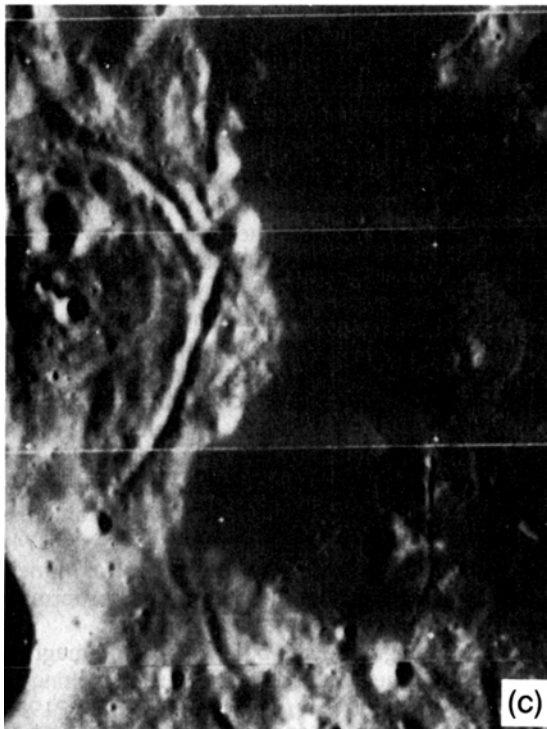
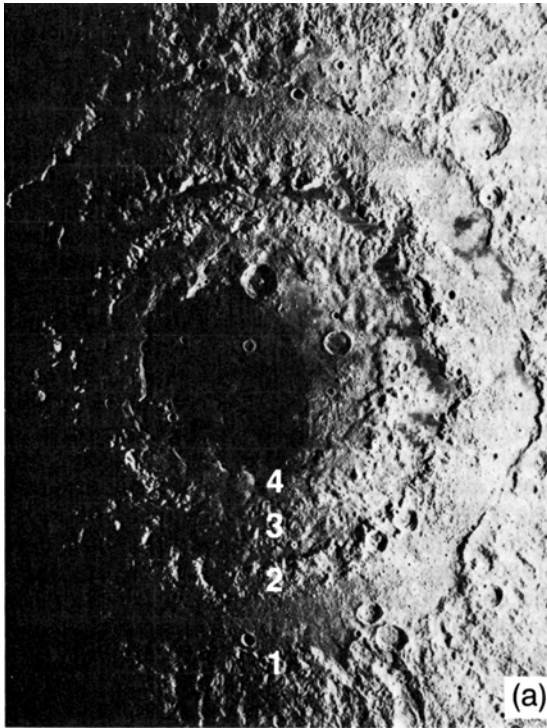


Fig. 4.28. Basaltic volcanism in Mare Orientale (at 20°S, 95°W), showing details of lunar basaltic volcanism that may be applicable to other, more extensively flooded, multiring basins. **(a)** Overview of Orientale, illustrating the well-preserved major rings: Innermost ring (4), 320-km diameter; Inner Rook (3), 480-km diameter; Outer Rook (2), 620-km diameter; and Cordillera (1), 930-km diameter. Note that dark basalts cover part of the basin interior as well as some depressions between the major rings. Occurrence of basalts in such different locations and as isolated patches in a number of depressions appears to require a large number of individual vents within the basin and between the rings (NASA Photo LO IV-187M). **(b)** Detailed view of the northeastern quadrant of Mare Orientale. Dark basaltic lavas have been erupted into the concentric depression formed between the Inner and Outer Rook Mountains, suggesting the existence of a number of conduits associated with basin-generated faults and slump zones. None of these basalts appear to have spilled into the basin interior; the interior fill must therefore have come from more centrally located vent areas. (NASA Photo LO IV-187 H₂). **(c)** Photographic enlargement of the lower right corner of **(b)**, illustrating examples of possible fissure vents (north-south trend) and associated volcanoes. The latter form low, broad shields (some 6 to 8 km in diameter at the base) around the vents. **(d)** Mare filling within the south-central Orientale Basin. Dark, smooth plains are interpreted to be basaltic lavas; the presence of sinuous rilles and of circular subsidence features suggests the presence of surface liquids and flow (NASA Photo LO IV-195 H₁).

These magmas had lower densities than the surrounding rocks, and therefore tended to rise as large bodies of melt. At shallower depths in brittle crust, the magma most likely followed fractures and faults induced by basin-forming impacts or by local extension of the crust caused by basin subsidence (Fig. 4.29c). The location of volcanic conduits is thus strongly affected by impact-basin structures in the crust (Solomon and Head, 1980).

Photogeologic studies reveal that fissures are the sources for some of the lunar lavas. In their models of lunar volcanic eruptions, Head and Wilson (1979) determined that such fissure vents need be no wider than 10 m to allow the high eruption rates required for long lava flows. They also determined that the speed of rising magmas must have been >0.5–1.0 m/sec to maintain lava fountains, even if no explosive lava fountaining activity occurred.

Vesicles (bubbles) occur within lunar lavas and pyroclasts indicating that a volatile phase (or phases) was present when the rocks were molten. The vanishingly small water content of lunar lavas indicates that—unlike terrestrial lavas—water was not a significant gas component. Sato (1978) presents evidence suggesting that CO was the main gas phase. Lunar pyroclastic activity, driven by CO, appears possible. Head and Wilson (1979) determined that only 250–750 ppm of CO is required to disrupt magmas at depths of 15 to 40 m, producing explosive activity by the growth of large bubbles that burst and throw spatter clots. Based upon analysis of orange-glass pyroclasts from the Apollo 17 site, Heiken and McKay (1978) favor semicontinuous lava fountaining as the main type of lunar explosive volcanism.

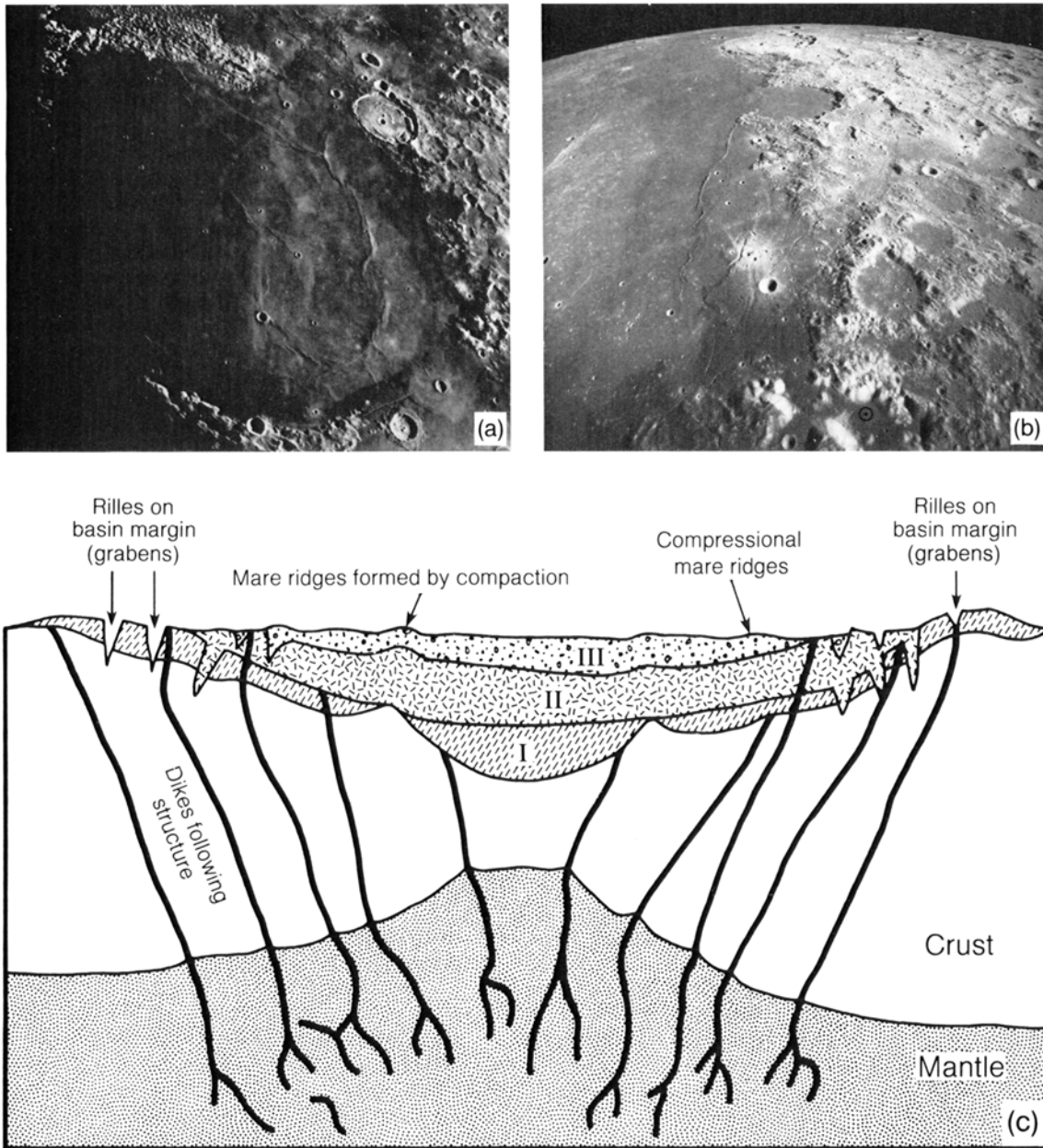
4.2.3. Volume Estimates of Basaltic Mare Fill

The total volume of the Moon's volcanic deposits is an important quantity in defining the extent of melting that took place within the lunar mantle

(Kesson, 1975; Delano, 1986). How much of the lunar mantle was melted to produce the basaltic lavas? This question addresses two important points: (1) What was the degree of partial melting, i.e., the fraction of melt produced per unit volume of mantle material? (2) How much of the entire lunar mantle was involved? A given volume of basalt at the surface can obviously be produced by large degrees of partial melting of a small mantle volume or by a small degree of partial melting of a large part of the mantle. The total volume of erupted basalt—an independently-determined quantity—can be used to constrain geophysical/geochemical models involving various bulk compositions and thermal histories of the lunar mantle.

The area occupied by basaltic deposits is readily measured—about 17% of the Moon's surface, or about 6.4×10^6 km². No direct measurements of the thickness of basaltic mare deposits have been made, however. Active seismic profiling during the Apollo missions did not yield good estimates of basalt depths, even at local scales, at the Apollo landing sites (Kovach and Watkins, 1973). Electromagnetic sounding of the maria from orbit (Peeples *et al.*, 1978) yielded discontinuities (interpreted as the base of the basalt fill) at about 1.6–2 km for Mare Serenitatis, 1.4 km at the center of the Serenitatis Basin, and about 0.8–1.0 km in the peripheral shelf areas of Mare Serenitatis. These data apply to single-line profiles across the basins, and they cannot be readily extended to other areas to calculate total basalt volumes.

Indirect estimates of total lava volume are obtained from studies of impact craters flooded by mare basalts, a technique pioneered by DeHon (1974). By using the ideal crater shapes described in section 4.1.2 (Table 4.1), in particular the height of the fresh crater rim, one can estimate how thick the basalt stack filling the crater must be. The crater diameter and the height of the present rim crest



above the basalt surface can be measured from photographs. Subtraction of the present height from the estimated initial rim height (above the initial lunar surface) yields the cumulative thickness of basaltic fill. This approach was applied to all observable flooded craters, generally only 20–40 craters per mare-filled basin; from these data isopach maps of the thickness of basalt filling were constructed (DeHon and Waskom, 1976; DeHon,

1979). These maps indicate basalt thicknesses of 0.5–1 km in the shelf areas, increasing to a few kilometers in the basin interiors (Fig. 4.25). The total volume of lunar basalt erupted is thus estimated at $\sim 6.5 \times 10^6 \text{ km}^3$, i.e., <1% of the lunar mantle volume.

These estimates by DeHon use the ideal shape of fresh lunar craters; Hörz (1978), on the other hand, suggested that lower rim heights are more commensurate with the average degradational state of

Fig. 4.29. Basaltic volcanism within the Serenitatis Basin. **(a)** Earth-based, telescopic view of Mare Serenitatis. The morphologic rim encloses substantially more dark basaltic fill than is the case for the Orientale Basin. The outermost zone of basalts is the oldest (based on crater density counts) and also has a very low albedo. This outer zone also contains extensive graben systems that formed in response to tensional forces (see section 4.3). The inner basin is flooded by younger basalts. The basalt surfaces display many compressional ridges, produced either by compressional tectonics or by surface buckling over subsurface basalt intrusions. **(b)** Portions of eastern Mare Serenitatis, illustrating the mare/highland contact relationships. Dark basaltic lavas have flowed out of the basin into older craters, such as Le Monnier (near the top of the photograph; 70-km-diameter crater). Dark mantle deposits, which underlie the lowest-albedo areas, are interpreted as volcanic ash. The Apollo 17 landing site (marked by the circled dot) is located slightly outside the major basin rim; this mission returned a variety of highland rocks, mare basalts, and pyroclastic rocks (NASA Photo AS17-M-0939). **(c)** Idealized cross-section of the lunar crust and mantle under Mare Serenitatis, illustrating some general ideas about the volcanic eruption history and the location of magma conduits as inferred from photogeology and from thermal modeling of the lunar crust. The prolonged eruption of basaltic lavas into the Serenitatis impact basin resulted in the downwarping of the basin floor and the gradual filling of this depression by successively younger basalt flows. This filling took place principally during three major episodes, labeled I through III from earliest to last (see also section 4.3). Peripheral downdropped grabens formed early during a period of extension, and compressional or “wrinkle” ridges were produced during a later stage of compression as the crust cooled and shrank. The locations and shapes of the basaltic conduits are highly idealized, as is the assumed upwarping of the lunar mantle.

impact craters. This correction would decrease the basalt thicknesses estimated by DeHon and coworkers by a factor of ~ 2 . A more serious shortcoming, however, affects the technique itself: the implicit assumption that all the now-flooded craters were originally formed on pristine basin floors before any lava had been erupted. The above volume estimates are therefore minimum values.

Larger estimates of erupted lava volume result if one instead assumes a specific geometry for the original impact basin cavities, modeled after the Orientale Basin, which is the youngest and least-filled basin (Head, 1977). Assuming similar cavity geometries for all the other basins, and measuring the present degree of flooding (elevation of the lava-filled mare surface relative to rim height), total erupted lava volumes of $6\text{--}7 \times 10^6 \text{ km}^3$ are obtained. A maximum volume of $3\text{--}4 \times 10^7 \text{ km}^3$ is obtained by assuming that all basins were filled to the brim, which is obviously not the case.

Other constraints on basalt thickness are derived from “mascons,” the positive gravity anomalies observed over many (but not all) of the basalt-filled mare basins (see Chapter 10). When the excess mass required to produce the observed gravity anomaly is assumed to be entirely basalt fill, minimum estimates for basalt thickness of 1–2 km are obtained (Phillips *et al.*, 1972; Phillips and Lambeck, 1980; Solomon and Head, 1980). These are minimum estimates, however. It is not known whether there is additional basaltic fill below the equilibrium gravitational surface used in the modeling. Evidence for the presence of such deeper basalt fill is seen in the fact that most large, unfilled craters have negative gravity (Bouguer) anomalies (Phillips and Dvorak, 1981), even the highly degraded Grimaldi Basin.

Solomon and Head (1980), in addressing the problem of lunar melting, have combined most geophysical, photogeological, and petrographic evidence with rheological and thermal modeling of the lunar crust. Their most recent models allow about $6 \times 10^6 \text{ km}^3$ of basalt to be produced within the Moon.

In summary, the total volume of basaltic magma generated within the Moon is not precisely known, but current estimates yield values of between 10^6 and 10^7 km^3 . Even the maximum estimates are $<1\%$ of the volume of the lunar mantle. It is therefore safe to infer that high degrees of partial melting, involving large regions of the entire mantle, did not take place within the Moon. Uncertain as these estimates are, they are nevertheless adequate to provide useful constraints in reconstructing the composition of the lunar mantle and its thermal history (see BVSP, 1981).

4.3. TECTONIC ACTIVITY

Tectonic activity refers to the deformation of the rocks of a planet by external or internally-produced forces. These forces can produce a wide range of observable deformation features—faults, folds, mountain ranges, and zones of volcanism—at or near the planet’s surface. These features, in turn, provide information about the interior of a planet, its structure, its mechanical properties, its thermal state, and its past history.

The volume of a planet over which such forces are applied (*stress fields*) can vary from local to global, and the stresses themselves can be either compressive or tensional. Depending on the magnitude of the stress, the rate of application, and the nature of the material under stress, deformation can occur by

either gradual ("plastic") deformation or by abrupt failure (*rupture*). Interpretation of the resulting features is complicated by several circumstances, including the superposition of local stress fields onto global ones and the alternation between tensional and compressional stresses in a given area as time passes.

Most information about lunar tectonic activity has been obtained from surface images, from surface seismometers emplaced at Apollo landing sites, and from modeling the thermal state of the lunar crust and mantle. These data indicate that, in comparison to the geologically active Earth, internal tectonic activity on the Moon is a minor process. The energy released by lunar earthquakes ("moonquakes") may be $<10^{-12}$ as much as the seismic energy released by the Earth. Furthermore, the crust of the Moon appears to be thick, rigid, immobile, and cool in comparison to the crust of the Earth, which is characterized, even today, by large-scale motions and by a high degree of partial melting. This comparison is reinforced by the fact that the returned lunar samples show virtually no textures typical of slow, low-strain-rate ("plastic") deformation, features that are abundantly displayed in a wide range of terrestrial rocks.

Under these conditions, much lunar tectonic activity is driven by forces external to the Moon—tidal stresses and large meteorite impacts. Internally-generated tectonic activity results from the changing thermal state of the Moon, and its effects include global expansion and contraction, as well as the production of volcanic lavas.

4.3.1. External Forces

Impact. As discussed in section 4.1, impact events create a large number of tectonic features associated with complex craters and large impact basins. These features include wall terraces, multi-ring mountain scarps, and radial fracture (*fault*) systems (Fig. 4.12). It is likely that additional movement occurred along these impact-produced faults for some time after the impact event itself, especially in the case of multiring basins.

The large cavity created by the basin-forming impact, the extensive subsurface shattering of crustal rocks, and the resulting lateral and vertical movements clearly represent a substantial disturbance of the pre-impact global stress field. After the impact, the lunar crust will tend to adjust to any residual stresses, probably by subsequent movements along the impact-produced faults. Such faults may be kept active for long periods of time, or may be reactivated by seismic energy from subsequent impacts in the vicinity (Titley, 1966; Schultz and Gault, 1975a,b). The

seismic energy emanating from a hypervelocity impact is generally 10^{-3} to 10^{-4} that of the initial projectile kinetic energy (Latham *et al.*, 1970a,b), and should be adequate to produce significant new movement on older, preexisting faults.

Another form of tectonic activity is associated with large-scale impact basins that are subsequently filled with basalts. The additional loads of basalt can produce significant stress within and adjacent to the filled basins. Near the basin edge, the radial and tangential stress components are tensile and mildly compressional, respectively (Melosh, 1978; Maxwell, 1978; Solomon and Head, 1979; Comer *et al.*, 1979). These combined stresses can produce concentric downdropped valleys (grabens) at the edges of the maria, a situation illustrated by Mare Humorum (Fig. 4.30). The basalt loading also produces down-warping of the basin center, generating compressional stresses and leading to foreshortening of the surface and the formation of wrinkle ridges (Fig. 4.31; Muehlberger, 1974; Lucchitta, 1976; Solomon and Head, 1979).

Post-impact gradual isostatic adjustments of large-scale crater and basin cavities may also have occurred in response to the lunar gravity field. However, the high viscosity of the solid lunar crust has prevented such isostatic adjustment from occurring rapidly, at least throughout the period represented by the preserved cratering record. Many large craters that are not filled with lavas still retain their original negative gravity anomalies (Phillips *et al.*, 1972; Phillips and Lambeck, 1980; Phillips and Dvorak, 1981). Furthermore, the Apennine Mountains, which were formed with the Imbrium Basin 3.9 b.y. ago, are even now not in isostatic equilibrium (Ferrari *et al.*, 1978). These conclusions are complicated by evidence of definite post-impact deformation in other craters. Portions of some large crater floors seem to have been uplifted and cut by grabens. (Hall *et al.*, 1982) have interpreted these features as evidence for tectonic activity associated with isostatic readjustment within craters.

Tidal forces. The body tides on the Moon, which are generated by the gravitational field of the Earth, together with the tidally locked or synchronous rotation of the Moon, cause the Moon to deform from a sphere into a triaxial ellipsoid (Jeffreys, 1962). The amount of deformation varies with the third power of the Earth-Moon distance. At the present Earth-Moon distance of about 60 Earth radii, the theoretical difference between the maximum and minimum radii of the Moon is about 65 m. Since the lunar orbit is elliptical, the monthly variations in the Earth-Moon distance cause this value to vary by about 40%. As a result, tidal stresses of a few bars build up and decay in the lunar crust every month.

These stresses are far too weak to produce independent tectonic activity in the lunar crust. However, the tidal stresses of ~ 0.2 bar at depths of 700 to 1100 km in the Moon seem adequate to generate or trigger the weak, cyclic, deep moonquakes (Lammlein, 1977), for such activity is strongly correlated with the Moon's position in its orbit around the Earth (see section 3.7 for a discussion of seismic stability).

Most theories of the origin of the Moon require that the Earth-Moon distance was only a few Earth radii early in lunar history (MacDonald, 1964; Binder, 1978; Thompson and Stevenson, 1983) and conclude that this distance has increased with time. If this is correct, or if the Moon underwent any reorientation events (Melosh, 1975), then at Earth-Moon distances

of $< 8 R_E$, tidal and synchronous rotational stresses of up to 100 kbar could develop within the early lunar lithosphere. The stresses required to produce major tectonic deformation on the Moon are on the order of 1 kbar at the surface and 10 kbar at the base of the crust. Therefore, these early tidally-induced stresses must have caused intense deformation, with probable faulting throughout the entire crust. Unfortunately, the period during which this intense faulting must have occurred was also the time when the Moon underwent its most intense cratering (section 4.1), a process that would have obliterated the surface effects of such deformation.

Despite the obliterating effects of the intense bombardment, evidence of early, global tectonic deformation may still be preserved. A number of

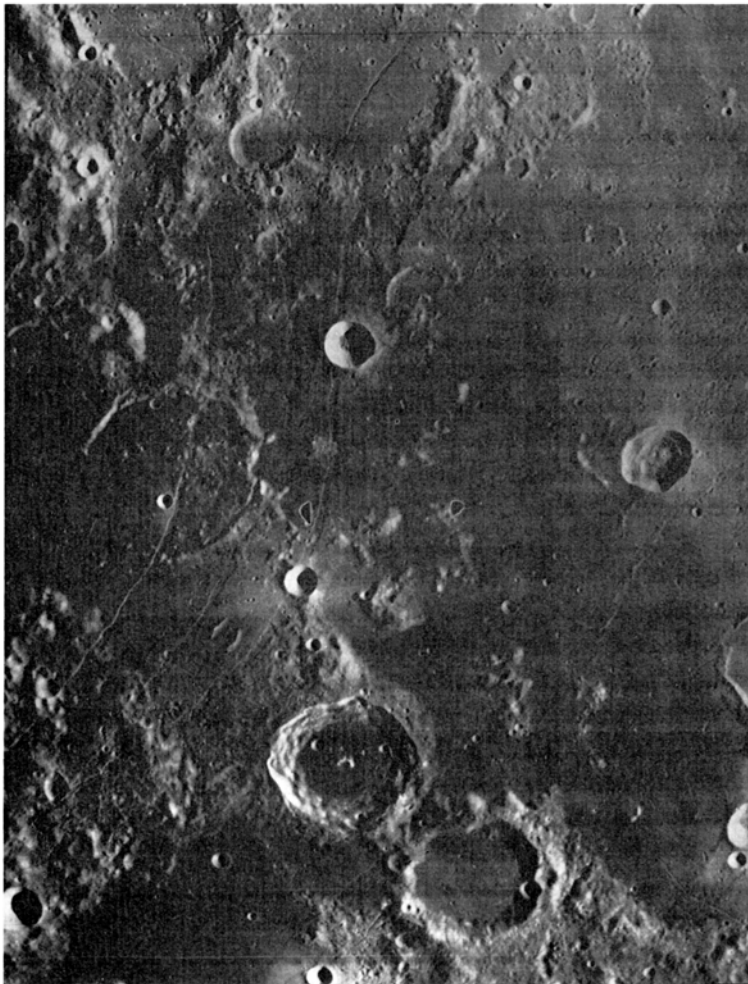


Fig. 4.30. A system of concentric, down-dropped valleys (*grabens*) at the southeastern edge of Mare Humorum. The width of the graben system is approximately 55 km, and individual grabens are a few hundred kilometers long. Note that the grabens are filled with basaltic lavas, indicating that they were relatively early extensional features. The grabens extend, virtually unobstructed, from the mare into the adjacent highlands, and they also cut across the rim of a large, preexisting flooded crater. These observations indicate that the grabens reflect a substantial, possibly deep-seated, basin-wide stress field. Two younger and much smaller impact craters (center) were clearly formed after the graben. The fact that graben-forming movements had completely ceased by this time is indicated by the sharp, undeformed crater rims. Such observations, combined with crater frequency counts, limit the period of extensional tectonics and graben formation to early lunar history, coincident with the early generation of large volumes of basaltic lava (NASA Photo LO IV-132H₁).

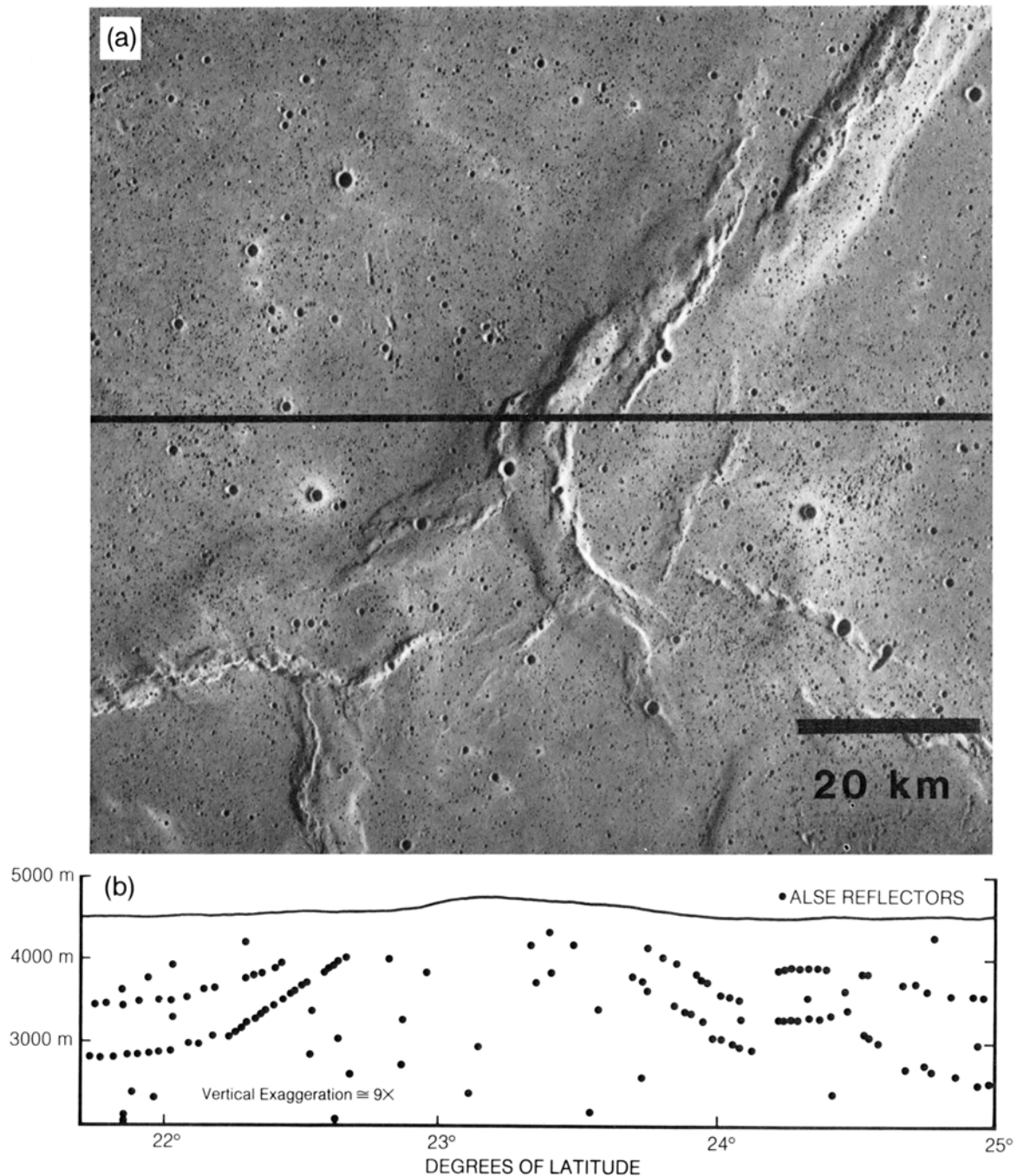


Fig. 4.31. Lunar compressional ridges. **(a)** Orbital photograph of a major wrinkle ridge system in southeastern Mare Serenitatis. The *en echelon* offsets of ridges and crests indicate compressive stress. The arcuate shape of the ridges (concentric to the basin) indicates substantial centrosymmetric foreshortening, perhaps 0.5% to 0.8% (Muehlberger, 1974; Maxwell, 1978) (NASA Photo AS17-M-0451). **(b)** Penetrating radar reflection profile obtained by the Apollo Lunar Sounding Experiment (ALSE) across the ridge depicted in **(a)**; horizontal line in **(a)** represents the ground track of the Apollo 17 spacecraft, along which these measurements were taken. Note substantial upwarping, possibly folding and faulting, of the basaltic subsurface layers down to depths of approximately 2 km below the surface (from Maxwell, 1978).

investigators (Habakov, 1949; Strom, 1964; Allen, 1975; Fagin *et al.*, 1978; Hale, 1980) have suggested that a systematic, global pattern of lineaments (grabens, horsts, linear scarps, linear crater wall segments, etc.) exists; this pattern has been called the "lunar grid" system. Because the overall mapping of the Moon is still incomplete, other scientists maintain that only local lineaments occur, unrelated to any global stress system.

4.3.2. Internal Forces

Thermal stress. Models of lunar thermal history indicate that thermal expansion during the first billion years of the Moon's existence would have produced tensional stresses in the lunar crust and that contraction during the subsequent 3.5 b.y. until now have produced compression (Solomon and Chaiken, 1976; Binder and Lange, 1980). The exact magnitude of these tensional and compressional stresses is still a matter of debate. Some models indicate that stresses during the early phase of expansion were about 1 kbar, or two orders of magnitude smaller than the stresses produced by tidal effects and synchronous rotation during the same period. Clearly, very early lunar tectonic activity was totally dominated by tidal stresses; internally-generated stresses were insignificant.

There is, however, clear photogeological evidence of tensional stresses in the Moon between 3.9 and 3.6 b.y. ago. A period of normal faulting, mainly characterized by the production of downdropped grabens, began at the time when the oldest mare lavas were deposited (Lucchitta and Watkins, 1978). Many of these grabens are found in maria such as Humorum (Fig. 4.30) that display positive gravity anomalies (mascons). Although these grabens are most likely related to stresses caused by filling of the maria with thick layers of basaltic lava, they could not have formed unless mildly tensile global stresses were also present (Melosh, 1978; Solomon and Head, 1979; Comer *et al.*, 1979). Similar grabens and normal faults are also observed in areas unrelated to maria and mascons, and these features could reflect global tensional stresses; the Sirsalis, Hyginus, Triesnecker, and Ariadeus Rilles are good examples (Fig. 4.32).

Subsequent to this episode of tensional stresses before 3.6 b.y. ago, the Moon's global stresses became compressional, and internally driven tectonism ceased for the last 2.5 to 3 b.y. These compressional stresses built up so slowly that a few billion years may have been required to accumulate sufficient stress (>1 kbar) to cause small-scale compressional features (*thrust faults*). Photogeologic observations reveal small scarps and thrust faults, generally less than 10 km long. Based on cratering

ages, these faults appear to be less than ~700 m.y. old (Binder and Gunga, 1985). Examples of such young thrust faults are illustrated in Fig. 4.33. It is estimated that there are some 2000 such features in the lunar highlands. A few of these scarps extend into the adjacent maria, where they appear as ridges. Other mare ridges could also be thrust faults (Muehlberger, 1974).

These compressional tectonic features are interpreted by Binder and Gunga (1985) to indicate that, since about 2 b.y. ago, the Moon had cooled and contracted sufficiently to have produced global compressive stresses and associated thrust faulting. In their view, the Moon is not tectonically dead, and it has not been firmly established that there is no seismic hazard to future exploration and habitation (see section 3.7). Long-term seismic observations, combined with other geophysical exploration, are required for a better understanding of the Moon's present thermal state, its detailed crustal structure, and its current deformation.

Volcanic intrusions. While most mare ridges are believed to have been caused by thermally-generated compressive stresses, some ridges may have been produced by intrusion of magma just below the surface (Strom, 1964). One model for the development of craters with fractured floors calls for intrusion of magma beneath the crater floors, resulting in uplift (Schultz, 1976b). Humboldt Crater may be one example of such uplift and associated fracturing (Fig. 4.34).

4.4. LUNAR STRATIGRAPHY

Stratigraphy is a branch of geology that deals with the recognition of different rock units, the establishment of geometric relations between them, and the use of these relations to determine the origin and history of the rocks involved. The goal of lunar stratigraphic studies is to apply the principles of terrestrial stratigraphy to the Moon in order to decipher its geologic history. Over 25 years ago Shoemaker and Hackman (1962) applied a fundamental principle of terrestrial stratigraphy to the Moon, the *Law of Superposition*, which states simply that older rocks are overlain, cut, or intruded by younger rocks. This is an obvious condition, but it is a powerful method for unraveling sequences of geological events on both the Earth and the Moon.

Although the Law of Superposition allows relative ages to be established, absolute age information is necessary to place lunar or terrestrial geologic history into an absolute time frame or to determine how long a specific epoch or event lasted. In terrestrial studies, such absolute ages have been provided by radioactive-decay measurements

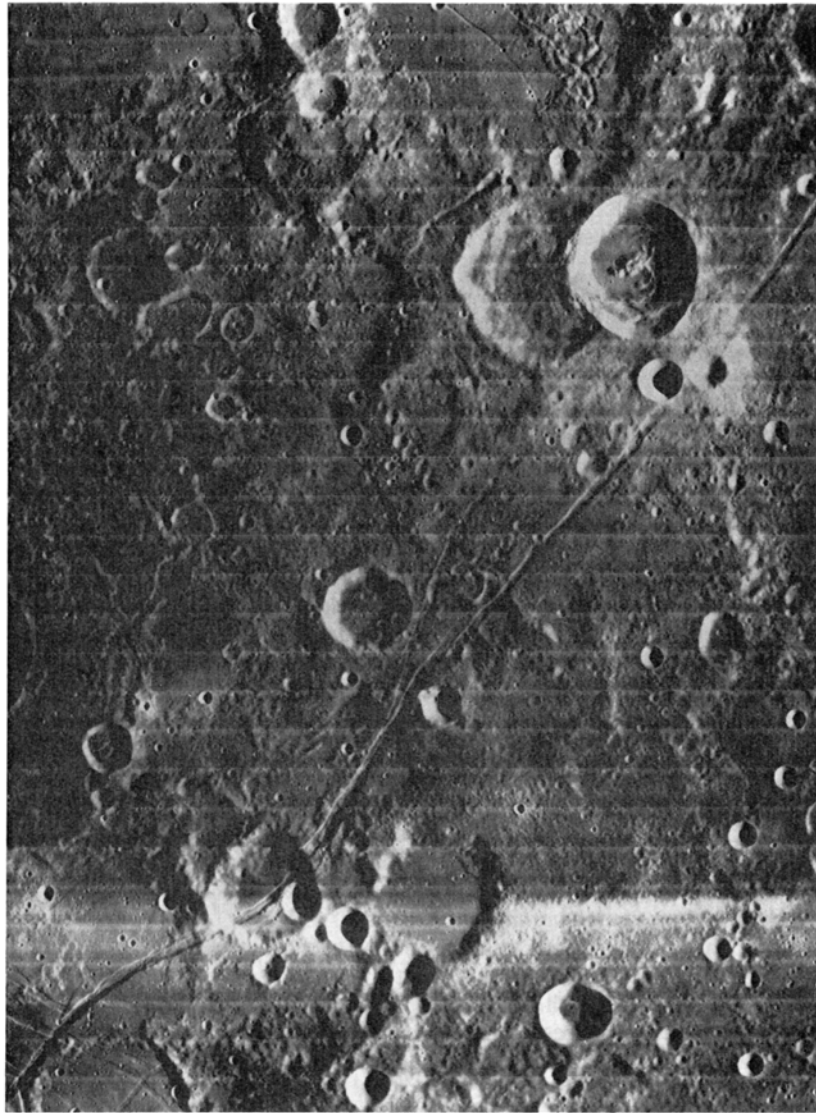


Fig. 4.32. Sirsalis Rille, running from upper right to lower left, a possible example of early extension unrelated to loading of the mare basins by basaltic lavas to produce mascons (NASA Photo LO IV-161 H₂). The northeast-trending rille, located on the outer fringes of the Orientale Basin ejecta blanket, is 300 km long.

applied to well-characterized terrestrial rocks. However, dating of even ideal rocks is complicated and time-consuming, and terrestrial stratigraphers have only a relatively small number of absolute chronological tie-points for the Earth's record. These data provide calibration points for the overall geological record of the Earth. More detailed age measurements can then be made by indirect means that allow interpolation between the absolute chronological reference points. On Earth, such interpolations are based on the fossil record or on the record of polarity-reversals of the Earth's magnetic field.

On the Moon, which lacks both fossils and a significant magnetic field, the impact crater populations and the areal density of craters can be used to determine ages. Using absolute ages for lunar surfaces, determined by age measurements of returned lunar samples, the crater population can then be used to determine the ages of other surfaces. These measurements have only begun, and few lunar surfaces have been precisely dated. Furthermore, for a number of reasons, many lunar rocks may not be dated accurately even when modern isotope-geochronology techniques are used (see sections 6.3 and 6.4).

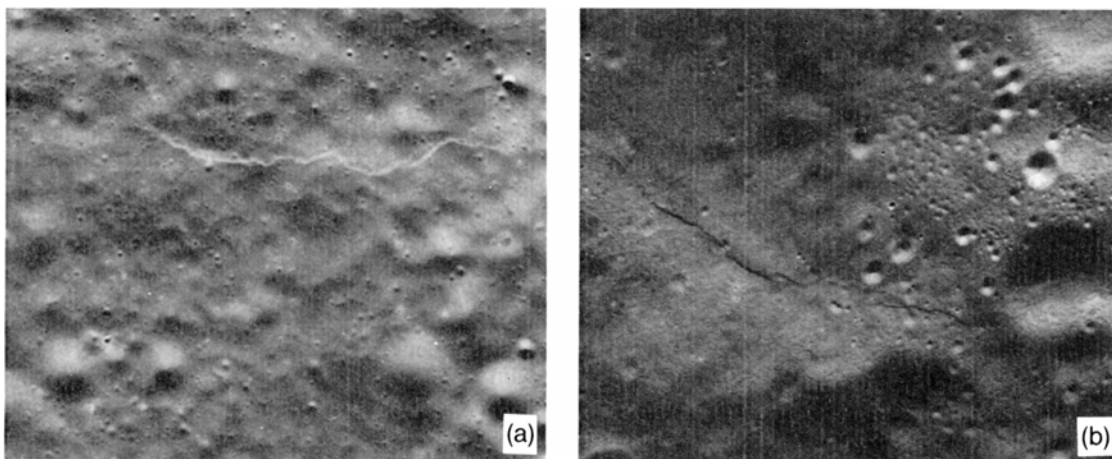


Fig. 4.33. Small scarps produced by compressive thrust faults in the lunar highlands. Such features are interpreted by *Binder and Gunga* (1985) to have formed recently by compression produced as a result of cooling and shrinking of the lunar interior. **(a)** Mandel'shtam Scarp (upper right), approximately 13 km long and located at 7°N/161°E near Mandel'shtam Crater (NASA Photo AS16-P-4150). **(b)** Morozov Scarp, approximately 15 km long, is located at 7°N/130°E, inside Morozov Crater (NASA Photo AS16-P-4970).

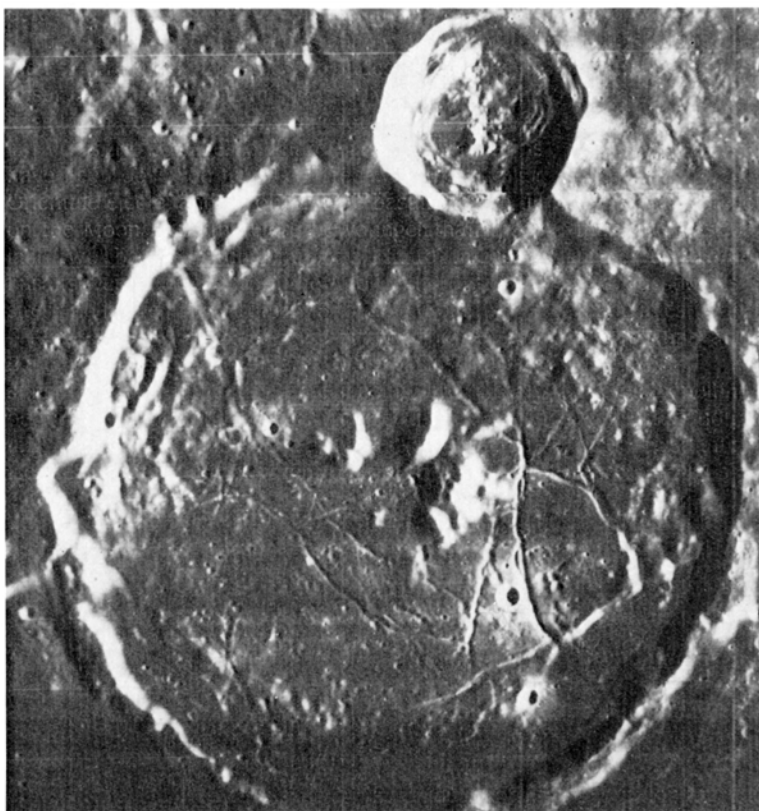


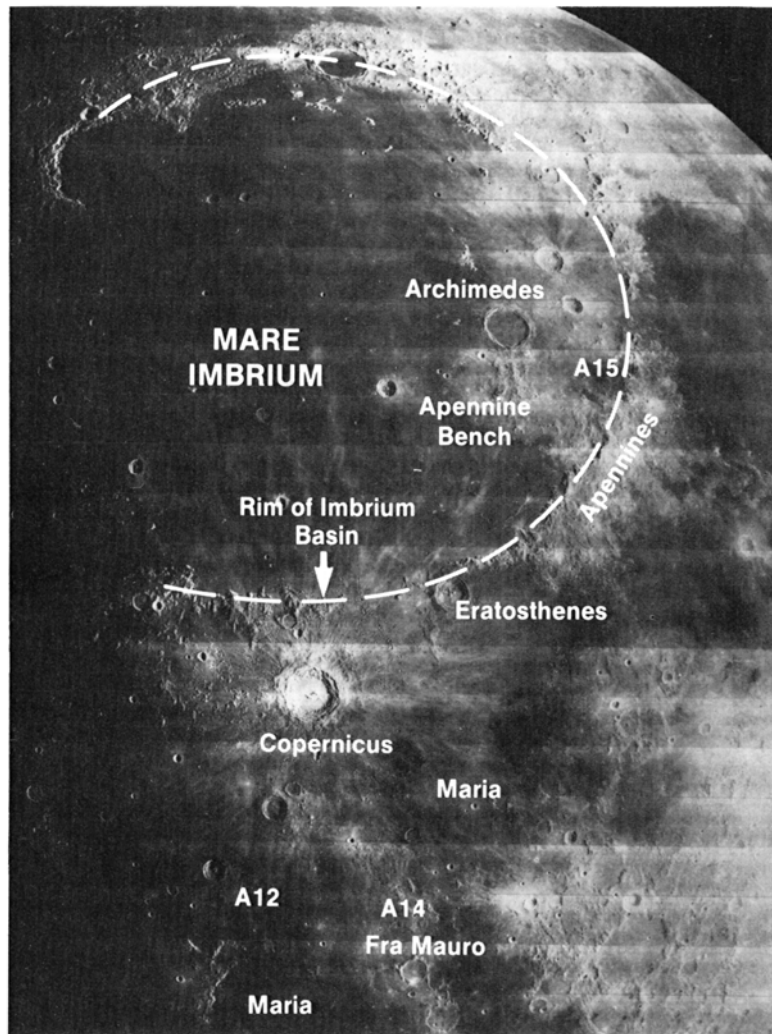
Fig. 4.34. Floor-fractured Gas-sendi Crater (110 km in diameter). Note the relatively flat crater floor apparently represents a filling of volcanic lava or impact melt. After solidification, this filling of the crater fractured irregularly, either because of contraction, subsidence of the crater floor, or intrusion beneath the crater floor (NASA Photo LO IV-143 H₂).

The techniques of lunar geologic mapping and stratigraphy are well illustrated by the region around Copernicus Crater, studied by *Shoemaker and Hackman* (1962) (Fig. 4.35). Copernicus is the youngest major impact crater in this region, as indicated by the fact that its rays and secondary craters overlie all the other geological units. The nearby Eratosthenes Crater (Fig. 4.35) has been overlain by the rays from Copernicus, so it must have been there when Copernicus formed. Eratosthenes has also been excavated in dark, smooth mare material. From these observations, the relative ages of three events can be established; from young to old, they are (1) Copernicus impact, (2) Eratosthenes impact, and (3) the eruption of mare lavas.

These observations can be carried further back in time. In their turn, the dark maria lavas embay, fill, or overlie other units: (1) Archimedes Crater, (2) a light-colored unit (the Apennine Bench Formation), and (3) the rugged highlands area and mountains associated with the rim of the Imbrium Basin (Fig. 4.35). Moreover, the plains formed by the light Apennine Bench Formation also embay the Imbrium Basin rim. Therefore the entire sequence recognized in this area, from young to old, is as follows: (1) Copernicus, (2) Eratosthenes, (3) the maria, (4) Archimedes, (5) the Apennine Bench plains, and (6) the Imbrium Basin.

Similar observations have been successfully employed to make geologic-stratigraphic maps of

Fig. 4.35. Region of the Moon around the crater Copernicus (97-km diameter, left-center of photograph), where the lunar stratigraphic system was first defined (Shoemaker and Hackman, 1962). The formation sequence of features in this region is as follows (from youngest to oldest): Copernicus, Eratosthenes, dark maria filling, Archimedes, Apennine Bench light plains deposits, Imbrium Basin massifs, and surrounding highlands features. These relative age relations define the equivalent time-stratigraphic systems: Copernican, Eratosthenian, Procellarian (epoch of mare lavas), Imbrian, and pre-Imbrian (see Table 4.4 for the current system nomenclature). North at top; portion of NASA Photo LO IV-126M. A12, A14, and A15 mark the Apollo 12, 14, and 15 landing sites, respectively.



the entire Moon (Wilhelms, 1970, 1972, 1984, 1985, 1987). This stratigraphic information has been supplemented by relative ages based on crater densities (see section 4.1.3) and by other age estimates based on the degradation of original crater shapes with time, caused by subsequent continuous bombardment. (See Fig. 4.36 for details on the relationship between a crater's size, its relative age, and the degree of degradation of its original features.)

The original lunar stratigraphic system established by Shoemaker and Hackman (1962) is shown in Table 4.4. Prior to the Apollo landings, the age durations of the various subdivisions of this system were unknown. Most of them were believed to be ancient; indeed, the ages of the maria were estimated to be 4.5 to 3.5 b.y. old (Shoemaker *et al.*, 1962; Hartmann, 1966). The measurement of abso-

lute ages of returned mare basalt samples allowed us to establish absolute dates for these photogeologically recognized systems.

The Moon has been mapped geologically at a variety of scales. A program to systematically map the lunar nearside at 1:1,000,000 scale was begun in 1962 and completed in 1972 (see Wilhelms, 1970). In addition, all the prime and potential Apollo landing sites were mapped at scales ranging from 1:1000 to 1:100,000, including several sites of strong geologic interest that were never visited by Apollo missions. After the Apollo flights, a global synoptic mapping program was undertaken at 1:5,000,000 scale. The resulting maps cover the lunar equatorial region in four sheets (Wilhelms and McCauley, 1971; Wilhelms and El Baz, 1977; Stuart-Alexander, 1978; Scott *et al.*, 1977); the lunar poles are covered in two more sheets (Lucchitta, 1978; Wilhelms *et al.*, 1979).

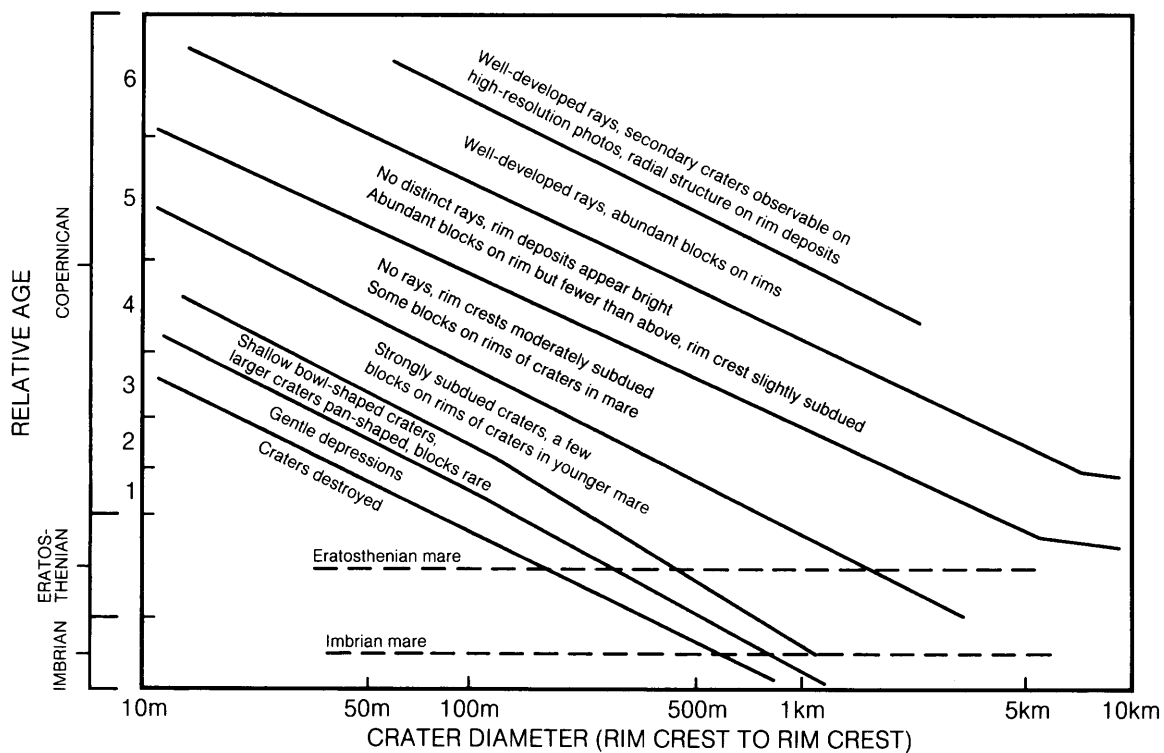


Fig. 4.36. Criteria used to characterize the relative degradational state of lunar impact craters >10 m in diameter. Post-crater degradation (loss of rays, lowering of rims, infilling) is produced by the continuing post-impact bombardment of the crater by smaller meteoroids. For a given original diameter, more degraded craters are older than less degraded ones, and the relative degree of degradation can be used as shown in the figure to establish the relative sequence of crater formation ages. For example, on the older Imbrian mare surface, all craters <500 m across have been completely destroyed, while on the younger Eratosthenian mare surface, craters as small as 200 m are still preserved. Even smaller craters (>50 m across) are preserved on the youngest Copernican mare surface. (Based on Trask, 1977 and after Wilhelms, 1985; see also Soderblom, 1970; Boyce, 1976; Schultz *et al.*, 1976; Basilevski, 1976.)

TABLE 4.4. Lunar stratigraphic systems—original and current (youngest to oldest).

System	Typical Units	Approximate Age (b.y.)
Original (<i>Shoemaker and Hackman, 1962; Shoemaker et al., 1962</i>)		
Copernican	Rayed craters	—
Eratosthenian	Nonrayed craters	—
Procellarian	Maria	4.5
Imbrian	Ringed basins	—
Pre-Imbrian	Terrae	4.6
Current (<i>Wilhelms, 1985</i>)		
Copernican	Fresh, rayed craters; minor maria	1.2-present
Eratosthenian	Slightly degraded craters, significant maria	3.2-1.2
Imbrian	Imbrium and Orientale basins; Cayley plains; degraded craters; most maria	3.85-3.2
Nectarian	Nectaris + 12 other basins; many degraded craters; some light plains	3.92-3.85
Pre-Nectarian	Basins and craters; volcanic and intrusive igneous rocks; megaregolith and crust	Before 3.92

These global maps are our current best summary of the geology of the Moon; a condensed version prepared from them is shown in Plate 10.10 (see also *Wilhelms, 1986*).

The lunar stratigraphy represented in these maps is subdivided into four major periods that are described from youngest to oldest in the following discussion. This arrangement, from young to old, is not normally practiced in stratigraphic descriptions on Earth. However, it is commonly used for the Moon because it aids the attempt to trace well-understood and comparatively recent processes into the distant and much more uncertain past.

Copernican Period (the present to ~1 b.y. ago). Copernicus Crater (96 km diameter) is one of the most recent large lunar craters. Its conspicuous rays cover much of the lunar nearside, and these rays can be used to determine unambiguously which surface units are older or younger than Copernicus itself. Very few large lunar craters (>50 km diameter) are younger than Copernicus; possible examples include Tycho and Kepler. Copernicus is currently believed to be approximately 900 m.y. old (*BVSP, 1981*), and the Copernican Period probably encompasses the last 1 b.y. of lunar history.

Virtually no internally-derived surface units (e.g., lava flows) younger than Copernicus have been identified. The Copernican Period is dominated by continuous and relatively modest impact cratering, which has produced small craters and created much

of the powdery lunar surface layer (regolith). Some minor tectonic activity, indicated by young thrust faults, has apparently also occurred (see section 4.3).

Eratosthenian Period (~1.0~3.2 b.y.). Eratosthenes Crater is similar to Copernicus in size. Although still well preserved, Eratosthenes is demonstrably older than Copernicus because its ray system has been essentially destroyed and its ejecta deposits underlie Copernican rays. Eratosthenes represents a class of abundant, moderately degraded craters >20 km in diameter, all of which are apparently older than Copernicus. Some of these craters and their surrounding ejecta deposits have been flooded by the youngest mare basalts. Although Eratosthenes itself has not been affected by basalt flows, the basalts in which Eratosthenes was formed are, on the basis of crater density measurements, estimated to be older than the youngest mare basalt units.

These observations indicate that the beginning of the Eratosthenian Period and the formation of the Eratosthenian class of craters was coincident with the ending of the great eruptions that more or less filled the mare basins with basaltic lavas. Most, but not all, of the Eratosthenian craters are flooded by the youngest mare basalts, and the end of major volcanic activity is more or less coincident with many Eratosthenian craters. The Eratosthenian Period therefore includes the last stages of major lunar basaltic volcanism, as well as some modest

subsequent basin subsidence and associated graben and ridge formation. Most of the surface debris (*regolith*) covering the lunar maria was also formed during this period. Eratosthenian basalts were collected at the Apollo 12 site, and their measured age dates suggest that initiation of this period can be placed at approximately 3.2 b.y. ago.

Imbrian Period (3.2–3.8 b.y.). The formation of the Imbrium Basin by a huge impact was a major event on the lunar nearside. Ejecta from this basin dominate a substantial fraction of the lunar globe and caused virtually complete reconstruction of the lunar surface in a large annulus around the basin. Imbrium ejecta represent the most important stratigraphic marker unit on the lunar nearside. Crater densities on these deposits indicate that substantial large-scale cratering activity continued for some time after formation of the Imbrium Basin. This activity includes the formation of at least one more basin (Orientale). Although some samples of Imbrium ejecta may have been returned by the Apollo 14, 15, and 16 missions, positive identification is currently not possible because of the intensity and complexity of cratering events at that time. The formation age of the Imbrium Basin is not known precisely, but is estimated to be between 3.8 and 3.9 b.y. ago.

It has become convenient to divide the Imbrian period into two parts, characterized by different kinds of geological activity. The “Early Imbrian” Epoch, which is bracketed by the Imbrium and Orientale basin-forming impacts, was a period of substantial cratering activity. Apollo 14 and 16 landed on heavily-cratered “Early Imbrian” surfaces (Head, 1974b; Hawke and Head, 1977). Many impact melts characterizing this period are 3.8 to 3.9 b.y. old, but the exact time boundaries (i.e., the ages of the Imbrium and Orientale Basins) have not been determined.

The “Late Imbrian” Epoch is characterized by less intense cratering and also includes most of the observable lunar volcanism, i.e., virtually all the basaltic mare fill, except for the younger Eratosthenian flows. No surfaces of mare basalt within basins have been observed to be covered with Imbrium or Orientale ejecta, and all observable basaltic basin fill on the Moon must therefore be younger than these last two basin-forming impacts. “Late Imbrian” basalts were returned from the Apollo 11, 15, and 17 sites and range in age from 3.75 to 3.2 b.y. old.

Nectarian Period (3.8–~3.9 b.y.). The Nectaris Basin is typical of several large mare basins that are substantially degraded. Some basins are clearly better preserved and therefore younger than Nectaris (e.g., Serenitatis), while some are older (e.g., Smythii). Isolated patches of apparent Nectaris ejecta are

clearly preserved in the Janssen Formation, and parts of the Nectaris rings occur in such places as the Altai Mountains.

By definition, the Nectarian Period encompasses lunar history between the Nectaris and Imbrium Basin impacts. Formation of the Nectaris Basin is estimated to have occurred between 3.8 b.y. ago (Wetherill, 1981) and ~3.9 b.y. ago (James, 1981; Spudis, 1984). These estimates are based on a number of Apollo 16 samples thought to be Nectaris ejecta. The Nectarian Period was therefore relatively short, approximately 200 m.y., compared to the other stratigraphic periods.

During the Nectarian Period, about a dozen lunar basins formed, and numerous other large-scale impacts occurred, indicating an epoch of heavy bombardment that is not reflected in later lunar history. Wilhelms (1976, 1984) estimates formation of a minimum of 1700 craters ≥ 20 km in diameter on the whole Moon. Heavy reworking of the lunar crust certainly took place at this time, including substantial vertical and lateral mixing. Early basaltic volcanism may also have occurred during the Nectarian Period (Schultz and Spudis, 1979; Taylor et al., 1983; Wilhelms, 1984, 1985).

Samples possibly representing Nectarian age deposits were returned from the Apollo 17 site (located at the rim of Mare Serenitatis), probably from the Apollo 16 site (Nectaris ejecta itself?), and possibly even from Apollo 15 (Serenitatis ejecta?).

Pre-Nectarian Period (~3.9–~4.6 b.y.). As implied by the name, this period encompasses all geologic history prior to the Nectaris impact. Features from this period are still clearly observable, but their complexity and the violence of events during this period has made it impossible at present to do the detailed morphological and chronological classification that would allow systematic geological subdivision and mapping.

This period is clearly characterized by heavy cratering and by the formation of many large impact basins. Wilhelms (1984) identifies 30 basins older than Nectaris, some of which are much larger (albeit largely eroded) than the younger, more recognizable major basins and rings. As discussed in section 4.1, one of the unresolved lunar questions is exactly how many of these large, ancient impact structures are preserved and how many have been destroyed. Until this question is settled, little improvement can be made in estimates of the number of large craters and basins that actually formed during pre-Nectarian time.

Global melting, chemical differentiation, crystallization, flotation, and solidification of a feldspar-rich lunar crust must have occurred very early in lunar history (>4.4 b.y. ago; section 2.4.3), but no direct

TABLE 4.5. Relative ages of known and possible (parentheses) ringed impact basins on the Moon, proceeding from youngest (class 1) to oldest (class 15) on the basis of photogeologic observations related to degradational state and crater density (from *Wilhelms*, 1984).

Basin*	Center		Diameters (km) [†]		Age [‡]
	Lat	Long	Main rim	Other ring(s)	
Orientele	20 S	95 W	930	620-480-320	1-I
Schrödinger	75 S	134 E	320	150	2-I
Imbrium	33 N	18 W	1200	670	3-I
Sikorsky- Rittenhouse	69 S	111 E	310	—	4-N
Bailly	67 S	68 W	300	150	
Hertzprung	2 N	129 W	570	410-265	
Serenitatis	27 N	19 E	740	420	
Crisium	18 N	59E	1060	635-500-380	
Humorum	24 S	40 W	820?	440-325	
Humboldtianum	61 N	84 E	600	275	
Mendeleev	6 N	141 E	330	140	5-N
Mendel-Rydberg	50 S	94 W	630?	460-200	6-N
Korolev	5 S	157 W	440	220	
Moscoviense	26 N	147 E	445	210	
Nectaris	16 S	34 E	860	600-450-350	
Apollo	36 S	151 W	505	250	7-pN
Grimaldi	5 S	68 W	430	230	
Freundlich- Sharonov	19 N	175 E	600	?	8-pN
Birkhoff	59 N	147 W	330	150	9-pN
Planck	58 S	136 E	325	175	
Schiller-Zucchi	56 S	45 W	325	165	
(Amundsen- Ganswindt)	81 S	120 E	355		
Lorentz	34 N	97 W	360	185	10-pN
Smythii	2 S	87 E	840	(600)-360	11-pN
Couloumb-Sarton	52 N	123 W	530?	400-180	
Keeler-Heaviside	10 S	162 E	780?	540	
Poincaré	58 S	162 E	340	175	12-pN
Ingenii	34 S	163 E	560?	325	
Lomonosov-Fleming	19 N	105 E	620		13-pN
Nubium	21 S	15 W	690		
Fecunditatis	4 S	52 E	690		
Mutus-Vlacq	52 S	21 E	700		
Tranquillitatis	7 N	40 E	775?		
Australe	52 S	95 E	880	(550)	

TABLE 4.5. (continued).

Basin*	Center		Diameters (km) [†]		Age [‡]
	Lat	Long	Main rim	Other ring(s)	
(Al Khwarizmi-King)	1 N	112 E	590		14-pN
(Pingré-Hausen)	56 S	82 W	300?		
(Werner-Airy)	24 S	12 E	500?		
(Balmer-Kapteyn)	16 S	69 E	550?		
(Flamsteed-Billy)	8 S	45 W	570?		
(Marginis)	20 N	84 E	580		
(Insularum)	9 N	18 W	600?		
(Grissom-White)	40 S	155 W	600?		
(Tsiolkovskiy-Stark)	15 S	128 E	700?		
South Pole-Aitken	56 S	180	2500		15-pN
(Procellarum)	26 N	15 W	3200	2400-1700	

* Basin names from two superposed, unrelated craters (*Wilhelms and El-Baz*, 1977) or from contained mare.

[†] Main rim refers to topographic basin rim.

[‡] "Age" ranked from youngest (top) to oldest (bottom). I = Imbrian; N = Nectarian; pN = pre-Nectarian. Fifteen age groups are given; Basins cannot be accurately ranked within a group. Those basins in a group are ranked in order of increasing size.

morphological evidence is available for these processes. Evidence for the Moon's earliest history and processes must be extracted from the returned rocks by petrogenetic and cosmochemical reasoning that encompasses the accretion and origin of the Moon itself.

Despite the violence and intensity of early lunar history, it is clear that relatively little geological activity has taken place on the Moon during the last 3 b.y. It is also clear that the absolute chronology of the early basin-forming events is not well understood, despite the great importance of these events in the lunar stratigraphic record. Fortunately, photogeologic analysis can successfully establish the relative sequence of most basin-forming events and Table 4.5 lists the relative ages of 42 Nectarian and pre-Nectarian ringed impact basins based on remote mapping.

Some of these basins have probably provided materials that are now among the Apollo returned samples. Ejecta from Orientale, Imbrium, Serenitatis, and Nectaris basins are most likely present in the Apollo sample collection, but it has not yet been possible to unambiguously associate a given sample with a specific basin. Neither is it clear at present how the observed cratering record and the range of measured crystallization ages of impact melts from the lunar highlands relate to each other (see section 6.4).

Despite the small number of places visited by the Apollo and Luna sample-return missions (Fig. 2.1), it is clear that numerous returned soil and breccia samples are related to the younger Copernican Period and Eratosthenian Period and reflect their dominant processes. The Apollo 12 mission provided samples of the young Eratosthenian basalts, and the older Late Imbrian basalts were obtained from several mare landing sites. Other samples have provided evidence for basaltic volcanism as long ago as 4.2 b.y. (*Taylor et al.*, 1983), and these results constitute the strongest argument for very early lunar volcanic activity. The record of intense cratering and basin formation for periods older than 3.8 b.y. is poorly understood, but it must be present in many highland samples obtained from the Apollo 14, 15, 16, and 17 landing sites.

There is general consensus that the lunar geological history as summarized in Fig. 4.37 is well established for the last 3.8 b.y. This historical reconstruction is a remarkable feat considering how few locations were actually sampled. In a sense, the Moon itself collaborated in this work, because it has experienced only a limited variety of geological processes for most of its existence and because it has preserved its records well. The heavily cratered, more active Moon that existed before >3.8 b.y. ago is more difficult to understand. Impact cratering clearly dominated these early surface processes, but

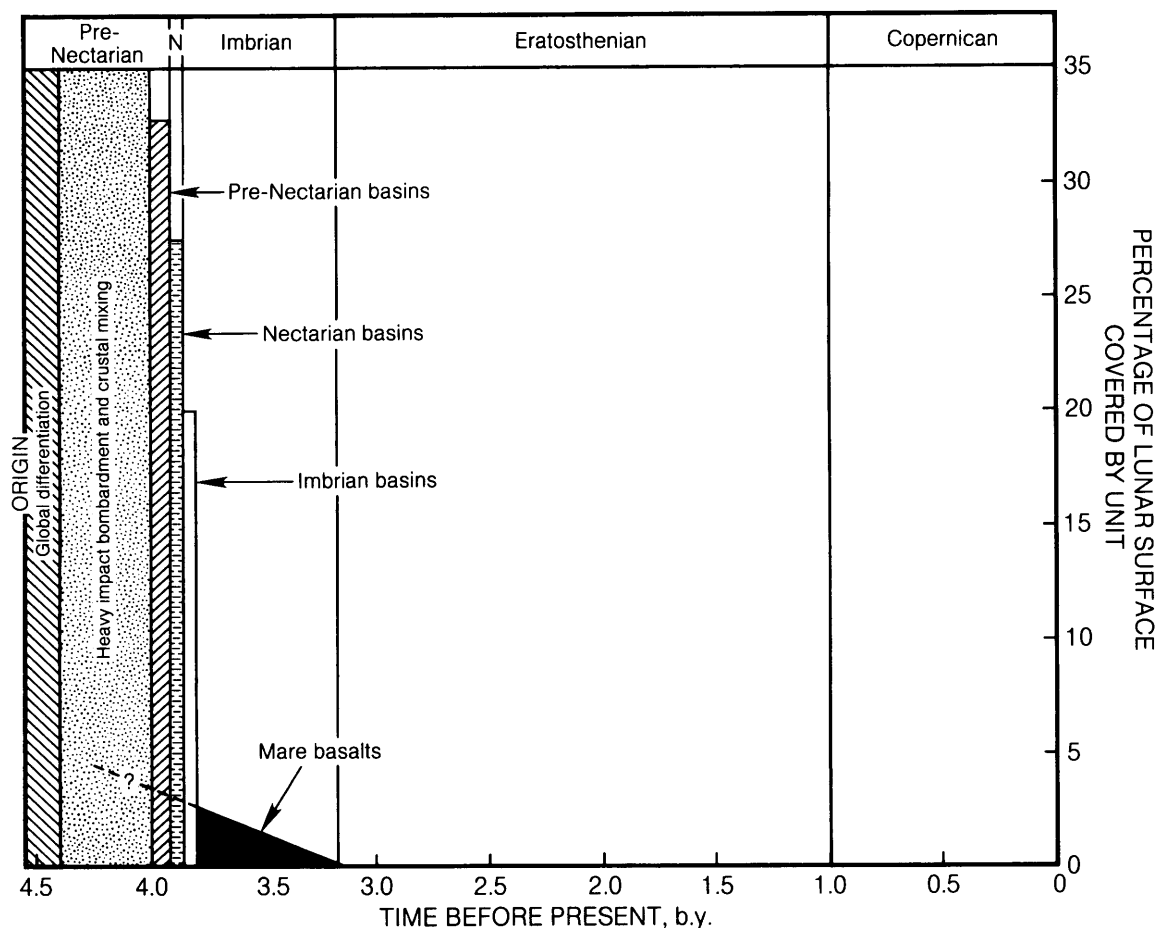


Fig. 4.37. Ages of lunar geological units, plotted against the percentage of the lunar surface covered by each unit or group of units (from *Wilhelms, 1984*). “Basin materials” include basin interior deposits and continuous basin ejecta to a distance of one basin radius beyond the basin margin. Eratosthenian and Copernican Crater deposits cover barely enough area to appear on this diagram. Ages are approximate and may overlap. The extrapolation of eruption rates for mare basalt lava units into the older period of intense cratering is uncertain and highly model dependent; there may have been a steady decline in heavy cratering throughout the early history of the Moon, and it may have continued into the Late Imbrian Period, while the rate of lava eruptions was also declining. Volcanism is shown as having ended at the beginning of the Eratosthenian Period; there may be Eratosthenian- and Copernican-age lavas, but any such deposits are too small to be visible on this diagram.

the details of the bombardment history and the absolute ages of even the youngest multiring basins are still not well known. Upon return to the Moon, this early bombardment history must be attacked with vigor. Extensive field exploration and sampling of materials from known structural/stratigraphic settings will constitute a crucial part of this effort. For example, collection and dating of the Orientale impact melt to determine the formation time of the Orientale Basin itself will provide an important insight into the end of large basin formation, for all other large basins are older. Other impact melts

recording the formation of most “young” multiring basins (e.g., Imbrium) may be collected and dated as well to yield additional insight into the early cratering history of the Moon. Impact melts from Tycho, Copernicus, and Eratosthenes would greatly illuminate the crater production rate over the past 3 b.y. Improved understanding of the lunar crater production rate would be useful not only for lunar stratigraphy; the data would also help us understand the intense collisional environment that must have affected all the planets in the early inner solar system, including Earth.